Carbon Nanotubes Under Pressure

Yiwei Sun

PhD thesis

School of Physics and Astronomy
Queen Mary University of London

June 2015

Abstract

Graphene has been investigated intensively since its discovery in 2004, for its unique mechanical and electrical properties. Strain modifies these properties to meet specific scientific or technological needs. Therefore, the strain determination and monitoring are of critical application importance and contribute to the characterization and understanding of this remarkable material. However, in many cases strain cannot be directly and precisely measured. Strain is therefore related to easily-detected phonon frequency. To be specific, researchers attribute the frequency shift of graphene in-plane vibrational mode E_{2g} (the graphite-mode) entirely to the in-plane strain and quantify this relation via the Grüneisen parameter and shear deformation potential. Different values of these parameters however have been reported by various experiments and calculations. The discrepancy comes from considering the in-plane strain contribution alone and whether this error is acceptable depends on the accuracy required in the specific scientific or technological problem. Chapter 2 presents our work to quantify other contributions to the graphite-mode shift under strain, namely the compression of the π-electrons into the sp^2 network. Calculations will use density functional theory, generalised gradient approximation for the exchange-correlation potential, with the van der Waals interaction add-on.

Carbon nanotubes can be considered as rolled-up graphene sheet. Similar to graphene, strain modifies their properties and can be determined and monitored by the graphite-mode frequency. The tube structure gives additional mechanical stability for application and meanwhile, complication in the relationship between frequency and applied strain. The *thick wall tube* model explains the effect of tube diameter on this relation (Chapter 3) while more recent experiment shows the graphite-mode frequencies of tubes of similar diameter but different chiralities shift very differently under pressure (Chapter 4), which is beyond current understanding. The significant bundling effect is reported but not fully understood either (Chapter 5). Chapter 6 presents our attempt to describe the collapse of tubes with the *atomistic refined elastic ring* model.

Statement of originality

I, Yiwei Sun, confirm that the research included within this thesis is my own work or that where it has been carried out in collaboration with, or supported by others, that this is duly acknowledged below and my contribution indicated. Previously published material is also acknowledged below.

I attest that I have exercised reasonable care to ensure that the work is original, and does not to the best of my knowledge break any UK law, infringe any third partys copyright or other Intellectual Property Right, or contain any confidential material.

I accept that the College has the right to use plagiarism detection software to check the electronic version of the thesis.

I confirm that this thesis has not been previously submitted for the award of a degree by this or any other university.

The copyright of this thesis rests with the author and no quotation from it or information derived from it may be published without the prior written consent of the author.

Signature: Sun Yiwei Date: 03/07/2015

Details of collaboration: I am very grateful that the experiments in Chapter 3 were performed by Dr. Ahmad Ghandour within my research group and the Molecular Dynamics simulation in Chapter 6 was performed by Dr. Markus Hartmann from University of Leoben.

Acknowledgements

First of all, I would like to thank Professor David Dunstan, who as my primary supervisor, makes my four-year PhD study absolutely enjoyable. He has shared me with his skills, knowledge, way of thinking, provided me with lots of chances to do and present our work — visit collaborators, write papers and make oral presentations, and been a model scientist of great qualities to me. I would appreciate it that through him I have known many interesting English cultures.

I am very grateful for the help from Dr Ignacio Hernández, who very kindly and generously invited and hosted me in Santander for experiments. He took great care of me as the third kid in his family (the fourth in the next visit) during my stay and guided me as a very responsible supervisor in the lab. Together with Prof Jesus González and Prof Fernando Rodríguez, they contribute so much to our work and my PhD study that without them I would not be able to finish my PhD with such a confidence. I would also like to thank Ignacio's family — Patricia for her kind hosting, Rocio and Carmen for their accompanying.

I would like to thank Dr David Holec, who is an excellent theorist, showed and explained me the ideas and the process of calculations with great patience and rich experiences, yet being one of the most humble men I have met. Chapter 2 would not be there if it was not his hard work.

I acknowledge many academics in CCMMP — Dr Andrei Sapelkin, my second supervisor, for many helpful suggestions in experiments and data analysis, Dr Ken Scott and Dr Kevin Donovan for sharing their samples and knowledge of the functionalized tubes, Dr Alan Drew for very detailed guidance on the presentation of a scientific work, Prof Martin Dove, Dr Alston Misquitta and Dr Anthony Philips for advice on calculations and Dr Mark Baxendale and Dr John Dennis for sharing their knowledge of carbon nanotubes. I would also like to thank many people from professional services in School of Physics — Dr George Nevill for everything related to chemicals, Mr Predrag Micakovic and Dr Terry Arter for everything related to computer (I have bothered them so many times), Ms Kathy Boydon and Ms Sarah Cowls for being very kind and supportive and Mr John Sullivan for accepting my request every single time.

I acknowledge School of Physics and Astronomy in Queen Mary, University of London and Chinese Scholarship Council. They offered me this great opportunity to study and work.

Finally, I am grateful for the supports from my family — my wife, Mia Zhou, who live with me here in London and my parents, Limin Wang and Xiaoming Sun, who have been always sharing my joys and worries for these four years.

Contents

List of Figures

List of Tables

List of abbreviations

CNTs	carbon nanotubes
GM	graphite-mode
SWCNTs	single-wall carbon nanotubes
SDP	shear deformation potential
DAC	diamond anvil cell
PTM	pressure transmit media
RRS	resonance-enhanced Raman spectroscopy
DWCNTs	double-wall carbon nanotubes
RBM	radial breathing mode
DFT	density functional theory
GGA	generalized gradient approximation
VASP	Vienna Ab initio Simulation Package
vdW	van der Waals
LDA	local-density approximation
MD	molecular dynamics
MDAC	membrane diamond anvil cell
FWHM	full width at half maximum
ODA	octadecylamine
DCE	1, 2-dichloroethane
DOS	density of states

Chapter 1

Introduction

Carbon nanotubes (CNTs) have extraordinary mechanical properties due to the stiff sp^2 bond resulting in the exceptionally high Young's moduli at a typical value of 1 TPa, together with their tube structure [Treacy et al., 1996]. They have unique electronic properties; they can be either metallic or semiconducting depending on the chirality — the direction along which a tube is rolled up [Odom et al., 1998]. Pressure modifies these properties. The sp^2 bond stiffens further, and the band gap in semiconducting CNTs changes with pressure [Yang and Han, 2000]. To characterize and understand the behaviour of CNTs under pressure, the shift rates of the phonon frequencies with pressure are very interesting, as they directly reflect the mechanics and are closely related to the electronic properties. They can also be used as strain sensors.

In this thesis, I will focus on the shift with pressure of the graphite mode (GM). The GM is an in-plane vibrational mode, coming from graphite and characteristic of sp^2-hybridized carbon [Tuinstra and Koenig, 1970]. Studies of the GM pressure coefficients of CNTs thus provides a direct approach to understand the sp^2 bond. It links closely to the high pressure study of other sp^2-bonded materials such as graphene and graphite. That is why we will start with the study of graphene and graphite and then introduce the complexity brought by the wall curvature of CNTs.

1.1 The Graphite-mode Phonons in Graphite

The GM is the Raman-active $E_{2g}^{(2)}$ optical mode of graphite at 1582 cm^{-1}, illustrated in Figure 1.1 by Reich and Thomsen [2004]. It is a two-fold (longitudinal and transverse) degenerate mode, first reported by Tuinstra and Koenig [1970]. The degeneracy is removed if the symmetry is broken by an external perturbation, such as strain. Mohiuddin et al. [2009] demonstrated this in the case of

graphene under uniaxial tensile strain, where the G^+ (+ for higher energy) and G^- denote the two perpendicular modes (see Figure 1.2).

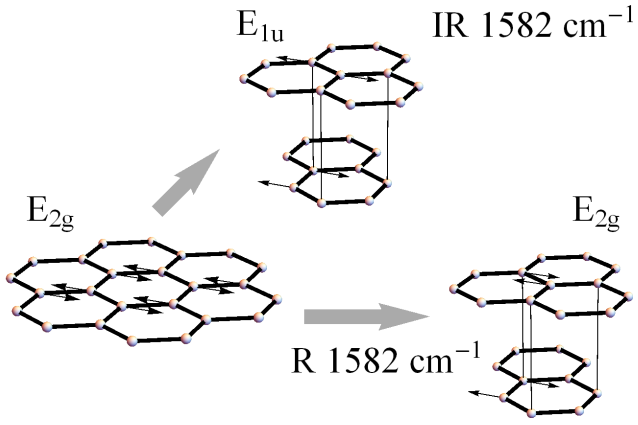

Figure 1.1: "Phonon eigenvectors of graphene and graphite. Every phonon eigenvector of graphene gives rise to two vibrations of graphite. For example, the in-phase combination of the two layers for the E_{2g} optical mode of graphene yields $E_{2g} \otimes A_{1g} = E_{2g}$ and the out-of-phase combination $E_{2g} \otimes B_{1u} = E_{1u}$. Next to the graphite modes it is indicated whether they are Raman (R) or infrared (IR) active and the experimentally observed phonon frequencies. The translations of graphite are omitted from the figure." After Figure 2 of Reich and Thomsen [2004].

Hanfland et al. [1989] recorded the first Raman spectrum of graphite under high pressure. Figure 1.3 shows the GM frequencies with the pressure under which they are obtained. The pressure dependence of the frequency

$$\omega(P)/\omega_0 = [(\delta_0/\delta')P + 1]^{\delta'} \tag{1.1}$$

where δ_0 is the logarithmic pressure derivative $(dln\omega/dP)_{P=0}$ and δ' is the pressure derivative of $dln\omega/dP$, least-square fitted to the experimental data. The frequency of the GM increased sublinearly under pressure with an initial pressure coefficient of 4.7 $cm^{-1}GPa^{-1}$.

The GM is an in-line anti-phase motion (see Figure 1.1) and therefore the shift of its frequency with pressure (4.7 $cm^{-1}GPa^{-1}$) should be determined by the shortening of $C-C$ bond. The sublinearity observed in graphite was considered [Sun et al., 2013] to be the result of the combination of the very soft C_{33}, 39 GPa in graphite [Bosak and Krisch, 2007] together with its relatively large pressure coefficient C'_{33} ~10 [Green et al., 1972] (see Section 2.1).

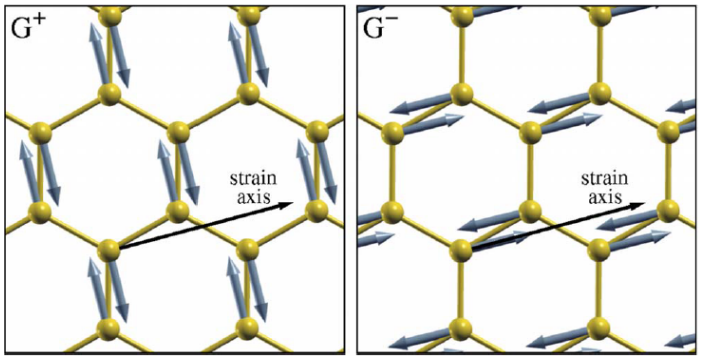

Figure 1.2: "Eigenvectors of G^+ and G^- modes determined by density-functional perturbation theory. These are perpendicular to each other, with G^- polarized along the tensile strain axis, as expected." Reprinted figure with permission from [T. M. G. Mohiuddin et al., Phys. Rev. B 79, 205433 (2009)] Copyright (2009) by the American Physical Society.

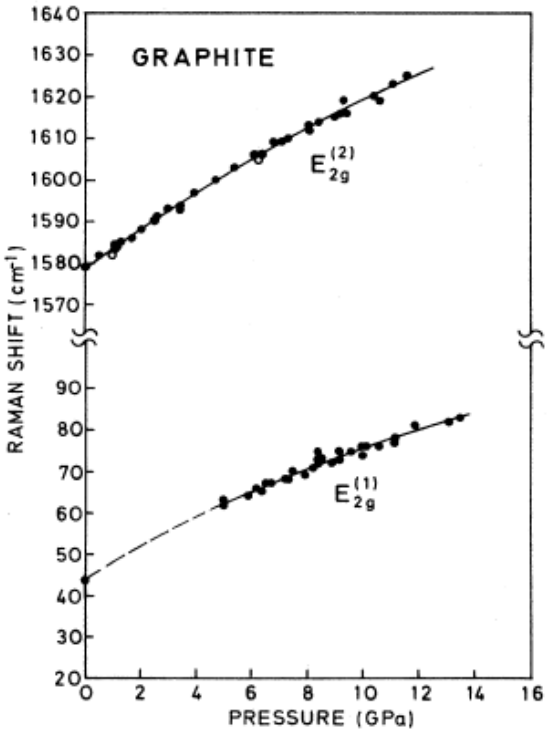

Figure 1.3: Raman shifts of the two E_{2g} modes of graphite. Lines are for the results of a least-squares fit of Eq. (1) to the experimental data. Open circles are for decreasing pressure. Reprinted figure with permission from [M. Hanfland, H. Beister, and K. Syassen, Phys. Rev. B 39, 12598 (1989)] Copyright (1989) by the American Physical Society.

1.2 What We Expect in Single-Wall Carbon Nanotubes

Graphene sheets are stacked to make graphite and rolled up to make single-wall carbon nanotubes (SWCNTs). It is reasonable to assume that the GM pressure coefficient of SWCNTs is also determined by the shortening of $C-C$ bond and therefore the shift rate of a solvent-filled tube is expected to be 4.7 $\mathrm{cm}^{-1}\mathrm{GPa}^{-1}$.

Now we consider an empty tube under hydrostatic pressure. Taking a finite wall thickness into account (the $thick-wall-tube$ model), the tangential stress is

$$\sigma_t = \frac{r_o}{r_o - r_i} P \tag{1.2}$$

and the axial stress is

$$\sigma_a = \frac{r_o^2}{r_o^2 - r_i^2} P \tag{1.3}$$

where r_o is the outer radius of the wall and r_i is the inner radius. Setting, for example, the diameter at a typical value of 1.3 nm and the wall thickness at 0.36 nm (the interlayer distance a_{33} of graphite), we expect the pressure coefficients of the 'tangential' mode to be 8.5 and the 'axial' to be 5.9 $\mathrm{cm}^{-1}\mathrm{GPa}^{-1}$ (see Chapter 3 for details). Jorio et al. [2002] assigned the lower energy G^- to the tangential mode, the frequency of which is sensitive to the tube wall curvature and the higher energy G^+ to the axial mode which is independent of the curvature. A caveat here is the significant electron-phonon coupling due to a Kohn anomaly, which softens only the axial mode of metallic tubes and hereby makes it G^-. This was predicted [Dubay et al., 2002] and confirmed [Farhat et al., 2007], while its effect on the GM pressure coefficients, however, is still unclear.

If we keep compressing an empty tube, there is a critical point, beyond which it will collapse. Therefore we expect the GM to shift with pressure as illustrated in Figure 1.4 — the shift rate is at the value of a thick-wall hollow tube initially and the frequency and its shift rate should both decrease to the values of graphite when the tube collapses [Caillier et al., 2008]. I will briefly discuss the problem of the collapse in Chapter 6.

1.3 What We Find (Not What We Expect)

First, I introduce early published results of the GM pressure coefficients which were not assigned to a specific tube diameter. Venkateswaran et al. [1999] performed the first high pressure experiment on SWCNTs. They loaded samples into a diamond anvil cell (DAC) and recorded their Raman spectra at various pressures (see Figure 1.5). They plotted the frequencies of the G^+ (T3) and

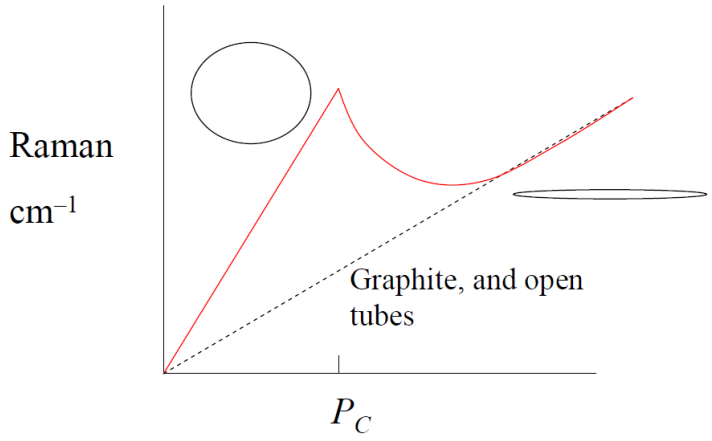

Figure 1.4: The solid line is for the GM shift with pressure of a hollow SWCNT and the dash line is for graphite. The GM frequency of CNTs first shifts at a higher rate than graphite and after the critical pressure P_C, both the shift rate and the frequency drop to the value of graphite, corresponding to a collapse phase. This illustration is based on the results reported by Caillier et al. [2008].

the wall-curvature (tube diameter) dependent G^- band (T1 and T2) with pressure (see Figure 1.6), and obtained initial linear shift rates at 7.1, 10 and 8 $cm^{-1}GPa^{-1}$ for T3, T2 and T1, respectively.

Since then, many high pressure studies on the GM of SWCNTs has been published, using various laser excitation wavelength and different pressure transmit media (PTM). Only recently were the GM pressure coefficients assigned to a specific diameter; we return to this point later. Meanwhile, no consensus on the value of the pressure coefficient was achieved, as shown in Figure 1.7 [Venkateswaran et al., 1999, Christofilos et al., 2007, 2005, Ghandour et al., 2011, Venkateswaran et al., 2001, Proctor et al., 2006, Thomsen et al., 1999, Lebedkin et al., 2006, Sood et al., 1999, Sandler et al., 2003, Merlen et al., 2005, Yao et al., 2008], which gives a summary of some early work on the shift rates of the dominant G^+ band (the signal is clear enough to extract accurate frequencies despite to the weaker signals from inside diamond-anvil high-pressure cells). Nevertheless, what can be seen from Figure 1.7 is that effects such as PTM, laser excitation energy and bundling/surfactant can all affect the GM pressure coefficients observed.

Although we cannot yet give a clear answer what the GM pressure coefficients are, some facts are worth noticing before considering the assignment of data to particular diameters. First, the evolution of the GM shift with pressure was reported to indicate tube collapsing as expected. Yao et al. [2008] and Caillier et al. [2008] presented a representative GM shift with pressure (see Figure 1.8),

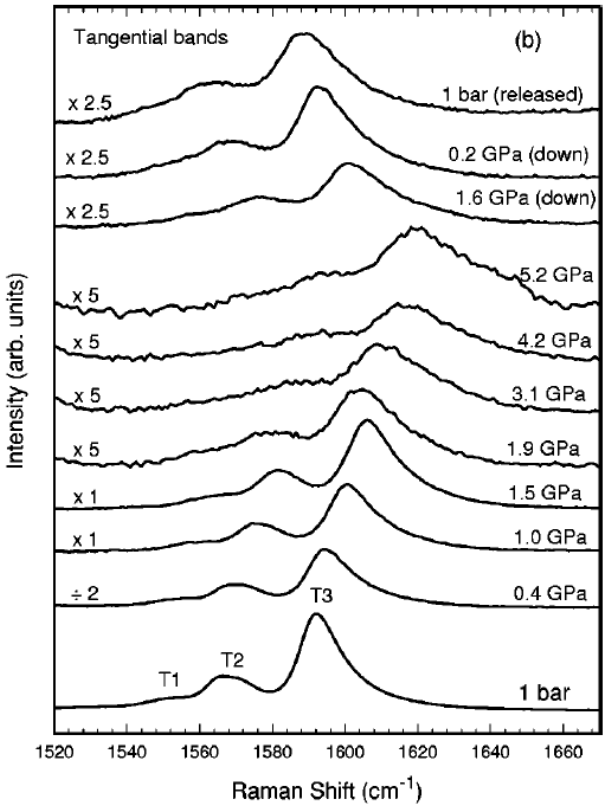

Figure 1.5: The pressure dependence of the room-temperature Raman spectra of SWCNTs bundles for the GM. The GM intensity drops significantly above 1.5 GPa. The spectra were recorded using 514.5 nm excitation. Reprinted figure with permission from [U. D. Venkateswaran et al., Phys. Rev. B 59, 10928 (1999)] Copyright (1999) by the American Physical Society.

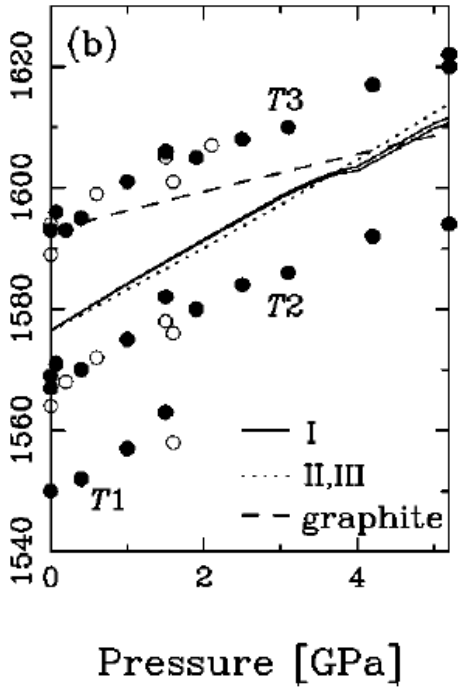

Figure 1.6: Pressure dependence of the GM frequencies of SWCNTs bundles. The results of the calculations using different models are indicated by solid and dotted lines. Experimental data (T1, T2, and T3) measured during the upward and downward cycles of pressure are plotted as solid and open circles, correspondingly. Dashed line corresponds to generalized tight-binding molecular dynamics result for the $E_{2g}^{(2)}$ mode frequency in graphite. Reprinted figure with permission from [U. D. Venkateswaran et al., Phys. Rev. B 59, 10928 (1999)] Copyright (1999) by the American Physical Society.

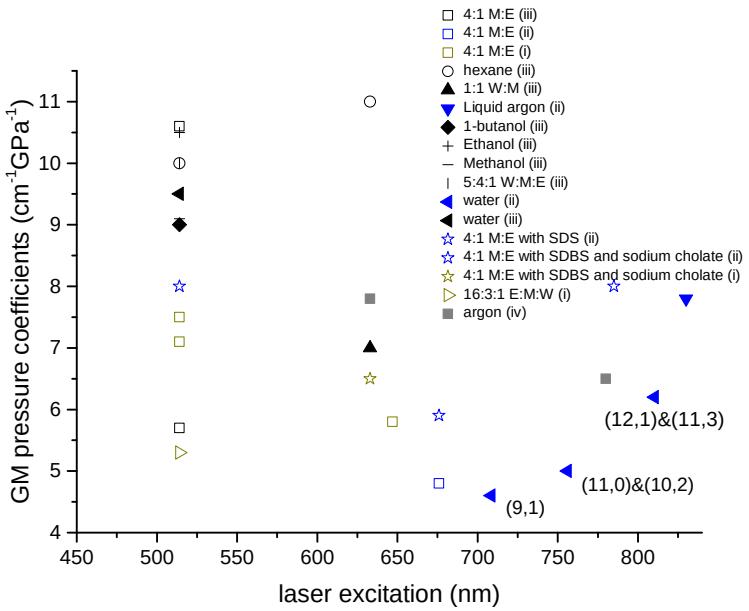

Figure 1.7: The GM pressure coefficients of SWCNTs reported in previous literature are plotted against the laser excitation wavelengths, at which they were obtained. Symbols identify the PTM used. The stars are for the individual tubes dispersed by surfactants. Three points are labelled with specific chiralities, to which they are assigned. M:Methanol; E:Ethanol; W:Water; SDS:Sodium dodecyl sulfate; SDBS:Sodium dodecylbenzene sulfonate. i: samples produced by pulsed-laser vaporization process, with a diameter range of 1.22–1.36 nm; ii: high pressure catalytic decomposition of carbon monoxide, 0.8–1.2 nm; iii: arc discharge method, 1.2–1.6 nm; iv: synthesis method not specified, 1.3±0.2 nm, labelled as dark green, blue, black and grey, respectively.

clearly showing that GM frequency of empty tubes shifts faster than graphite initially. The rate and the frequency dropped to the values of graphite after the tubes collapse. Second, the GM pressure coefficients of solvent-filled tubes, against expectation, are not 4.7 $cm^{-1}GPa^{-1}$. Merlen et al. [2006] reported the GM pressure coefficients of open-ended tubes as 6.5 $cm^{-1}GPa^{-1}$ in argon and in 4:1 methanol-ethanol, and as 10 $cm^{-1}GPa^{-1}$ in paraffin oil. This raises another issue: what molecules can enter, and how much they can enter, into a SWCNT through an open end. Third, doping shifts the GM frequencies. Skakalova et al. [2005] reported the doping effects on the GM frequency (see Figure 1.9), which indicates that the charge transfer shifts the GM frequency, but whether it changes the GM pressure coefficient is unclear — an increase in charge transfer with pressure is plausible, and this would impact on the pressure coefficient.

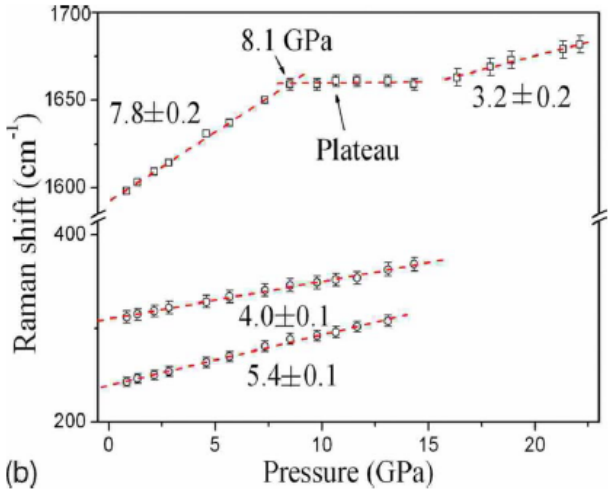

Figure 1.8: The frequencies of two RBMs (circles) and the most intense G^+ peak (squares) are plotted with pressure. Reprinted figure with permission from [Mingguang Yao et al., Phys. Rev. B 78, 205411 (2008)] Copyright (2008) by the American Physical Society.

Recent reported experimental work enables the assignment of the observed GM pressure coefficients to a specific tube diameter. This can be done in two ways: using resonance-enhanced Raman spectroscopy (RRS), which generally requires a Raman system with a wavelength-tunable laser (see Chapter 2), or using SWCNTs samples of a single diameter. Liu et al. [2011] fractionalised SWCNTs of a single chirality (and therefore diameter) and later Sanchez-Valencia et al. [2014] successfully synthesised them, but these tubes are not yet commercially available and no high pressure study of them has been reported. Hence, here our study focuses on the other method, picking out tubes of a specific diameter by RRS.

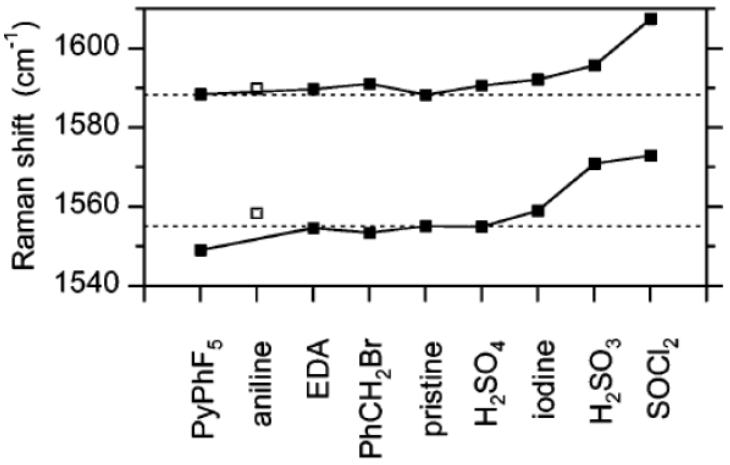

Figure 1.9: Raman shifts of the GM for SWCNTs chemically treated with different molecules as labelled are compared to the values for the pristine sample (dotted lines). The order of samples along the horizontal axis is of increasing conductivity. Aniline data (open squares) are not included in the trend lines. Adapted with permission from (V. Skkalov, A. B. Kaiser, U. Dettlaff-Weglikowska, et al, J. Phys. Chem. B, 2005, 109 (15), pp 7174-7181). Copyright (2005) American Chemical Society.

RRS depends on the electronic structure of SWCNTs. As one-dimensional materials, they have the feature that their density of states (DOS) is not a continuous function of energy, but descends gradually and increases in a spike. The sharp peaks are called Van Hove singularities and the gaps between them are found to be related to the tube diameters. This was presented by Kataura et al. [1999] in the famous Kataura Plot (see Figure 1.10).

In this plot, tubes are denoted by a certain chiral index (n, m), the way of which is illustrated in Figure 1.11.

For Raman scattering, the resonance condition was given by Martin and Falicov [1975] as

$$I(E_{laser}) \propto |\frac{1}{(E_{laser} - E_{ii} - i\Gamma)(E_{laser} \pm E_{ph} - E_{ii} - i\Gamma)}|^2 \qquad (1.4)$$

where I is the intensity of Raman scattering, E_{laser} is the laser energy, E_{ii} is the transition energy (gap between Van Hove singularities), E_{ph} is the energy of a specific phonon mode, and Γ is the broadening factor deriving from the life time of the resonant states. Because Γ is usually tiny compared to other terms, the Raman intensity will increase significantly when either the incident photon at E_{laser} or the outgoing photon at $E_{laser} \pm E_{ph}$ (+ for anti-Stokes and - for Stokes scattering) matches the transition energy E_{ii} (resonance). Practically,

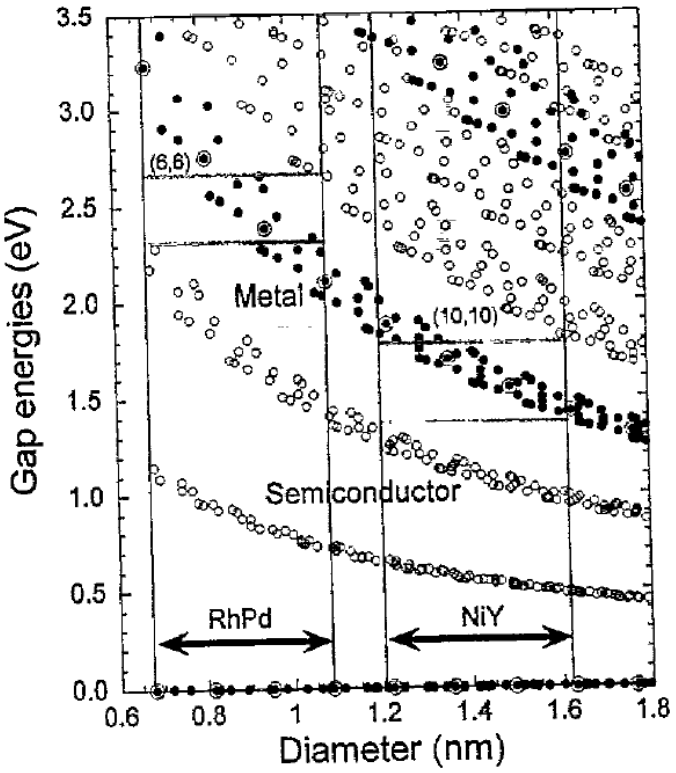

Figure 1.10: "Calculated gap energies between mirror-image spikes in density of states for $\gamma = 2.75$ eV. Solid circles indicate the metallic SWNTs and open circles the semiconducting ones. Double circles indicate the armchair-type SWNTs. Gap energies for all the chiral indexes with larger diameter than (5, 5) are plotted as a function of diameter. Arrows show diameter distributions for the each catalyst. Two horizontal lines in each catalyst area show metallic window in which the optical transitions only by the metallic tubes would be observed." Reprinted figure with permission from [H. Kataura,Y. Kumazawa,Y. Maniwa,I. Umezu,S. Suzuki,Y. Ohtsuka,Y. Achiba, Synthetic Metals 103, 2555–2558 (1999)] Copyright (1999) by the Elsevier.

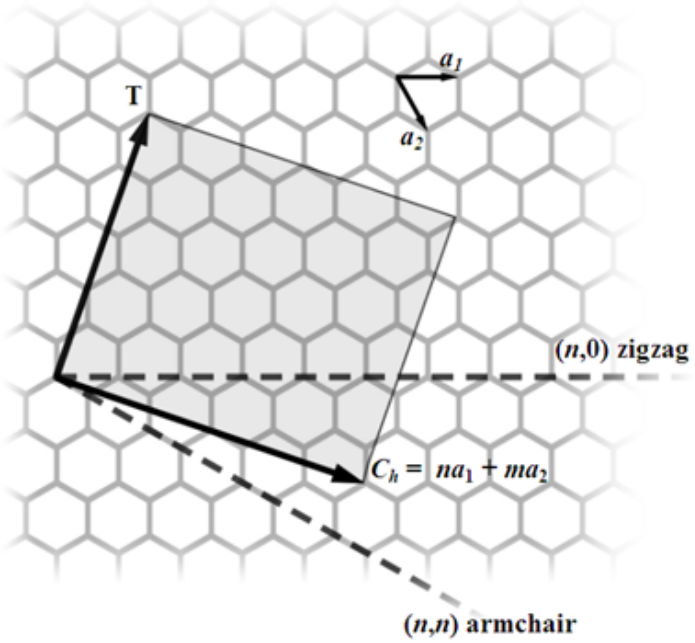

Figure 1.11: "The (n, m) nanotube naming scheme can be thought of as a vector ($\mathbf{C}_h$) in an infinite graphene sheet that describes how to 'roll up' to graphene sheet to make the nanotube. $\mathbf{T}$ denotes the tube axis, and $\mathbf{a}_1$ and $\mathbf{a}_2$ are the unit vectors of graphene in real space." Reproduced from `https://en.wikipedia.org/wiki/Carbon_nanotube` and based upon similar diagrams found in the literature.

the amount of such increase can easily reach up to 10^6. Therefore, at selected laser excitation wavelength, we can obtain a Raman spectrum dominated by the SWCNTs of a specific diameter, which are in resonance. A 3D plot by Fantini et al. [2004] gives a clear demonstration for the radial breathing mode (RBM) (see Figure 1.12). The GM behaves similarly, as long as we pay attention to the E_{ph}, which is about 200 meV for the GM and about 50 meV for the RBM.

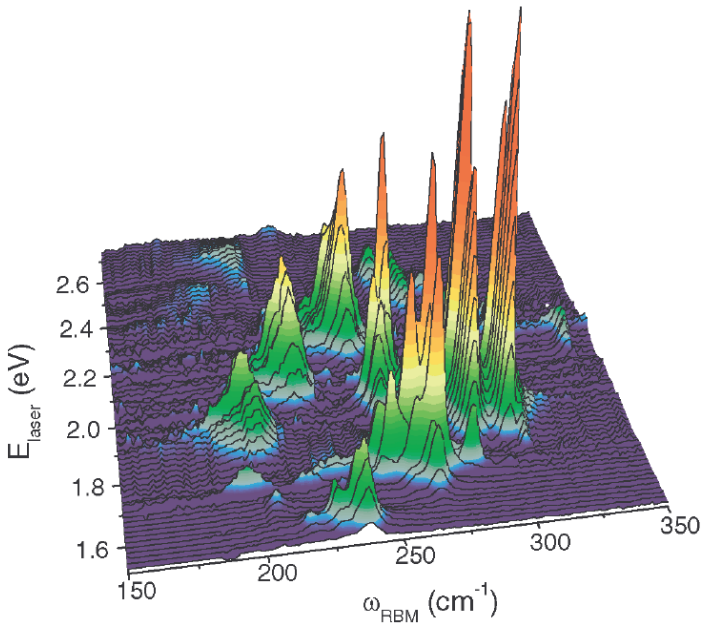

Figure 1.12: The RBM Raman measurements of SWCNTs dispersed in SDS aqueous solution [O'Connell et al., 2002], measured with 76 different laser lines. The non-resonance Raman spectrum from a separated CCl_4 solution is obtained after each of the RBM measurement, and is used to calibrate the intensities of the spectra and to check the frequency calibration. Reprinted figure with permission from [C. Fantini et al., Phys. Rev. Lett. 93, 147406 (2004)] Copyright (2004) by the American Physical Society.

A specific tube diameter corresponds to a unique chirality. In principle, the GM pressure coefficient can be assigned to a specific chirality, while the practical difficulty rises because lots of chiralities may correspond to very similar diameters. The uncertainty can be decreased by a further analysis of the Katuara plot — the branches in Figure 1.10 refer to semiconducting or metallic tubes, which is determined by the chirality [Odom et al., 1998], and the order of transitions (E_{11} for the nearest van Hove singularities and so on). It says that chiralities corresponding to similar tube diameter but belonging to other branches will not contribute to the ambiguity in chirality assignment. Further refinement of the Kataura plot has been carried out by detailed comparison of experiment and

theory. Figure 1.13 by Maultzsch et al. [2005] is a good reference for chirality assignment in RRS experiments of SWCNTS under high pressure, with the caveat that we do not know exactly how the whole diagram shifts with pressure.

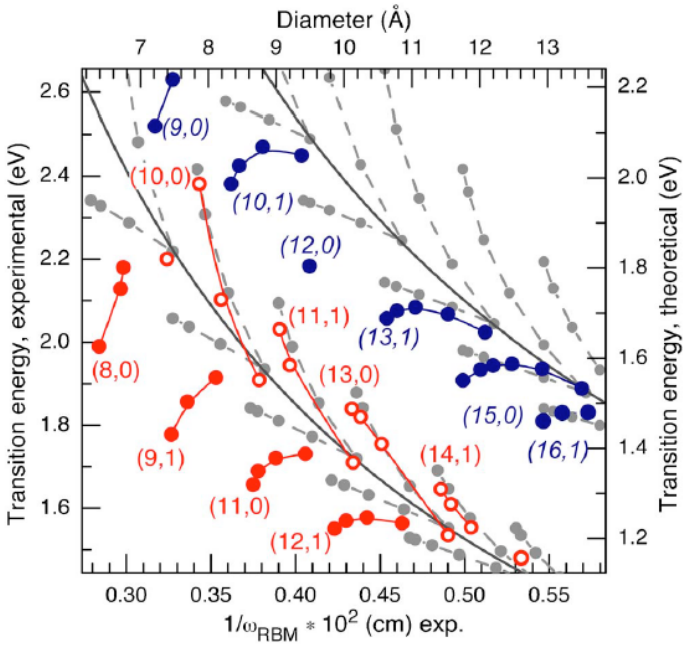

Figure 1.13: "Experimental (large open and closed circles, left and bottom axes) and theoretical (small gray circles, right and top axes) Kataura plot. The second transitions of semiconducting tubes E_{22}^S and the first transitions E_{11}^M of metallic tubes are shown. The solid lines give the approximate 1/d dependence of the transition energies. The dashed lines indicate the 'V'-shaped branches, where the chirality of a tube is related to its left neighbour (n_1, n_2) by $(n_1', n_2')=(n_1-1, n_2+2)$. In the experimental data, the assignment is given for the first tube in each branch, where upright numbers indicate semiconducting and italic numbers indicate metallic tubes. The semiconducting tubes are divided into two families with $\nu=(n_1-n_2) \bmod 3= -1$ (full circles, lower branches) and with $\nu= +1$ (open circles, upper branches)." Reprinted figure with permission from [J. Maultzsch et al., Phys. Rev. B 72, 205438 (2005)] Copyright (2005) by the American Physical Society.

Ghandour et al. [2013] gave an experimental example of achieving the GM pressure coefficient of a specific chirality. This will be discussed in details in Chapter 2.

Experimental data for many more chiralities is required in order to reliably establish a relationship between the GM pressure coefficients and the tube chiralites. Sun et al. [2014] reported the GM pressure coefficient of (6, 5) tubes,

which are of similar diameter to the (9, 1) tubes discussed in Chapter 2. Unexpectedly, the result is very different from the (9, 1) tubes and from the value predicted by the $thick - wall - tube$ model. It will be discussed in details in Chapter 3.

In conclusion, we cannot yet give a clear answer what the GM pressure coefficient is, but we may expect to be able to, after obtaining sufficient chirality-assigned data. At the same time, we need to quantify and understand the exogenous effects such as the laser energy, PTM, doping and bundling on the shift rates, based on variable controlled and of course chirality assignable experiments. The summary of the current understanding of these effects is as follows. First, the laser energy dependence of the GM pressure coefficient shown in Figure 1.7 can be explained that tubes of different chiralities are picked out at different excitation energy. Therefore it is in fact the intrinsic tube chirality dependence. It now makes sense as we do not expect the laser energy to have any effect (only what affects the $C - C$ bond shortening with pressure is expected to have an effect). This however needs to be confirmed by measurements on samples of a single chirality in the same conditions except the excitation energy. Second, it was reported that PTM shift the transition energy [Ghandour et al., 2012] and therefore the PTM effect in Figure 1.7 can be again interpreted as the chirality dependence, as tubes of different chiralities are picked out in different PTM, at the same excitation energy. The PTM should not affect the GM pressure coefficient. Third, doping shifts the GM frequency at ambient pressure but no evidence shows whether it affects the shift rates with pressure. And fourth, understanding bundling effects is more complicated than all the above. CNTs tend to form bundles [Bandow et al., 1998], which means that, if not otherwise specified, all the reported results of GM pressure coefficients are of CNTs bundles. Moreover, bundling effects on the GM pressure coefficient of the tube picked out by RRS may vary with parameters such as the diameters of the surrounding tubes, the bundling configuration (tangled, etc) and the degree of bundling, which is affected by the sample concentration but cannot be precisely controlled. On the other hand, surfactants stably disperse CNTs, which allows to exclude the bundling effects and their uncertainties, while possibly introduces surfactant effects (via the interaction between surfactant molecules and tubes). Early work compared the GM shift rates of individual tubes dispersed by surfactants to the shift rates of bundles (see Figure 1.7) [Christofilos et al., 2007, Lebedkin et al., 2006], but they were not assigned to a specific chirality. The bundling effects will be discussed in Chapter 5.

1.4 Double-wall Carbon Nanotubes (Not What We Expect)

Here I briefly discuss the GM pressure coefficients of double-wall carbon nanotubes (DWCNTs). We expect the outer tube to behave similarly to a SWCNT and the inner tube to be protected by the outer tube from external pressure, because the strong sp^2 bonds, compared with the soft C_{33} of graphite, leads to only a small shrinkage of the outer tube under pressures in the gigapascal range. However, Puech et al. [2006] reported the GM pressure coefficients of the inner tube at 3.3, 4.1 and 5.1 $cm^{-1}GPa^{-1}$ in methanol-ethanol, oxygen and argon, respectively, about 2/3 of the corresponding values of the outer tube. These values vary with the PTM, even there is no contact at all between the inner tube and the PTM. A possible explanation is that the π-electrons compressed through the sp^2 network of the outer wall may act as a PTM and this might be a link to the type of PTM. To investigate the effect of π-electrons behaviour on the pressure dependence of CNTs is the original motivation of our study of graphite and graphene in Chapter 2.

To summarize, we expect the GM pressure coefficients of the outer tubes of DWCNTs to be consistent with the value of the SWCNTs from the thick wall tube model and the inner tubes to be close to zero. They do not appear to be, but more data from tubes assigned to a specific chirality are required.

1.5 Resonance and Effects of Solvents

In this thesis I do not intend to discuss the pressure dependence of the RBM, it is nevertheless necessary to mention it. The RBM, though related to the GM, is a unique signature of CNTs [Rao et al., 1997]. Its vibrational frequency is diameter-dependent and therefore of critical importance to the study of the features, which are related to the tube structure, including the GM pressure coefficients (see Chapter 3).

The RBM is derived from tube structure, first reported by Rao et al. [1997]. The frequency of RBM is proportional to the inverse tube diameter [Reich et al., 2004], which is refined as

$$\omega_{RBM} = \frac{c_1}{d} + c_2 \tag{1.5}$$

where c_1=215 cm^{-1}nm and c_2 was introduced to account for additional external forces from environment [Maultzsch et al., 2005]. So if individual RBM peaks are resolved, the pressure coefficients of RBM obtained in a high pressure measurement can be assigned to tubes of specific chiralities without finely tuning the excitation wavelength to make tubes of only one specific chirality in resonance,

thereby dominating the spectrum.

In this section, I will introduce how the RBM is used to study the effects of solvents on the CNTs resonance condition. A preferable way to present the results is to plot the RBM peak intensity in different conditions, with excitation energy and the RBM frequency. It has to be mentioned that when making the chirality assignment of the RBM peaks according to the Kataura plot, we need to consider both the first and second optical transition (E_{11} and E_{22}). Telg et al. [2007] gave an example for samples of several chiralities (see Figure 1.14). According to the study by Cambré et al. [2010], solvent-filling effect shifted not only excitation energy, but also the RBM frequency, as clearly shown in Figure 1.15. Maultzsch et al. [2005] found small shifts in excitation energy peaks for metallic and semiconducting tubes, but in opposite directions, when the tubes were in two different surfactants. The Figure 1.16 by Ghandour et al. [2012] shows that the effects of solvents and pressure on tubes of a specific chirality are roughly orthogonal to each other — solvents shift the resonance energy without shifting the RBM frequency (with exception of air) and pressure shifts the frequency with only a slight shift in energy.

1.6 Summary

In this chapter, I review the study of the SWCNTs GM under pressure and introduce how the following chapters fit into the big picture. For GM, we give expectations for the pressure coefficients from its origin in graphite (the shift of frequency with pressure is induced by the shortening of $C-C$ bond) and the tube structure (the $thick-wall-tube$ model). Early studies have no consensus on the value of the pressure coefficient. This emphasizes the importance of chirality assignment in high pressure studies of the GM. For the future work, we think the study of CNTs under pressure relies on high resolution Raman spectroscopy equipped with a tunable laser, as RRS not only picks out specific tubes but also significantly increases their Raman signals.

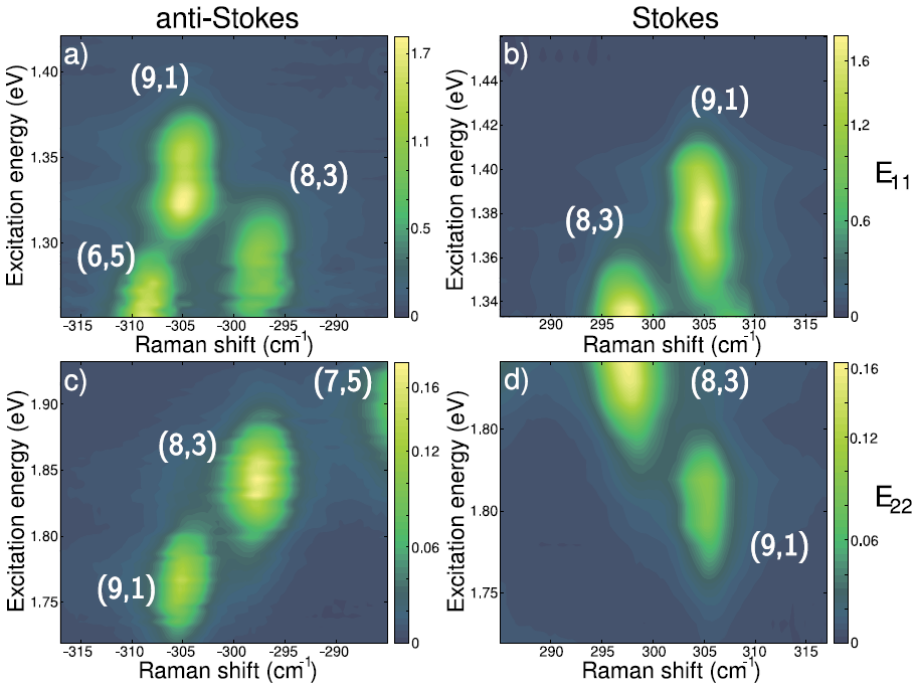

Figure 1.14: "The plotted intensities are proportional to the Raman susceptibility. Upper plots contain anti-Stokes(a) and Stokes(b) Raman spectra excited resonantly via E_{11}. Lower plots show anti-Stokes(c) and Stokes(d) spectra in resonance with E_{22}." Reprinted figure with permission from [H. Telg, J. Maultzsch, S. Reich, C. Thomsen, Phys. Status Solidi (b) 244, 4006–4010 (2007)] Copyright (2007) by John Wiley and Sons.

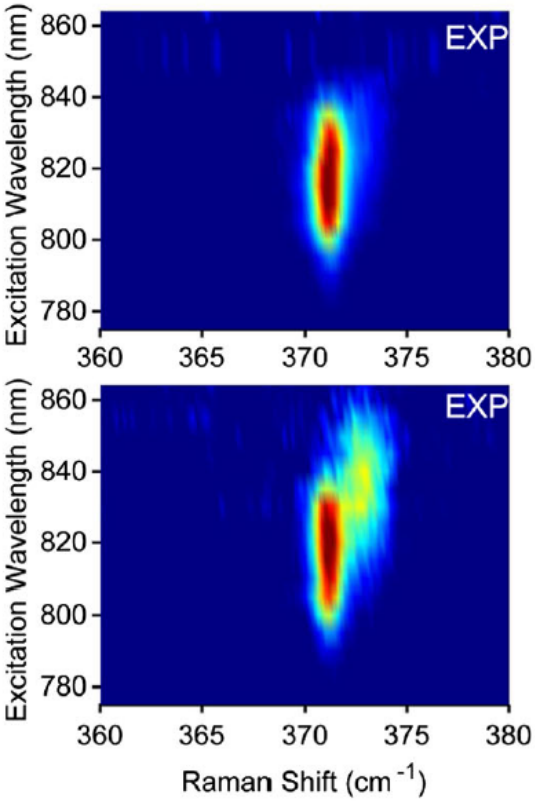

Figure 1.15: The Raman-excitation maps of the first electronic transition of the (5, 4) tubes. The sample used for the upper panes contains less open (solvent-filled) tubes than the sample used for the lower ones. Reprinted figure with permission from [Sofie Cambré et al., Phys. Rev. Lett. 104, 207401 (2010)] Copyright (2010) by the American Physical Society.

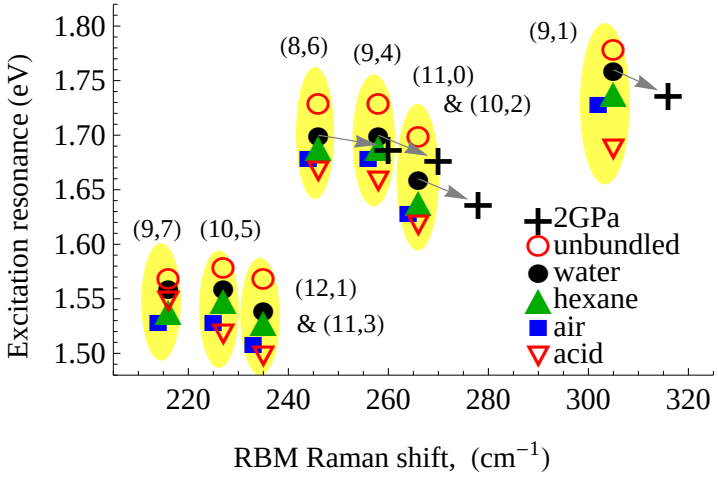

Figure 1.16: Data points corresponding to the RBM frequency and the excitation resonance energy for HiPCO semiconducting nanotubes with the chiral indices (m, n) labelled. The squares are for dry nanotubes in air; the down triangles for sulphuric acid; the up triangles for hexane. The solid circles are for bundled tubes in water and the open circles for unbundled in water with surfactant. Data taken under the pressure of 2GPa is shown by the crosses (+) for bundled nanotubes in water. The arrows show the shifts due to pressure. After Figure 2 of Ghandour et al. [2012].

1.7 Associated publications

Portions of the work detailed in this thesis have been presented in international scholarly publications, as follows:

- Chapter 2: Section 2.1 was published in **Proceedings in the Applied Mathematics and Mechanics** [Sun et al., 2013].

  Section 2.2 and 2.3 were just accepted by **Physical Review B** (arXiv:1502.04323).

- Chapter 3: Published in **Physical Review B** [Ghandour et al., 2013].

- Chapter 4: Published in **High Pressure Research** [Sun et al., 2014].

- Chapter 5: This work was submitted to **Journal of Physical Chemistry C** (arXiv:1411.5832).

- Chapter 6: Published in **Proceedings in the Applied Mathematics and Mechanics** [Sun et al., 2013].

Chapter 2

Graphene and Graphite Under Strain

This chapter demonstrates our study of the vibrational frequency of the in-plane phonon modes of graphene and graphite under strain. I will start with a simple one-dimensional *ball and spring* model to explain the marked sublinearity of the experimental in-plane phonon pressure dependence of graphite, and then show the problem in determining the relationship between strain and the phonon frequency from a two-dimensional analysis. Finally and most importantly, I will present our recent work introducing a quantified significant contribution of out-of-plane compression to in-plane phonon frequency, which was entirely ignored previously and might help to understand the vital environmental effects on graphene.

2.1 One-dimensional Analysis

This section explains the sublinearity of the GM pressure dependence of graphite.

Because of the unavailability of large single crystals, the best estimation of the elastic constants of graphite come from inelastic X-ray scattering techniques [Bosak and Krisch, 2007]. These experiments gave the full C_{ij} stiffness tensor, with $C_{11} = 1109$, $C_{33} \approx 38.7$, $C_{12} = 139$, $C_{13} \approx 0$ and $C_{44} = 4.95$ GPa. For an interlayer spacing of 3.35Å, in-plane 2D values of $C_{11} = 423$ and $C_{12} = 49$ Nm^{-1} may be used. This C_{ij} tensor is consistent with the results from *ab initio* Density Functional Theory (DFT).

The same experiments also detected the energies of all the phonons of graphite. Knowing these energies allows for determining interatomic force constants. Using stretching, in-plane bending and out-of-plane bending (torsion) motions,

Mohr et al. [2007] found that it is necessary to consider interactions up to the fifth nearest neighbour, yielding a total of fifteen force constants. Of these, the C-C stretch between the nearest neighbour is the dominant one, with a force constant of 25.88 eVÅ^{-2}.

In Raman spectroscopy, the G-mode ($E_{2g}^{(2)}$) phonon at 1581 cm^{-1} is the most important, as it is fully allowed and observed in all graphite, graphene and CNTs. Hanfland et al. [1989] and subsequent authors have measured its pressure coefficient of graphite, obtaining values of 4.7 cm^{-1}GPa^{-1} with a marked sublinearity. The question to answer is, if these values can be explained by the theoretically or experimentally derived interatomic force constants discussed above. The harmonic force constant for a C-C pair of atoms performing in-line antiphase motion (bond stretching) corresponding to 1581 cm^{-1} is readily calculated, and is 54 eVÅ^{-2}. In the force constant model of Mohr et al. [2007], this indicates that over half the force constant comes from elsewhere than the stretching constant 25.88 eVÅ^{-2} between the nearest neighbour. However, only nearest-neighbour potentials include the repulsive term due to atomic core overlap, and this is by far the fastest-changing term with atomic separation (e.g. r^{-12} in the Lennard-Jones potential), so it might be expected that the pressure coefficient would come largely from the increase of this stretching constant with pressure. This increase is due to the shift of the bond length to smaller than its equilibrium (at zero pressure) values when the pressure is increased and reflects the aharmonicity of the bond stretching potential. The three-parameter Morse potential fits *ab initio* theoretical data well. For the case of DFT data corresponding to the generalized gradient approximation (GGA) of the exchange and correlation potential, Holec et al. [2010] explicitly show that the sp^2 stretch potential is well fitted by

$$E(r) = E_0[(1 - \exp[-\beta(r - r_0)])^2 - 1] \tag{2.1}$$

with E_0=6.13 eV, β=1.85 Å^{-1} and r_0=1.43 Å. These values correspond to a k=$\partial^2 E/\partial r^2$ of 42 eVÅ^{-2} and ω_G=$\sqrt{2k/m}/2\pi$c = 1380 cm^{-1}. Again one must suppose other contributions to the G-mode force constant, and again supposing them to be independent of pressure. We then obtain a pressure coefficient of 3.8 cm^{-1}GPa^{-1}, derived from pressure induced change in force constant, which is rather low. Walther et al. [2001] reported MD modelling of carbon nanotubes in water in which they used a Morse potential with parameters which gives a still lower pressure coefficient. The sublinearity of the pressure dependence is very small until we include the reduction in the in-plane force due to the large

compression of the c-axis under pressure. We have

$$c_{33}(P) = c_{33} + Pc'_{33} \Rightarrow a_{33}(P) = a_{33}(1 + \frac{c'_{33}P}{c_{33}})^{-\frac{1}{c'_{33}}} \Rightarrow F = \frac{P}{a_{33}(P)} \qquad (2.2)$$

so that the in-plane biaxial force F on the graphene sheet is sub-linear with pressure. The in-plane biaxial strain gives an atomic bond-length *r(P)* and hence a spring constant *k(P)*,

$$r(P) = r_0(1 - \frac{F}{c_{11}^{2D} + c_{12}^{2D}}) \Rightarrow k(P) = \left.\frac{\partial^2 E(r)}{\partial r^2}\right|_{r=r(P)} \qquad (2.3)$$

The resulting expression for $\omega_G(P)$ is plotted in Figure 2.1. It is interesting that the fit is poor if we let the other contributions required above to give 1580 cm^{-1} be pressure-independent; on the other hand, if we simply multiply k by the factor 27/22 to obtain 1580 cm^{-1} then the whole curve $\omega_G(P)$ fits the data very well with no free fitting parameters. A possibility is that GGA usually underestimates bonding, which is responsible for the low frequency and pressure coefficient, and therefore is likely the reason of the multiplication.

To summarise the understanding of the mechanical properties of graphite which we will carry forward to a consideration of nanotubes, the elastic properties and the vibrational frequency of the G-mode are reasonably well-explained by the known properties of the sp^2-bonded structure, but it is less clear whether the pressure-dependence of the G-mode is adequately accounted for in this way, whereas the sublinearity comes from the relatively fast stiffening C_{33} under pressure.

There is no reason to distinguish the elasticity and G-mode frequency of graphene from graphite. Nevertheless, opposing results can be found in literature. Some authors reported a frequency of the G-mode to 1590 cm^{-1} in graphene(e.g. Mohiuddin et al. [2009]) – while others did not (e.g. Nicolle et al. [2011]). This discrepancy is attributed to effects of the environment, but without a definitive explanation. A finer calculation requires taking both GGA's underestimation of bonding and pressure independent contribution of other parts (bending and torsion) from Morse potential to the force constant into consideration and possibly it will be necessary to invoke the behaviour of the π-orbitals under pressure.

2.2 Two-dimensional Analysis

Strain, induced by compression or tension, modifies properties of graphene. Strain determination and monitoring are therefore of critical application impor-

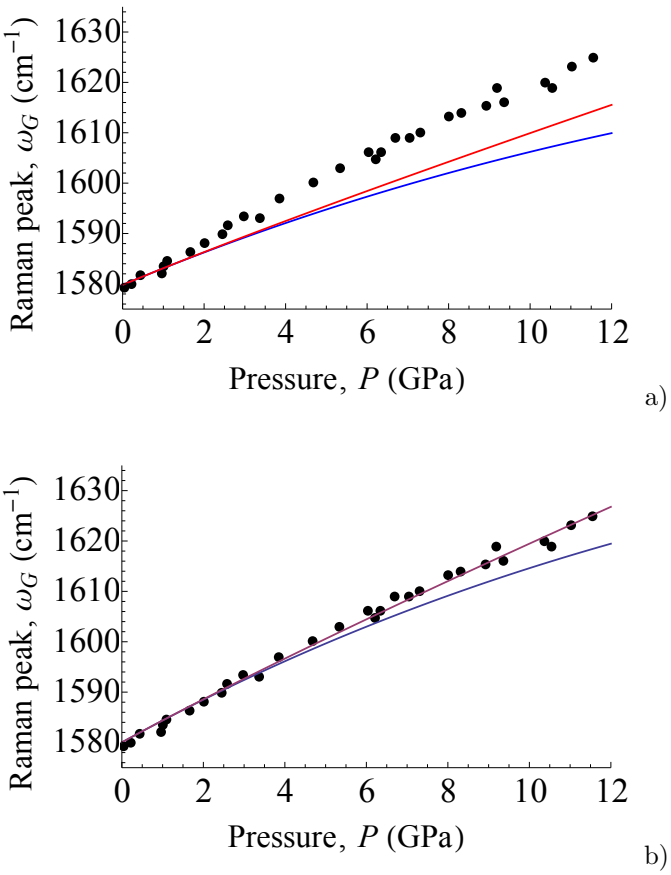

Figure 2.1: "Hanfland et al. [1989]'s experimental data (black dots) of the GM frequency of graphite under applied pressure, is plotted. The theoretical lines are calculated as described in the text, when we take a) other contributions(bending and torsion) to k pressure independent and then b) multiply k by the factor 27/22. In both a) and b) blue lines are without the stiffening of c_{33} with pressure, and red lines are with c'_{33}=10.3." Adapted from Sun et al. [2013].

tance and contribute to the characterization and understanding of graphene. Strain is related to phonon frequencies, which can be directly obtained by experiments. The analysis, rather naturally, is two-dimensional. Thus the frequency shifts of the graphene E_{2g} mode are considered as entirely induced by in-plane strain.

Stacking graphene sheets forms graphite. The in-plane vibrational modes E_{1u} and $E_{2g}^{(2)}$ of graphite are derived from the graphene E_{2g} mode, and from the two dimensional analysis, all these three modes are expected to have the same shift rate [Thomsen et al., 2002, Mohiuddin et al., 2009, Reich et al., 2000, Proctor et al., 2009, Ding et al., 2010, Sun et al., 2013] with in-plane strain. The problem is that the shift rates are not the same. That is what we investigate here by density functional theory (DFT) calculations Hohenberg and Kohn [1964], Kohn and Sham [1965] of graphite under non-hydrostatic conditions.

Huang *et al.* gave the dynamical equations of the graphene optical phonon modes E_{2g} as [Huang et al., 2009]

$$\sum_{\beta} K_{\alpha\beta} u_{\beta} = \omega^2 u_a \tag{2.4}$$

where $\mathbf{u}$=(u_1,u_2) is the relative displacement of the two carbon atoms in the unit cell, ω is the phonon frequency, and K is the force constant tensor, which can be expanded in powers of strain as

$$K_{\alpha\beta} = K^0_{\alpha\beta} + \sum_{lm} K^{\varepsilon}_{\alpha\beta lm} \varepsilon_{lm} \tag{2.5}$$

$K^{\varepsilon}_{\alpha\beta lm}$ has only two independent elements because of the hexagonal lattice, so Eqs. 2.4 and 2.5 may also be written as

$$\begin{pmatrix} \omega_0^2 + A\varepsilon_{xx} + B\varepsilon_{yy} & 0 \\ 0 & \omega_0^2 + B\varepsilon_{xx} + A\varepsilon_{yy} \end{pmatrix} \begin{pmatrix} u1 \\ u2 \end{pmatrix} = \omega^2 \begin{pmatrix} u1 \\ u2 \end{pmatrix} \tag{2.6}$$

where A and B are the two independent elements of $K^{\varepsilon}_{\alpha\beta lm}$ and ω_0 is the unperturbed frequency. Thomsen *et al.* expressed the solution to the secular equation of Eq. 2.6 with the Grüneisen parameter and shear deformation potential (SDP) as [Thomsen et al., 2002]

$$\frac{\Delta\omega}{\omega_0} = \gamma(\varepsilon_{xx} + \varepsilon_{yy}) \pm \frac{1}{2} SDP(\varepsilon_{xx} - \varepsilon_{yy}) \tag{2.7}$$

Eq. 2.7 makes explicit the two-dimensional nature of the analysis. The Grueneisen parameter γ and the SDP are the two key parameters and a number of experimental [Mohiuddin et al., 2009, Huang et al., 2009, Ni et al., 2008, Proctor

Table 2.1: The Grüneisen parameter and SDP obtained from various experiments and calculations of graphene. The values in square brackets are the corrections by Ghandour *et al.* [Ghandour et al., 2013]

Experiments	γ	SDP
uniaxial strain(beam flexure) [Huang et al., 2009]	0.69[0.58]	0.38[0.435]
uniaxial strain(beam flexure) [Mohiuddin et al., 2009]	1.99[1.34]	0.99[1.31]
uniaxial strain(substrate stretch) [Ni et al., 2008]	1.5	
hydrostatic pressure [Proctor et al., 2009]	1.99	
hydrostatic pressure [Soldatov et al., 2012]	2.3	
Calculations		
uniaxial strain [Mohiuddin et al., 2009]	1.87	0.92
uniaxial strain [Mohr et al., 2009]	1.83	1.18
biaxial strain [Mohiuddin et al., 2009]	1.8	
hydrostatic and shear strain [Thomsen et al., 2002]	2.0	0.66

et al., 2009, Soldatov et al., 2012] and theoretical [Mohiuddin et al., 2009, Mohr et al., 2009, Thomsen et al., 2002] papers reported work on graphene under strain to define their accurate values. The results are shown in TABLE 2.1. It is worth noticing that Ghandour *et al.* pointed out that the transverse strain ε_T=0 rather than ε_T=-$\nu\varepsilon_L$, where ν is the in-plane Poisson's ratio and ε_L is the longitudinal strain, in the case that uniaxial strain is applied by flexure of a beam to which a graphene flake adhered [Ghandour et al., 2013].

For graphite, when two adjacent graphene layers are considered, we can simply make two copies of Eq. 2.6, as

$$\begin{pmatrix} \omega_0^2 + A\varepsilon_{xx} + B\varepsilon_{yy} & 0 & C & 0 \\ 0 & \omega_0^2 + B\varepsilon_{xx} + A\varepsilon_{yy} & 0 & C \\ C & 0 & \omega_0^2 + A\varepsilon_{xx} + B\varepsilon_{yy} & 0 \\ 0 & C & 0 & \omega_0^2 + B\varepsilon_{xx} + A\varepsilon_{yy} \end{pmatrix} \begin{pmatrix} u1 \\ u2 \\ u3 \\ u4 \end{pmatrix} = \omega^2 \begin{pmatrix} u1 \\ u2 \\ u3 \\ u4 \end{pmatrix} \tag{2.8}$$

where C is added to account for the interlayer coupling. The longitudinal modes are not coupled with the transverse modes, giving the zero elements. Eq. 2.7 still applies and the weak interlayer coupling is usually neglected. Thomsen *et al.* obtained the corresponding Grüneisen parameter as 2.0 [Thomsen et al., 2002], from the experimental data of graphite under hydrostatic pressure [Hanfland et al., 1989].

We are now able to demonstrate the problem more explicitly — if the frequency shifts of the in-plane modes are induced by in-plane strain alone, as shown in Eq. 2.7, for graphene, the shift rates of E_{2g} with in-plane strain (therefore the Grüneisen parameter) should be the same no matter how the strain is applied and for graphite, E_{1u} and $E_{2g}^{(2)}$ modes should have the same shift rates as the graphene E_{2g}, also no matter how the strain is applied (hydrostatic or

biaxial). This is against the results shown in TABLE 2.1 and previous high pressure studies on graphite — that is, E_{1u} shifts faster than $E_{2g}^{(2)}$ under hydrostatic pressure [Hanfland et al., 1989, Abbasi-Perez et al., 2014, Cousins and Heggie, 2003].

The difference between them could be a consequence of the compression of the π-electrons changing the in-plane bonds. To quantify this effect, we model uniaxial strain and uniaxial stress along the out-of-plane c-axis, and hydrostatic pressure. To describe the results, it is necessary to introduce a new parameter γ' to relate out-of-plane strain to its contribution to the shift of the in-plane phonon frequencies.

The rest of this chapter employs DFT. Graphite was studied at 0 K using DFT [Hohenberg and Kohn, 1964, Kohn and Sham, 1965] as implemented in the Vienna Ab initio Simulation Package (VASP) [Kresse and Furthmuller, 1996]. The exchange-correlation effects were treated within the generalised gradient approximation as parameterized by Perdew, Burke and Ernzerhof [Perdew et al., 1996] and the projector augmented-wave method pseudopotentials [Kresse and Joubert, 1999] for carbon were used. To reach highly accurate results, we used 900 eV plane-wave cut-off energy, and the reciprocal unit cell was sampled with 18x18x9 k-mesh. Van der Waals effects were included using the Grimme method [Grimme, 2006] as implemented in the VASP code. The elastic properties were evaluated using the stress-strain method [Yu et al., 2010]. The vibrational frequencies at the Brillouin zone centre, the Γ point, were calculated using the $2\times2\times2$ supercell employing the finite displacement method as implemented in the Phonopy code [Togo et al., 2008].

First of all, we obtain the optimized geometry for unstrained graphite, as the in-plane bond length of $a = 1.42$Å. and the interlayer distance of $c = 3.20$Å. The errors relative to the experimental values [Hanfland et al., 1989] are 0.06% and 4.6%. The vdW add-on is included, nevertheless the interlayer interaction is not so well-described as the in-plane covalent bonding. The LDA calculation (without vdW) usually gives a better agreement to the experimental value of the interlayer distance, however this is considered to be a coincidence because LDA is a local approximation which overestimates bonding. To minimize the effects of calculating vdW inaccurately , we study the bond anharmonicity under compressive strain, where the vdW attractive potential plays only a small role compared to the dominant repulsion. The error in the value of interlayer distance would not affect the phonon frequency shift rates with compressive strain as much as it would under tensile strain.

We then model hydrostatic pressure on graphite by setting a smaller unit cell volume than the unstrained, optimizing the geometry at that certain volume, and calculating the corresponding sp^2 bond length, interlayer distance,

pressure and phonon frequencies. The frequencies of the E_{1u} and $E_{2g}^{(2)}$ modes of unstrained graphite are 1565.2 and 1559.1 cm^{-1}, respectively. The errors relative to the experiments are 1.4% and 1.3% [Hanfland et al., 1989, Nemanich et al., 1977]. We assume that they are linked to the vdW attractive term and so they would not affect the shift rates with compressive strain. Phonon frequencies are plotted against pressure in Fig. 2.2, as is the standard for presenting experimental data. And the pressure, now as a calculation output, is plotted against the input here — the unit cell volume. (L) and (T) refer to two orthogonal in-plane vibrations, longitudinal and transverse. The frequency difference between these two under hydrostatic condition is less than 0.4 cm^{-1} for both E_{1u} and $E_{2g}^{(2)}$ and the shift rates of (L) and (T) with pressure are the same in the case of the E_{1u} and $E_{2g}^{(2)}$. Therefore, here and in the following calculation, we treat the differnce between longitudinal and transverse modes as computational error and will study the longitudinal modes alone as a representative. Linear least square fits give the shift rates with compressive pressure up to 10 GPa at 5.3 and 4.3 $cm^{-1}GPa^{-1}$ for E_{1u} and $E_{2g}^{(2)}$ modes, respectively. No experimental data for E_{1u} exists and the shift rates for $E_{2g}^{(2)}$ are 4.1–4.6 [Hanfland et al., 1989, Liu et al., 1990, Sandler et al., 2003]. In the previous theoretical work, Cousins *et al.* obtained 4.74 and 4.67 $cm^{-1}GPa^{-1}$ for E_{1u} and $E_{2g}^{(2)}$ modes [Cousins and Heggie, 2003], while Abbasi-Pérez *et al.* [Abbasi-Perez et al., 2014] got 5.0 and 4.3 $cm^{-1}GPa^{-1}$. To summarize, the calculation results are reliable and reasonable, with the shift rates with pressure comparable to previous work, with observable sublinearity of the frequency shift due to the pressure dependence of the elastic constant C_{33}, and with the two in-plane modes degenerate when the graphene layers are pulled apart. However, the problems are again the different shift rates for E_{1u} and $E_{2g}^{(2)}$ with pressure, and the behaviour of the frequency starting off vertically upwards with pressure (see FIG. 2.2). The latter point implies that the pressure (force) may be inaccurately calculated under tensile stress (pressure remains at about -2GPa when the unit cell volume keeps increasing), where vdW plays an important part. We will resolve the former point and we avoid the latter point by focusing on the compressive part.

Modelling non-hydrostatic condition helps to investigate problems found under hydrostatic condition. The only study of graphite under non-hydrostatic condition reported so far is that of Abbasi-Pérez *et al.*. They suggested that the contribution to the shift of the in-plane phonon frequency from the out-of-plane compression is so little that it can be neglected [Abbasi-Perez et al., 2014]. The following results do not agree with that.

We model uniaxial strain along the c-axis of graphite by varying the interlayer distance while fixing the in-plane geometry. The phonon frequencies and out-of-plane stress are calculated at each interlayer distance and fixed sp^2 bond

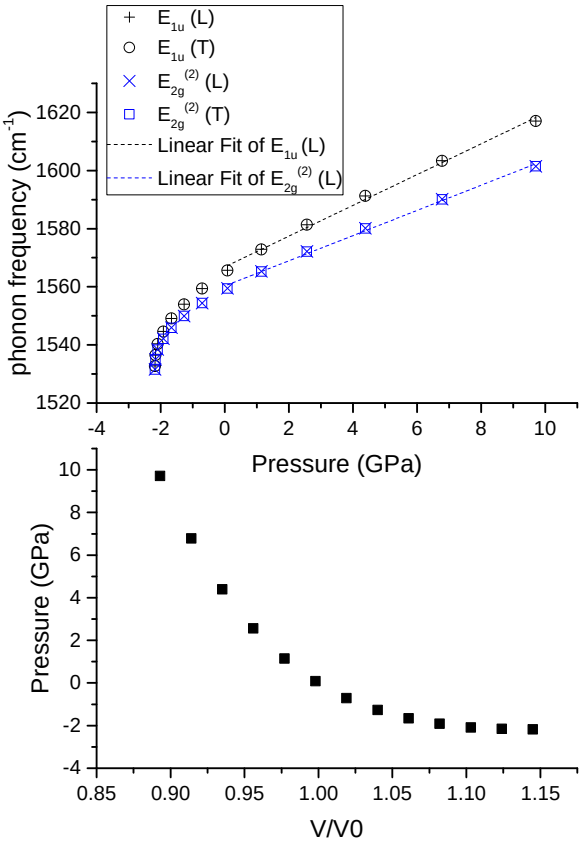

Figure 2.2: (colour online) [Modelling] Graphite under hydrostatic pressure. The frequencies of the graphite E_{1u} and $E_{2g}^{(2)}$ are plotted against pressure. The pressures are plotted against the unit cell volumes at which they are calculated. V_0 is the unit cell volume of unstrained graphite. The linear fit of the phonon frequencies at compressive pressure up to 10 GPa is presented as dashed lines, black for E_{1u} and blue for $E_{2g}^{(2)}$.

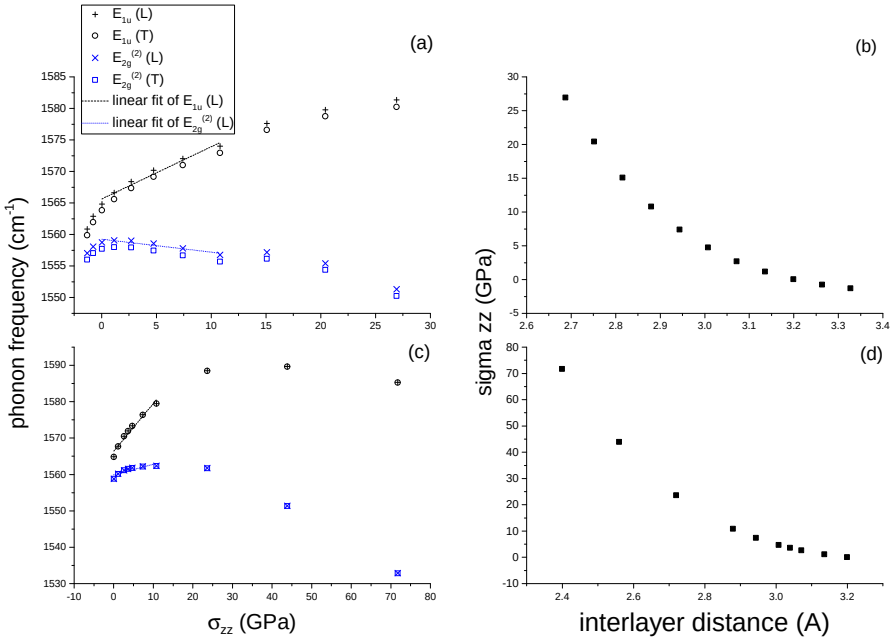

Figure 2.3: (colour online) [Modelling] Graphite under uniaxial strain / stress along the c-axis. The frequencies of the graphite E_{1u} and $E_{2g}^{(2)}$ are plotted against out-of-plane stress in the case of uniaxial strain (a) and uniaxial stress (c). The out-of-plane stresses are plotted against the interlayer distances at which they are calculated, in the case of uniaxial strain (b) and uniaxial stress (d). The linear fit of the phonon frequencies at compressive stress to about 10 GPa is presented as dashed lines, black for E_{1u} and blue for $E_{2g}^{(2)}$.

length. FIG. 2.3 (a) shows the shifts of the in-plane phonon frequencies against out-of-plane stress along c-axis. In FIG. 2.3 (b), the stress as a calculation output, is plotted against the input — the interlayer distance in this case. The shift rates with stress up to about 10 GPa, by least square linear fits, are 0.8 and -0.2 $cm^{-1}GPa^{-1}$ for E_{1u} and $E_{2g}^{(2)}$, respectively. It is worth noticing that the elastic constant C_{13}, determining the Poisson's ratio ν_{zx}, is poorly defined due to the structural anisotropy of graphite, but can be considered to be close to zero [Bosak and Krisch, 2007]. Our calculated C_{13} value is -10.5 GPa, and the corresponding ν_{zx} is -0.024. Therefore, uniaxial compressive strain here induces in-plane tensile stress. The degeneracy of the two modes can be again seen in this case when the graphene sheets are pulled apart. The problem is that the E_{1u} and $E_{2g}^{(2)}$ modes shift with opposite signs.

Next we consider uniaxial stress on graphite along the c-axis, by varying the interlayer distance and optimizing the in-plane geometry at each interlayer distance. The phonon frequencies, the out-of-plane stress and the sp^2 bond

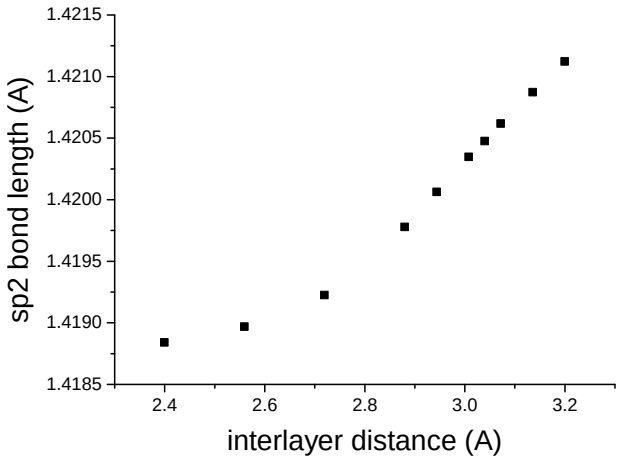

Figure 2.4: (colour online) [Modelling] Graphite under uniaxial stress along c-axis. The sp^2 bond length is plotted against the interlayer distance, at which it is calculated.

length are calculated at each interlayer distance. The effect of the negative Poisson's ratio can now be clearly illustrated in FIG. 2.4 as the in-plane bond is also compressed as we compress along the c-axis. The amount, however, is tiny. FIG. 2.3 (c) presents the in-plane phonon frequency against out-of-plane stress and again the output stress is plotted against the input interlayer distance in FIG. 2.3 (d). The shift rates with stress up to 10 GPa in this case are 1.3 and 0.3 $\mathrm{cm}^{-1}\mathrm{GPa}^{-1}$ for E_{1u} and $\mathrm{E}_{2g}^{(2)}$, respectively. The shift rate with uniaxial stress for the E_{1u} is about a quarter of the shift rate under hydrostatic stress; this is large enough to be significant.

It is usual to present frequency against stress, because stress is considered as input in experiments. However, the atomic positions (strain) determine properties such as phonon frequency, and it is therefore helpful to plot the frequencies against strain. To be specific, for graphite, the shifts of the frequencies of the in-plane modes E_{1u} and $\mathrm{E}_{2g}^{(2)}$ are considered to be induced by in-plane strain. So we plot the phonon frequencies against in-plane strain under hydrostatic and non-hydrostatic conditions and then obtain the corresponding Grüneisen parameters $\gamma_{E_{1u}}$ and $\gamma_{E_{2g}^{(2)}}$ for the E_{1u} and $\mathrm{E}_{2g}^{(2)}$ modes, respectively, according to Eq. 2.7. Values for the two modes should be the same from the two dimensional nature of Eq. 2.4–2.7.

In the case of uniaxial strain, the phonon frequencies for both modes shift at fixed in-plane geometry. The Grüneisen parameters are hence $\gamma_{E_{1u}}=\infty$ and $\gamma_{E_{2g}^{(2)}}=\infty$, according to Eq. 2.7.

In the case of uniaxial stress, in FIG. 2.5 (a) we plot the in-plane phonon frequencies against the sp^2 bond length, which is calculated by optimizing the in-plane geometry at each interlayer distance. The top axis of in-plane strain is converted from the sp^2 bond length by $\varepsilon = (a - a_0)/a_0 \times 100\%$, where ε is the in-plane strain, a is the sp^2 bond length and a_0 is the sp^2 bond length of unstrained graphite. This is the same data as in FIG. 2.3. We apply a linear fit to the data points under compression up to about 10 GPa (the same as in FIG. 2.3), and obtain the shift rates $\partial\omega_{E_{1u}}/\partial\varepsilon$=-152.00 cm^{-1}/% and $\partial\omega_{E^{(2)}_{2g}}/\partial\varepsilon$=-35.50 cm^{-1}/%, which correspond to $\gamma_{E_{1u}}$=4.86 and $\gamma_{E^{(2)}_{2g}}$=1.14.

In the case of hydrostatic pressure, in FIG. 2.5 (b) we plot in-plane phonon frequency against the sp^2 bond length, which is calculated by the geometry optimization at each unit cell volume. The top axis of in-plane strain is converted in the same way as before. The data is the same as in FIG. 2.2. We apply a linear fit to the data points under compression up to about 10 GPa (the same as in FIG. 2.2) and get the shift rates $\partial\omega_{E_{1u}}/\partial\varepsilon$=-69.20 cm^{-1}/% and $\partial\omega_{E^{(2)}_{2g}}/\partial\varepsilon$=-56.59 cm^{-1}/%, corresponding to $\gamma_{E_{1u}}$=2.21 and $\gamma_{E^{(2)}_{2g}}$=1.81.

We present the Grüneisen parameters obtained in the case of uniaxial stress and hydrostatic pressure in FIG. 2.5 and compare them to that of uniaxial strain and those reported in TABLE 2.1. The values for the E_{1u} and $E^{(2)}_{2g}$ modes obtained under hydrostatic condition are in good agreement with the most values of the E_{2g} mode of graphene presented in TABLE 2.1. Similar agreement has been reported in the literature; this is the quantitative reason why the in-plane phonon frequency shifts were considered as induced by in-plane strain alone [Thomsen et al., 2002, Mohiuddin et al., 2009, Reich et al., 2000, Proctor et al., 2009, Ding et al., 2010]. However, the difference between the values of the E_{1u} and $E^{(2)}_{2g}$ modes grows and neither of the values agrees with the E_{2g} of graphene, under uniaxial stress, where the relative out-of-plane compression to in-plane is considerably larger than it is under hydrostatic pressure. Under uniaxial strain, where there is only out-of-plane strain, the difference of the frequency shifts can be considered as infinity. The out-of-plane strain is responsible for the difference of the Grüneisen parameters for the E_{1u} and $E^{(2)}_{2g}$ modes. Regarding the amount of the difference, to include the out-of-plane strain contribution to the in-plane phonon frequency is desirable in the case of hydrostatic pressure (where the 'good agreement' is actually with the presence of errors in TABLE 2.1) and definitely necessary in the cases of uniaxial strain and stress.

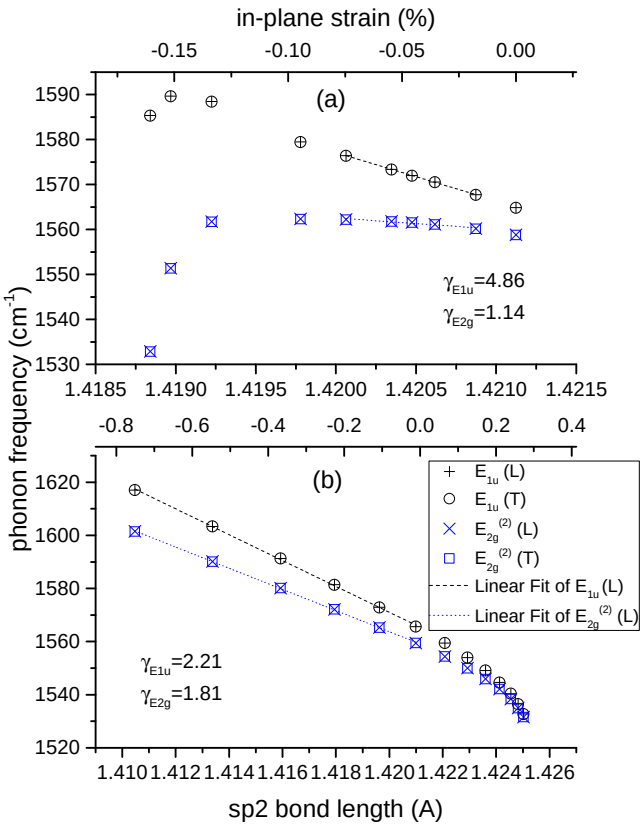

Figure 2.5: (colour online) [Modelling] Graphite under uniaxial stress along c-axis (a) / hydrostatic pressure (b). The data in (a) is the same as in Figure 2.3 (c) and the data in (b) is the same as in Figure 2.2. Here the frequencies of the graphite E_{1u} and $E_{2g}^{(2)}$ are plotted against in-plane sp^2 bond length, which is calculated at each interlayer distance (a) / unit cell volume (b). The top axis of in-plane strain is converted from the sp^2 bond length by $\varepsilon = (a - a_0)/a_0 \times 100\%$. The linear fit of the phonon frequencies at compressive stress to about 10 GPa is presented as dashed lines, black for E_{1u} and blue for $E_{2g}^{(2)}$. The Grüneisen parameters for both modes, obtained from the linear fit, are presented in each case for comparison to the values in TABLE 2.1.

2.3 Three-dimensional Analysis

To quantify this contribution, we suggest refining Eq. 2.8, as

$$\begin{pmatrix} \omega_0^2 + A\varepsilon_{xx} + B\varepsilon_{yy} + D\varepsilon_{zz} & 0 & C + E\varepsilon_{zz} & 0 \\ 0 & \omega_0^2 + B\varepsilon_{xx} + A\varepsilon_{yy} + D\varepsilon_{zz} & 0 & C + E\varepsilon_{zz} \\ C + E\varepsilon_{zz} & 0 & \omega_0^2 + A\varepsilon_{xx} + B\varepsilon_{yy} + D\varepsilon_{zz} & 0 \\ 0 & C + E\varepsilon_{zz} & 0 & \omega_0^2 + B\varepsilon_{xx} + A\varepsilon_{yy} + D\varepsilon_{zz} \end{pmatrix} \begin{pmatrix} u1 \\ u2 \\ u3 \\ u4 \end{pmatrix} = \omega^2 \begin{pmatrix} u1 \\ u2 \\ u3 \\ u4 \end{pmatrix} \tag{2.9}$$

where D and E are the additional two independent parameters. The solutions of the secular equation of Eq. 2.9 are

$$\begin{aligned} \omega_{(1)}^2 &= \omega_0^2(E_{2g}^{(2)}) + (A+B) \times \varepsilon_{in-plane} + (D+E) \times \varepsilon_{zz} \\ \omega_{(2)}^2 &= \omega_0^2(E_{2g}^{(2)}) + (A+B) \times \varepsilon_{in-plane} + (D+E) \times \varepsilon_{zz} \\ \omega_{(3)}^2 &= \omega_0^2(E_{1u}) + (A+B) \times \varepsilon_{in-plane} + (D-E) \times \varepsilon_{zz} \\ \omega_{(4)}^2 &= \omega_0^2(E_{1u}) + (A+B) \times \varepsilon_{in-plane} + (D-E) \times \varepsilon_{zz} \end{aligned}$$

where ε_{xx} is equated to ε_{yy} for all the three cases in this paper and C accounts for the separation of the frequency of the E_{1u} and $E_{2g}^{(2)}$ modes of unstrained graphite. For small shifts, $\omega^2 - \omega_0^2 \approx 2\omega_0(\omega - \omega_0)$, we now have a new parameter γ', relating out-of-plane strain to its contribution to in-plane phonon frequency for Eq. 2.7 as

$$\frac{\Delta\omega}{\omega_0} = -\gamma(\varepsilon_{xx} + \varepsilon_{yy}) \mp \frac{1}{2}SDP(\varepsilon_{xx} - \varepsilon_{yy}) - \gamma'\varepsilon_{zz} \tag{2.10}$$

where $\gamma = (A+B)/2\omega_0^2$, $\gamma'_{E_{1u}} = (D+E)/2\omega_0^2$ and $\gamma'_{E_{2g}^{(2)}} = (D-E)/2\omega_0^2$. Alternatively, we can preserve the true hydrostatic term $(\varepsilon_{xx} + \varepsilon_{yy} + \varepsilon_{zz})$ as

$$\frac{\Delta\omega}{\omega_0} = -\gamma(\varepsilon_{xx} + \varepsilon_{yy} + \varepsilon_{zz}) \mp \frac{1}{2}SDP(\varepsilon_{xx} - \varepsilon_{yy}) - (\gamma' - \gamma)\varepsilon_{zz} \tag{2.11}$$

We believe this out-of-plane contribution is mostly related to the compression of the π electrons, which is beyond the picture of the force constant model.

Let us now return to Eq. 2.10. In the case of uniaxial strain, where the shifts of the frequencies are entirely from the out-of-plane strain, we plot the in-plane phonon frequencies against the interlayer distance — the calculation input, in FIG. 2.6 (a) and fit the data under compression up to about 10 GPa (the same as in FIG. 2.3 (a)). The top axis of out-of-plane strain is converted from interlayer distance by $\varepsilon = (a_{33} - a_{33_0}/a_{33_0}) \times 100\%$, where ε_o is the out-of-plane strain, a_{33} is the interlayer distance and a_{33_0} is the value of unstrained graphite.

The shift rates for the E_{1u} and $E_{2g}^{(2)}$ modes are $\partial\omega_{E_{1u}}/\partial\varepsilon$=-0.915 cm^{-1}/% and $\partial\omega_{E_{2g}^{(2)}}/\partial\varepsilon$=0.204 cm^{-1}/%, corresponding to $\gamma'_{E_{1u}}$=0.0585 and $\gamma'_{E_{2g}^{(2)}}$=-0.0131, according to Eq. 2.10. They are small, but non-negligible as the out-of-plane strain is about 30 times larger than the in-plane strain under hydrostatic condition (the anisotropy of graphite) and can be even larger under non-hydrostatic conditions. It is worth noticing that the in-plane phonon frequency cannot be considered as an indicator of the in-plane bond stiffness in this case as the E_{1u} and $E_{2g}^{(2)}$ modes, both representing the in-plane bond stiffness, shift with opposite signs under out-of-plane compressive strain. Now we have quantified the out-of-plane strain contribution by γ', which is responsible for the separating of the E_{1u} and $E_{2g}^{(2)}$ modes and then the in-plane γ can be the same in various conditions for the two modes (and the E_{2g} of graphene) as it should be from its definition.

Finally, we calculate the refined value for the in-plane γ from Eq. 2.10, by $\gamma'_{E_{1u}}$ and $\gamma'_{E_{2g}^{(2)}}$ obtained under uniaxial strain. For both modes, in the case of uniaxial stress and hydrostatic pressure, we calculate the contribution to the shifts of the frequencies from out-of-plane strain by γ' and attribute the rest to the in-plane strain. And from that we obtain the refined in-plane γ.

We plot the in-plane phonon frequencies against interlayer distance, which is the calculation input under uniaxial stress in FIG. 2.6 (b) and calculated by the geometry optimization at each unit cell volume under hydrostatic pressure in FIG. 2.6 (c). The top axis of the out-of-plane strain is converted from the interlayer distance in the way as mentioned above. The data is the same as in FIG. 2.3 (c) and 2.2, for uniaxial stress and hydrostatic pressure, respectively. We obtain the shift rates for the two modes at the same pressure range as before. Under uniaxial stress, we obtain $\gamma_{E_{1u}}$=1.84 and $\gamma_{E_{2g}^{(2)}}$=2.01 from the results shown in FIG. 2.5 (a) and 2.6 (b). Under hydrostatic pressure, the values are $\gamma_{E_{1u}}$=1.85 and $\gamma_{E_{2g}^{(2)}}$=1.90, from the results shown in FIG. 2.5 (b) and 2.6 (c).

The proposed Eq. 2.10 describes the graphite E_{1u} very well, while the error in the $E_{2g}^{(2)}$ mode is due to the non-linear relationship between out-of-plane strain and the shifts of the frequencies, as shown in FIG. 2.6 (a). This indicates a more complicated relation of out-of-plane strain to in-plane phonon frequency, when the two adjacent graphene layers vibrate in-phase ($E_{2g}^{(2)}$) than out-of-phase (E_{1u}). We consider the refined value of the $\gamma_{E_{1u}}$ as a reliable one, relating in-plane strain to in-plane phonon frequency of both graphite and graphene, which excludes any out-of-plane contribution. An additional term to refine the non-linear effect for the $E_{2g}^{(2)}$ mode could be introduced but should await further work — either initial experimental evidence or, theoretically, the evolution of

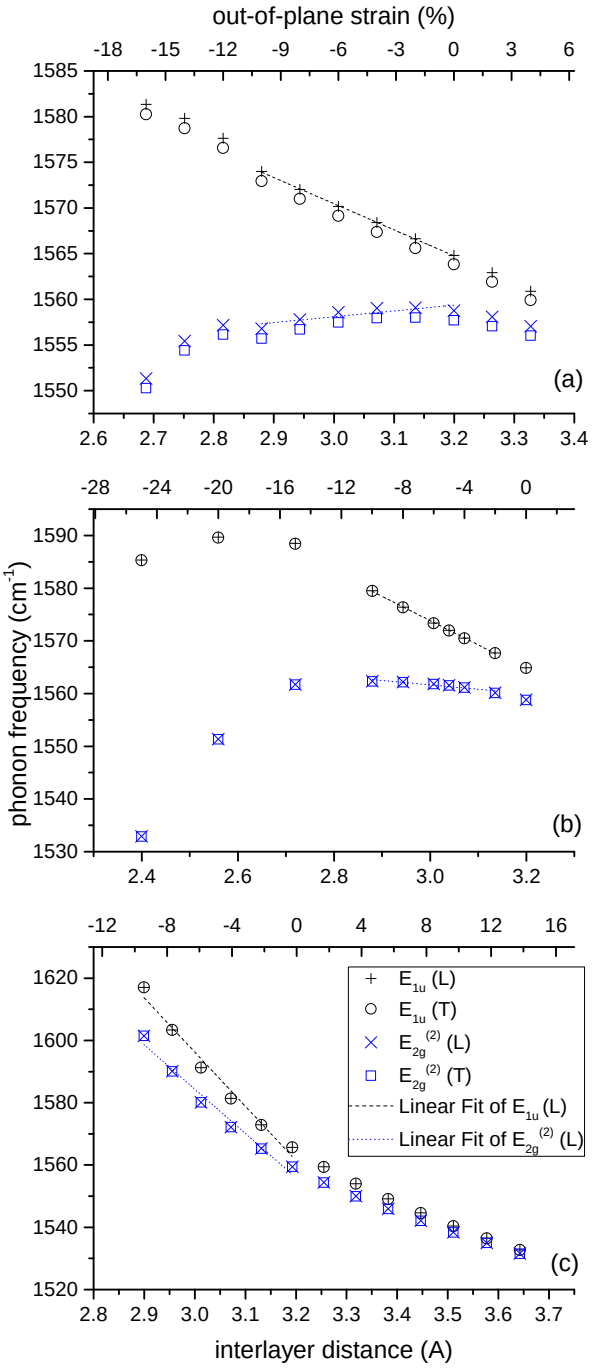

Figure 2.6: (colour online) [Modelling] Graphite under uniaxial strain (a) / uniaxial stress (b) / hydrostatic pressure (c). The frequencies of the in-plane modes of the graphite E_{1u} and $E_{2g}^{(2)}$ are plotted against interlayer distance, which is the calculation input in the case of (a)&(b) and is calculated at each unit cell volume in the case of (c). The top axis of out-of-plane strain is converted from interlayer distance by $\varepsilon = (a_{33} - a_{33_0}/a_{33_0}) \times 100\%$. The linear fit of the phonon frequencies at compressive stress to about 10 GPa is presented as dashed lines, black for E_{1u} and blue for $E_{2g}^{(2)}$.

the π-electrons may be visualized under compression to give a clearer picture of the phenomenon to be quantified. Further analysis can also be done to study the phase transition induced by the change of interlayer distance, which has clear signs in the presented results, namely the significant drop of phonon frequency in FIG. 2.3 (b), 2.5 (a) and 2.6 (b) under large compression.

As a result of this work, for existing [Abbasi-Perez et al., 2014, Pena-Alvarez et al., 2014] or future study of in-plane phonon frequency of graphite under uniaxial compression along c-axis, we suggest an additional contribution from out-of-plane strain by γ' and for the study of graphene, we suggest a reliable in-plane γ, based on which the disparity in different cases (uniaxial/biaxial in-plane strain, hydrostatic pressure, with/without substrate, etc.) can be attributed to the behaviour of the π-electrons.

To summarize Section 2.2&2.3, we model uniaxial strain, stress along c-axis and hydrostatic pressure on graphite and calculate the vibrational frequencies of the in-plane modes derived from the graphene E_{2g} mode. The shifts of the frequencies come from both in-plane and out-of-plane compression. We quantify the contribution from out-of-plane strain by a new parameter γ' and therefore refine the existing value of the Grüneisen parameter γ. This contribution is responsible for the separating shifts of the E_{1u} and $E_{2g}^{(2)}$ modes of graphite under hydrostatic pressure and therefore non-negligible, against previous conclusion. It can be significant under non-hydrostatic condition. The reliable value of the in-plane Grüneisen parameter can be used for strain calibration in various applications and for further refinement of studying the π-electron behaviour.

Chapter 3

The Diameter Effect on the GM Pressure Coefficients of Carbon Nanotubes

This chapter presents the experimental work employing Raman Spectroscopy equipped with a wavelength-tunable laser to obtain the GM pressure coefficients of SWCNTs, each assigned to a specific chirality and we explain the diameter dependence of the GM pressure coefficients with a thick-wall tube model.

Studies of the mechanical properties of single-walled carbon nanotubes are hindered by the availability mostly of ensembles of tubes with a range of diameters. Raman spectroscopy with tunable excitation picks out identifiable tubes. The pressure coefficient of the GM varies with diameter consistent with the thick-wall tube model. Reappraisal of data for graphene and graphite suggests revision of the G-mode Grüneisen parameter γ and the shear deformation parameter β values towards 1.34.

Raman spectroscopy has been used extensively for investigating the structural, mechanical and vibrational properties of SWCNTs. The GM at about 1600 cm^{-1} derives from the bulk graphite in-plane E_{2g} mode while the low-frequency radial breathing mode (RBM) is a consequence of the tube structure. The pressure dependence of these modes carries key information about the bond anharmonicity and the mechanical strength of the curved graphene sheet. However, the Raman signal is highly resonant and nanotube samples usually contain a large number of different diameters and chiralities, denoted by the chiral indices (n, m). The Raman spectrum is dominated by those tubes for which the excitation photon energy or the Raman photon energy match the electronic transition energies E_{ii} [Kataura et al., 1999, Fantini et al., 2004]. As well as

shifting with pressure [Ghandour et al., 2012, Deacon et al., 2006] the electronic transition energies are also highly sensitive to the nature of the solvent or hydrostatic PTM in which the nanotubes are immersed [Ghandour et al., 2012, Deacon et al., 2006, Merlen et al., 2005]. The result is that different nanotubes are in resonance, for any given laser excitation energy, in different solvents, and with increasing pressure different tubes come in and out of resonance [Dunstan and Ghandour, 2009]. As a consequence, unambiguous determination of the pressure coefficients of the Raman peaks is complicated, and, most remarkably, especially for the RBM, no clear difference between (solvent) filled and empty tubes has yet been reported [Merlen et al., 2005].

A large body of published work has shown that resonant Raman spectroscopy of carbon nanotubes at ambient pressure, in which both the RBM shift ω_{RBM} and the resonance energy E_{ii} are measured, giving peaks on a two-dimensional surface to which chiral indices (n, m) can be assigned. This work began with the Kataura plot of theoretical E_{ii} values against diameter for all (n, m) [Kataura et al., 1999]. More recent experimental and theoretical work refined this plot so that identification of many peaks from their (ω_{RBM}, E_{ii}) position is now unambiguous [Maultzsch et al., 2005, Telg et al., 2007, Araujo et al., 2009, Fantini et al., 2004]. Whilst the bulk of these studies concern unbundled nanotubes in water with surfactant, different shifts have been observed with different surfactants [Maultzsch et al., 2005], and the effect of filling open tubes with water has also been reported [Cambré et al., 2010].

We have reported large shifts in the E_{ii} co-ordinate of some (n, m) nanotubes in the form of bundles in different solvents (water, hexane, sulphuric acid) and in air [Ghandour et al., 2012]. In contrast, high pressure with water as the PTM (solvent) gives a shift which is mainly in the ω_{RBM} coordinate [Ghandour et al., 2012]. This showed that solvent effects and pressure effects are distinct, and opens the way to obtaining reliable pressure coefficients for each (n, m), not only for the RBM mode but also for the G mode . To do this, it is necessary to find a sparse region of the (ω_{RBM}, E_{ii}) map so that the G mode resonance observed can be identified with the RBM resonance and hence with a specific chirality or diameter. Here we demonstrate this by obtaining the RBM and G-mode pressure coefficients for three peaks in the (ω_{RBM}, E_{ii}) map. Results for the RBM agree well with previous authors. For the G-mode the results are not as expected from the current interpretation of the pressure dependence of the graphene and graphite equivalents of the GM — an issue which we address here.

HiPCO SWCNTs (see Appendices) were used as bought (powder) from NanoIntegris Inc., without debundling (see Appendices), in water as the PTM. The spectra were obtained using a triple spectrometer (see Appendices) equipped

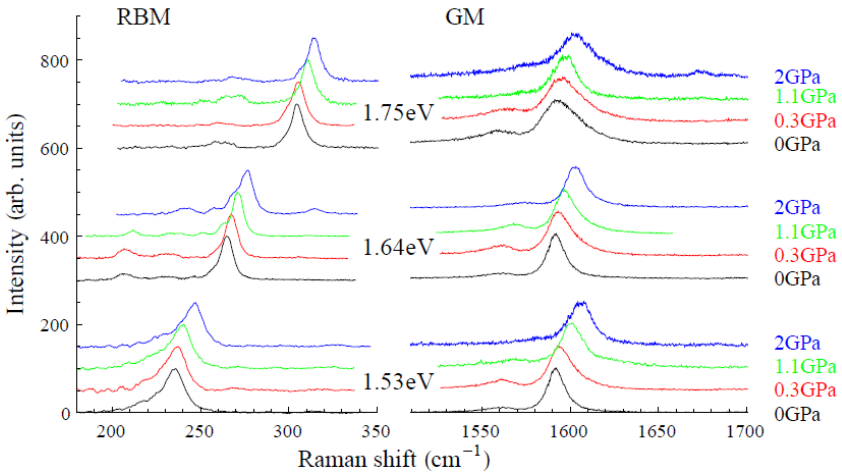

Figure 3.1: "The RBM and G-mode spectra for the excitation energies and pressures marked, offset vertically for clarity. The spectra under 1.75-eV excitation (upper group) are assigned to the (9, 1) chirality, the spectra under 1.64-eV excitation (middle group) to the (11, 0) and (10, 2) chiralities, and the spectra under 1.53 eV (lower group) to the (12, 1) and (11, 3) chiralities." Reprinted figure with permission from [A. J. Ghandour et al., Phys. Rev. B 87, 085416 (2013)] Copyright (2013) by the American Physical Society.

with a Ti-sapphire laser over the excitation range 1.48 eV – 1.78 eV at intervals of about 10 meV. At each excitation energy, Raman spectra were recorded over the range 210 cm^{-1} - 320 cm^{-1} to capture the RBM peaks, and from 1500 cm^{-1} - 1700 cm^{-1} for the G-band spectra. The RBM spectra are fitted with Lorentzian peaks (giving the positions ω_{RBM}), and the intensity of each peak is plotted against the laser wavelength. The laser excitation energy giving maximum RBM intensity is taken as E_{ii} for that peak. We presented the Kataura plot thereby obtained, with the chiralities assigned by comparison with the results of Araujo et al. [2009, 2010] in Ghandour et al. [2012]. Given the chiralities (n, m), the diameters are calculated as $d = a\pi^{-1}\sqrt{(n^2 + nm + m^2)}$ where a = 0.246 nm is $\sqrt{3}$ times the C-C bond length. At laser wavelengths near 1.75 eV there is a single dominant peak in the RBM spectrum (Figure 3.1) that is assigned to the (9, 1) chirality (d = 0.747 nm). At 1.64 eV the peak assigned to the (11, 0) (d = 0.861 nm) and (10, 2) (d = 0.872 nm) chiralities dominates the spectrum, and at laser wavelengths near 1.53 eV it is the (12, 1) (d = 0.981nm) and (11, 3) (d = 1.000 nm) peak which dominates. At most other excitation wavelengths there are two or more strong peaks in the RBM spectrum.

If there are two or more strong peaks in the RBM spectrum then the G-band peak would contain contributions from both of the corresponding chiralities or diameters. When a single RBM peak dominates the spectrum, it might be hoped

that the G-band peak would be largely due to the same diameter tube. However, resonances with E_{ii} may occur with the outgoing Raman photon, and the effect on the Raman intensity is the same [Fantini et al., 2004]. The resonance with the Stokes Raman photon is shifted up in energy and the resonance with the anti-Stokes Raman photon is shifted down relative to the resonance with the excitation photon. For the RBM, the energies are too close to be resolved, and this effect merely broadens and shifts the resonance by 10 – 20 meV ($\hbar\omega_{RBM}$). However, for the G-mode of any given tube, this effect gives peaks about 200 meV ($\hbar\omega_{GM}$) apart in excitation energy. Consequently, any given excitation energy may be in resonance with one tube for the excitation photon, giving both the RBM and the G-mode Raman peaks of that tube, and it may also be in resonance with the Raman (Stokes) G-mode photon of another tube, giving the G-mode Raman peak but not the RBM peak for that tube. To determine whether there may be other contributions of this sort to the G-mode peak when we observe only one RBM peak requires considering where these resonances are on the Kataura plot.

Figure 3.2 shows the Kataura plot for the RBM resonances for the HiPCO nanotubes bundled in water in the range of excitation energies used [Ghandour et al., 2012]. The predicted incident and Stokes resonances for the G-mode are also shown. We see that the 1.53 eV excitation energy which excites the (12, 1) and (11, 3) tubes risks slightly exciting the larger (10, 5) and (9, 7) tubes, but not more in the G-band than in the RBM. The 1.64 eV excitation is close only to the target (11, 0) and (10, 2) tubes. The 1.75 eV excitation, aimed at the (9, 1) tubes, comes close to exciting the Stokes photon resonance of the large (10, 5) and (9, 7), but is not on the peak. We consider below what the consequences on the interpretation of our data would be if there were significant excitation of these tubes via their G-mode Stokes Raman photon. At lower and higher energies, there are no other tubes or E_{ii} states giving resonances that would be excited.

The pressure experiments were carried out in a DAC (see Appendices) operated in the Zen configuration (using a single diamond [van Uden and Dunstan, 2000], see Appendices), which permits good control over the pressure in the range 0 – 2 GPa. The pressure was measured using the standard technique of ruby photoluminescence [Mao et al., 1986]. The dependence of the RBM spectra and the G-band spectra on pressure is shown in Figure 3.1 for the three excitation wavelengths. The peak positions are plotted in Figure 3.3 with linear least-squares fits to obtain the pressure coefficients. To estimate the errors due to scatter, and also because the 2 GPa points may have increased error due to the freezing of the water PTM above 1 GPa, least-squares fits to the data for the three lower pressures are also shown.

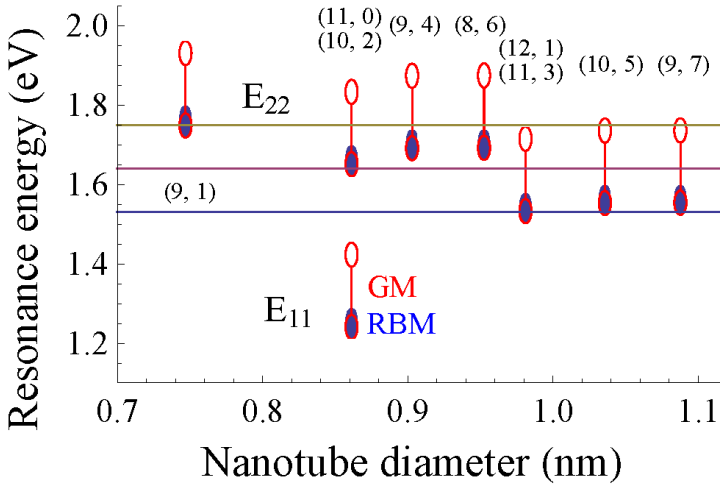

Figure 3.2: "The solid ellipses represent the observed RBM resonances for HiPCO nanotubes bundled in water, reported in Ghandour et al. [2012]. The expected resonances for the G-mode are shown by the open ellipses; for each tube diameter the lower ellipse is for the resonance with the incident photon and the upper ellipse for the resonance with the Stokes Raman photon. The lines joining the upper and lower ellipses represent the non-zero intensity between the two peaks." Reprinted figure with permission from [A. J. Ghandour et al., Phys. Rev. B 87, 085416 (2013)] Copyright (2013) by the American Physical Society.

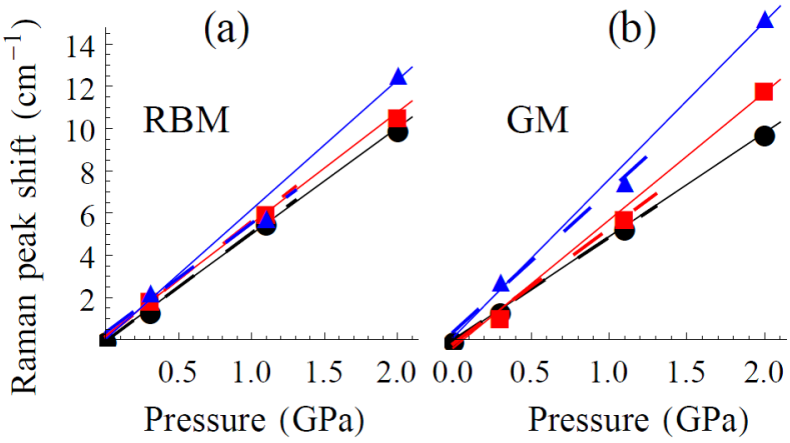

Figure 3.3: "Shifts with pressure for (a) the RBM peaks, and (b) the G-mode peaks, for the three excitation energies of Figure 3.1. The solid lines are linear least-squares fits to the whole datasets, while the dashed lines are fits to the lower three pressure points." Reprinted figure with permission from [A. J. Ghandour et al., Phys. Rev. B 87, 085416 (2013)] Copyright (2013) by the American Physical Society.

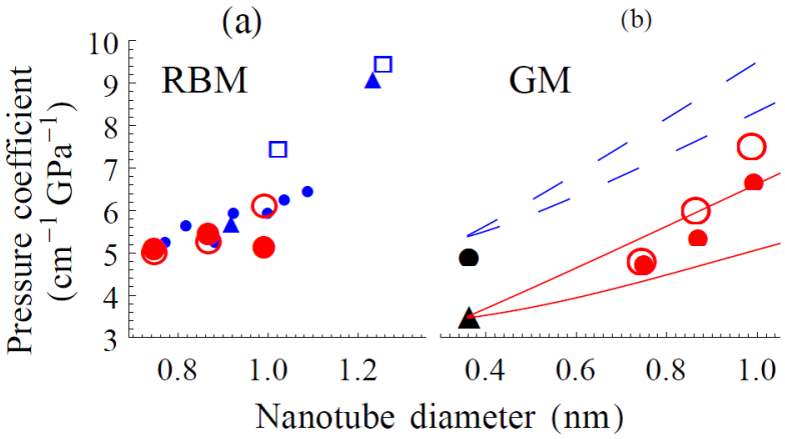

Figure 3.4: Pressure coefficients from Figure 3.3 plotted against the tube diameters for the three excitation energies of Figure 3.1. In (a), the RBM data (large circles) are compared with experimental results for bundled semiconducting tubes in ethanol/methanol (triangles) [Venkateswaran et al., 2003], unbundled semiconducting tubes in water/surfactant (small solid circles) [Lebedkin et al., 2006], and with the MD simulation results for unbundled semiconducting tubes in water from Longhurst and Quirke [2007] (open squares). In (b), the GM data are plotted. The broken lines show the dependence on diameter expected for the G^+ and G^- bands from Eq. 3.3 with the values for γ and β given in Mohiuddin et al. [2009] and the solid lines show the results for the revised values discussed in the text. For comparison, the pressure coefficients of graphite (solid circle) [Hanfland et al., 1989] and graphene (solid triangle) (revised value from the data of Mohiuddin et al. [2009] according to Eq. 3.2 with $\varepsilon_T = 0$) are shown, plotted at $d = w$. Reprinted figure with permission from [A. J. Ghandour et al., Phys. Rev. B 87, 085416 (2013)] Copyright (2013) by the American Physical Society.

In Figure 3.4, the pressure coefficients we measure are plotted against the tube diameters, using solid circles for the fits to the lower pressure points and open circles for the fits that include the 2 GPa data. Literature data for the pressure coefficients of the RBM peaks of semiconducting SWCNTs is also shown. Experimental data is for the RBM of bundled tubes in an ethanol-methanol mixture from Venkateswaran et al. [2003] and the RBM of unbundled tubes in water with surfactant from Lebedkin et al. [2006]. Simulation data is for molecular dynamics (MD) of the RBM of isolated tubes in water from Longhurst and Quirke [2007].

Here I will briefly discuss about the results of the RBM, as they are related to the GM. A striking feature in Figure 3.4 (a) is the excellent agreement of our RBM data with the data for semiconducting debundled tubes of Lebedkin et al. [2006] and for the bundled tubes of Venkateswaran et al. [2003]. Previously,

differences in reported pressure coefficients were attributed to consequences of bundling (e.g. hexagonalisation under pressure [Venkateswaran et al., 2003]) and to the different solvents used as PTM [Dunstan and Ghandour, 2009]. The good agreement between bundled and unbundled tubes in water and unbundled tubes in ethanol-methanol suggests that neither of these factors affects the pressure coefficients. This is a surprising but useful result.

The RBM frequency has been related to the G-band frequency by Venkateswaran et al. [2003] using a continuous elastic medium approximation and by Gerber et al. [2009] using a simple ball-and-spring model. In both analyses good agreement is obtained with the empirical dependence of ω_{RBM} on diameter. Both analyses imply a small RBM pressure coefficient of about 0.8 $\mathrm{d}^{-1}\mathrm{cm}^{-1}\mathrm{GPa}^{-1}$ where the tube diameter d is in nm (before correction for the thick-wall effect, see Eq. 3.1 below), very much less than the values observed. The MD simulations of Longhurst and Quirke [2007] explain this in terms of the interaction between the (unbundled) nanotube and its environment by considering a nanotube surrounded by water molecules at high pressure. The vdW interaction between the nanotube and the first shell of water molecules provides only a small correction to the ambient-pressure RBM frequency, but the increase in the force constant of this interaction with pressure gives the bulk of the RBM pressure coefficient. This is a greater effect for low RBM frequencies (large tubes) than for high (small tubes), giving the dependence of the pressure coefficient on the diameter seen in Figure 3.3 (a). The good agreement of the data for bundled tubes in water, unbundled tubes in water and surfactant, and bundled tubes in ethanol-methanol suggests that the increase in the force constant of the interaction between the nanotube and its environment is similar in all cases. It would seem that the same RBM pressure coefficient (within experimental error) is obtained by the stiffening of the inter-nanotube vdW interaction in nanotube bundles as by the stiffening of the water (or surfactant) vdW interaction with unbundled tubes.

The GM pressure coefficients in Figure 3.4 (b) are remarkably low – in this low-pressure range, values up to 8 or 10 $\mathrm{cm}^{-1}\mathrm{GPa}^{-1}$ have commonly been reported [Dunstan and Ghandour, 2009] – and vary quite fast with diameter. The dependence on diameter may be understood by considering the nanotube as a thick-walled closed tube under external pressure P [Sandler et al., 2003, Elliott et al., 2004]. For an outside diameter of $d + w$ and an inside diameter of $d - w$, with $d > w$, the axial and tangential stresses are greater than the pressure P,

$$\sigma_L = \frac{(d+w)^2}{4dw} P, \sigma_T = \frac{d+w}{2w} P \tag{3.1}$$

These are unequal, so to predict the pressure coefficient we require both the hydrostatic and the shear deformation parameters (mode Grüneisen parameters) γ and β. These are available from the experimental data of Mohiuddin et al. [2009] who studied the Raman G-band in graphene as a function of uniaxial strain, obtained by flexure of a beam to which a graphene flake adhered. Under uniaxial strain, the G-band splits into two components, G^+ and G^-. Dropping unnecessary notation and combining their Eq. 3 with their experimental results, they gave

$$\omega_{\varepsilon_L}^{G^\pm} = \frac{\partial \omega^{G^\pm}}{\partial \varepsilon_L} = -2125 \mp 1045 cm^{-1} = -\omega_0^G \gamma(\varepsilon_L + \varepsilon_T) \pm \frac{1}{2}\omega_0^G \beta(\varepsilon_L - \varepsilon_T) \quad (3.2)$$

where ε_L is the longitudinal strain imposed on the graphene flake by the curvature of the substrate beam. They used the Poisson ratio $\nu = 0.33$ of the substrate to obtain the transverse strain $\varepsilon_T = \nu\varepsilon_L$, and, using the experimental value of $\omega_0 = 1590$ cm^{-1} for the GM frequency at ambient pressure, they obtained the G-mode parameters as $\gamma = 1.99$ and $\beta = 0.99$. The hydrostatic strain coefficient of graphene under hydrostatic pressure P is $\omega_\varepsilon^{G^\pm} = 2\omega_0\gamma = 6340 cm^{-1}$, which, with $(s11 + s12)^{-1} = 1250 GPa$, corresponds to $\omega_P^{G^\pm} = 5.07 cm^{-1} GPa^{-1}$ in good agreement with experimental values for graphite [Hanfland et al., 1989]. However, using $\varepsilon_T = -\nu\varepsilon_L$ for the transverse strain is incorrect. For a thin beam in flexure, as the tensile part above the neutral plane tries to contract laterally and the compressive part below tries to expand, anticlastic curvature develops. Only if the anticlastic curvature is completely unconstrained is $\varepsilon_T = \nu\varepsilon_L$. Otherwise, if the anticlastic curvature is constrained by the beam aspect ratio [Timoshenko and Goodier, 1970] or by the loading contacts, there may be little or no transverse strain – i.e. this may be better treated as a plane strain problem [Timoshenko and Goodier, 1970]. Taking this limiting case and putting $\varepsilon_T = 0$ in Eq. 3.2, gives $\gamma = 1.34$ and $\beta = 1.31$, or to experimental accuracy, $\gamma \sim \beta \sim 4/3$. Then the predicted pressure coefficient for graphene and graphite from the experimental data of Mohiuddin et al. [2009] becomes 3.40 cm^{-1}GPa^{-1}. For the nanotube, using Eq. 3.1 for the axial and tangential stresses under a pressure P and taking $\nu = 0.13 = -s_{12}/s_{11}$, $s_{11} + s_{12} = 1/1250$ GPa as in Mohiuddin et al. [2009], the strains and the pressure coefficients of the $G^\pm$ bands are given by

$$\begin{aligned} \varepsilon_L = s_{11}\sigma_L + s_{12}\sigma_T, \varepsilon_T = s_{12}\sigma_L + s_{11}\sigma_T \\ \varepsilon_H = \varepsilon_L + \varepsilon_T, \varepsilon_S = \varepsilon_L - \varepsilon_T \\ \omega_P^{G^{\pm}} = \omega_0\gamma\varepsilon_H \mp \frac{1}{2}\omega_0\beta\varepsilon_S \end{aligned} \tag{3.3}$$

These curves are plotted in Figure 3.4 (b) against d for w = 0.36 nm for the values of $\gamma = 1.99$ and $\beta = 0.9918$ (broken curves) and these do not agree with the data. They are plotted also for the revised values of $\gamma = 1.34$ and $\beta = 1.31$ (solid curves) and these show good agreement with the data, within experimental uncertainty. In these fits we have not taken into the effect of the wall curvature on the Raman frequencies or pressure coefficients [Aguiar et al., 2012].

Here we should consider also the possible consequence of Figure 3.2, that there may be some contribution to the G-band of the nanotube diameters that we ruled out above. Clearly, if the G-band was always given equally by all nanotube diameters, its pressure coefficient would not vary with excitation energy. Since it does, the observed values must be attributed to the different diameters. However, it is possible that the pressure coefficient we attribute to the (12, 1) and (11, 3) tubes (d = 0.98 nm) with 1.53 eV excitation comes partly from the tubes with diameters up to 1.1 nm. This would improve the agreement in Figure 3.4 (b) between the observed and calculated values.

These results are surprising. With the maximum revision for plane strain of the result of the uniaxial experiment of Mohiuddin et al. [2009] we have good agreement between their data and the data for nanotubes under high pressure. On the other hand, these results are in sharp disagreement with data for graphene and graphite under high pressure, where much higher pressure coefficients are reported. Initial experiments on graphene under hydrostatic pressure [Proctor et al., 2009] gave the GM peak shifts as a function of strain / pressure that were consistent with DFT calculations [Mohiuddin et al., 2009] and simple mechanical models assuming that the Raman peak shifts are due entirely to the bond stiffening when the C-C distance decreases. However, more recent experimental results [Nicolle et al., 2011] showed the graphene GM pressure coefficient varying from 8–11 $\mathrm{cm}^{-1}\mathrm{GPa}^{-1}$ according to the choice of PTM, as observed in nanotubes. If a significant part of the G-mode pressure coefficient derives from interaction with the environment, then it is noteworthy that the uniaxial stress experiment on graphene and nanotubes under pressure (whether bundled or unbundled) have condensed matter (solid or liquid) in contact with one side only of the graphene sheet. In contrast, graphene under pressure and graphite both have condensed matter (solid or liquid) in contact with both sides

of each graphene sheet. Why and by how much environment can affect the C-C bond stiffening under pressure are unclear and without speculating on the origin of the environmental effect, there is scope for it being twice as large in this case. This requires that a significant part of the graphite pressure coefficient is due to interactions between the graphene sheets (each sheet serving as part of the environment of its neighbours). This interpretation also predicts that open tubes which fill with PTM will display a higher pressure coefficient than expected from the data for closed tubes (but independent of diameter). This may explain why no clear difference has been reported between closed tubes, with pressure coefficients raised by the thick-wall effect (Eq. 3.1), and open tubes [Merlen et al., 2005].

In pressure experiments on double-walled nanotubes [Puech et al., 2006], the inner tube has condensed matter on one side only, while the outer tube has it on both sides. The pressure coefficients of the inner tubes (3.3–5.1 $cm^{-1}GPa^{-1}$) are consistently much lower that those of the outer tubes (5.8–8.6 $cm^{-1}GPa^{-1}$) [Puech et al., 2006]. The data were interpreted in terms of the intertube pressure, but the data are also consistent with the environmental effect suggested here.

In conclusion, the data reported here utilise tunable laser excitation to obtain the first reliable pressure coefficients for both the Raman modes of bundled single-walled carbon nanotubes that may be assigned to chirality and diameter. Experimentally, it is clearly urgent to find the GM pressure coefficients for nanotubes for a larger range of diameters, in different solvents, and for open tubes as well as closed. The results for the RBM show that the increase in the force constant of the interaction between the nanotube and its immediate surroundings at high pressure occurs in a similar manner for tubes surrounded by other nanotubes, surfactant or solvent. The results for the G-band are unexpected and have stimulated a correction of the available data for graphene. Theoretically, they suggest the calculation ab initio of graphene, when the π-orbitals are compressed by an adjacent graphite layer or PTM on one side and on both sides. This study represents a major step forward to achieving a unified understanding of the characteristics of graphene-based structures under stress and gives clear guidance as to what further studies are necessary to complete this understanding.

Chapter 4

The Chirality Effect on the GM Pressure Coefficients of Carbon Nanotubes

Following the work in Chapter 3, we intend to obtain the GM pressure coefficient of (6, 5) tubes as a supplement. Unexpectedly, due to the significant chirality effect this work develops to the whole chapter.

Here we use 488 nm and 568 nm laser Raman spectroscopy under high pressure to selectively follow evolution of Raman GM signals of SWCNTs of selected diameters and chiralities ((6, 5) and (6, 4)). The GM pressure coefficients of tubes from the work in Chapter 3 are consistent with the thick-wall tube model. Here we report the observation of well-resolved G^- peaks in the Raman spectrum of SWCNTs in a DAC. The pressure coefficients of these identified tubes in water, however, are unexpected, having the high value of over 9 $cm^{-1}GPa^{-1}$ for the G^+ and the G^-, and surprisingly the shift rates of the same tubes in hexane have clearly lower values. We also report an abrupt increase of G^- peak width at about 4 GPa superposed on a continuous peak broadening with pressure.

In Chapter 3, we only reported the G^+ peaks. The GM splits in carbon nanotubes into the G^+ and the G^-, distinguished by their different in-plane vibrational directions, along and perpendicular to the tube axis, respectively, and split by the curvature of the tube wall [Jorio et al., 2002]. The G^- has been observed by many groups. Thomsen et al. [1999] used 514 nm laser excitation to record the GM spectra of arc-discharge-grown SWCNTs samples of diameters ranging from 1.2–1.5 nm. Using a 4:1 methanol-ethanol mixture under pressure, they reported pressure coefficients of 3.7 $cm^{-1}GPa^{-1}$ for both of the two G^- peaks they found in the spectra. Venkateswaran et al. [2001] recorded the

GM spectra of purified arc-discharge-grown SWCNTs samples (bucky paper) of diameters ranging from 1.2–1.5 nm also with 514 nm laser and 4:1 methanol-ethanol mixture, obtaining three G^- peaks with pressure coefficients of 6.1, 5.7 and 5.9 $cm^{-1}GPa^{-1}$, from higher to lower G^- frequency respectively. Christofilos et al. [2006] performed high pressure measurements on SWCNTs material with a diameter distribution from 1.25–1.47 nm in 4:1 methanol-ethanol, with a 647 nm laser, obtaining two G^- peaks with pressure coefficients of 5.9 and 5.8 $cm^{-1}GPa^{-1}$, respectively, from lower to higher frequency. Lebedkin et al. [2006] studied HiPCO SWCNTs with diameters of 0.8–0.13 nm in water with surfactant. Their G^- peaks were too weak to analyze with all three excitations, 514, 633 and 785 nm laser, used in their work. Here we report the pressure coefficients for both the G^+ and the G^-, of tubes assigned to a specific diameter and chirality in water and compare them with the values in hexane.

Besides shifting GM frequency, pressure ovalizes and then squashes tubes. One might expect a broadening of the curvature-sensitive G^- mode due to the continuously varying curvature along the tube wall in an oval phase and a splitting in a collapsed phase [Aguiar et al., 2012]. Here we also report the experimental broadening of the G^- of a specific chirality with pressure.

Room temperature non-polarized Raman spectra were obtained in the backscattering geometry with a Horiba T64000 Raman system (see Appendices) with a confocal microscope in the single mode, a 1800 grooves/mm grating and a 100-μm slit. The system is equipped with a liquid N_2-cooled CCD detector (Jobin-Yvon Symphony) and has a resolution of 0.6 cm^{-1}. Excitation was at 488 nm (equipped with a laser edge filter (see Appendices)) and 568 nm (equipped with a 550 nm Longpass Colored Glass Filter (see Appendices)) lines of a Coherent Innova Spectrum 70C Ar^+-Kr^+ laser, with 514, 520, 531, 647 nm lines also available. It was focused in the DAC with a 20× objective. We kept the power on the sample below 5 mW to avoid laser-heating effects on the probed material and the concomitant softening of the observed Raman peaks. For the high pressure experiments we used a membrane diamond anvil cell (MDAC) (see Appendices) with two diamond anvils of 500 microns of culet size and a very low fluorescence (Type IIa).

We use water and hexane as pressure media in this work, one polar and the other non-polar. It is necessary to take advantage of the established *Kataura* plot to indentify tubes of a specific diameter for a GM spectrum Kataura et al. [1999], as we did in Chapter 3. The Kataura plot has been refined by several groups Maultzsch et al. [2005], Araujo et al. [2010].

CoMoCAT SWCNTs, grown on a silica support with a low mass ratio of Co to Mo, are used as purchased from Sigma-Aldrich Co., without debundling. We choose CoMoCAT tubes for their small diameter (0.8 nm) and narrow range

of diameter distribution($\pm$0.1 nm). In the raw sample powder, carbon is over 90%, in which SWCNTs are over 77% and among the tubes the (6, 5) ones are over 50%, where all the percentages are in mass. There are two main reasons to study bundles in this work: 1) the previous study on the relation between GM pressure coefficient and tube diameter, which we want to compare with, was on bundles. 2) Individualization and surfactant effects are not experimentally separable in water, so the surfactant effect itself on the electronic transition energy E_{ii} and the GM pressure coefficient of tubes is still unclear.

Carbon nanotubes samples usually contain a number of different chiralities, denoted by the chiral indices (n, m). The diameter is given by $d=\frac{a}{\pi}\sqrt{n^2+nm+m^2}$, where a is related to the C-C bond length. The Raman spectrum is dominated by the contribution from tubes when the in-coming laser or out-going Raman photon energy matches the electronic transition energy E_{ii} of these tubes. The *Kataura* plot gives E_{ii} against diameter for all (n, m) [Kataura et al., 1999]. Taking advantage of the Kataura plot, we are able to obtain the Raman spectrum dominated by the GM of a specific chirality at a certain laser excitation energy, which is equal to or 200 meV higher (corresponding to the phonon energy of GM) than the E_{ii} of that tube (see chapter 3).

In this study a perfect resonance condition is not necessary as we are still able to trace the GM of specific diameters under pressure because of the properties of the CoMoCAT samples and so instead of a continuously tunable laser, we perform the measurement with a selection of discrete laser energies.

In water, we use 514, 520, 531 and 568 nm laser to record the RBM spectra and get one dominant peak only with 568 nm, which can be assigned to the (6, 5) tubes according to the *Kataura* plot and the sample property. We also check the RBM spectra with 647 nm (about 200 meV below) and find no dominant peak, suggesting that the contribution from (6, 5) tubes dominates the GM spectra obtained with 568 nm laser. In hexane, we obtain the GM of (6, 5) tubes at the excitation of 488 nm, following the same procedure as in water. Figure 4.1 shows clear G^+ and G^- peaks of (6, 5) in hexane and two well-resolved G^- peaks in water, as the resonance condition for (6, 5) tubes in water with 568 nm laser is not perfect. These are assigned to (6, 5) and (6, 4) according to their transition energies and G^- frequencies [Maultzsch et al., 2005, Jorio et al., 2002].

After selecting a suitable laser energy, we increase the pressure on the samples and obtain their GM spectra, ranging from 1400 cm^{-1} to 1800 cm^{-1}, every 0.5 GPa in the low pressure regime, followed by a gradual increase of intervals up to the 10^{th} pressure point. We present several raw spectra under pressure in Figure 4.1. The Raman intensity decreases with pressure and as a result, in water, the G^- peak of (6, 4) tubes can no longer be resolved above 2.5 GPa. We

fit the Raman peaks by Lorentzian peaks, and plot the frequencies as a function of pressure in Figure 4.2. We stop fitting the G^- of (6, 4) tubes when the peak can hardly be seen at 2.4 GPa. It is worth noticing that the G^+ in Figure 4.2 a) is contributed by both (6, 5) and (6, 4) tubes. The pressure coefficients are obtained by linear least-square fits and then plotted as a function of diameter in Figure 4.3, along with our previous data and the theoretical predictions from the thick-wall tube model in Chapter 3.

Before discussing the results of the GM pressure coefficients, the hydrostaticity of the PTM needs to be considered. Water solidifies at 1 GPa and undergoes a further transition at around 2 GPa, and hexane transforms to solid at around 1.4 GPa and there is an evidence of further transition at 9.1 GPa Liu et al. [2006], Kavitha and Narayana [2007]. This can lead to non-hydrostatic pressure conditions, the effect of which might vary from one experiment to another. We record the variation of the full width at half maximum (FWHM) of the ruby R1 line, and find that the width in water stays around 0.59 nm until 8 GPa. In contrast, it starts to increase at 2 GPa in hexane. Here we consider that there is only a small non-hydrostatic effect on the pressure coefficients in hexane because the data after 2 GPa (Figure 4.2 (b)) stays on much the same line as that below 2 GPa. The error bars of pressure should be obtained by measuring the ruby pieces at several different positions. We did not do this in this experiment.

The results are striking, in terms of the followings. First, all the GM pressure coefficients are too high to be within the range of the $thick-wall-tube$ model. Second, at 568 nm in water, the G^+ shift rate of a tube should be a lower than the G^- according to the $thick-wall-tube$ model, whereas the G^+ shift rate of the (6,4) and (6,5) mixture appears to be higher than either of the G^- peaks. Third, the pressure coefficients obtained in hexane are clearly lower than the ones in water, suggesting a strong solvent effect on the GM pressure dependence, which is not expected as the GM shift with pressure is considered to be mostly induced by the decrease of the C-C bond length [Gerber et al., 2009] Ironically, solvent effects on the RBM pressure dependence have not been reported where it might be expected to be strong as the RBM shift with pressure is mostly induced by the decrease of the interlayer distance between the tube wall and the absorbed fluid shell around [Longhurst and Quirke, 2007, Ghandour et al., 2013] Except for these surprises, the results make sense in a higher shift rate of G^- than G^+ for (6, 5) in hexane. And in water the pressure coefficient of G^- from (6, 5) is higher than the one from (6, 4) as expected.

Since the diameter of (6, 5) tubes are very close to the diameter of (9, 1) tubes, the pressure coefficient of which in water from Chapter 3 is also plotted in Figure 4.3, the very different values of these two suggest a strong effect other than diameter. The chirality is the key difference but how it affects the shift

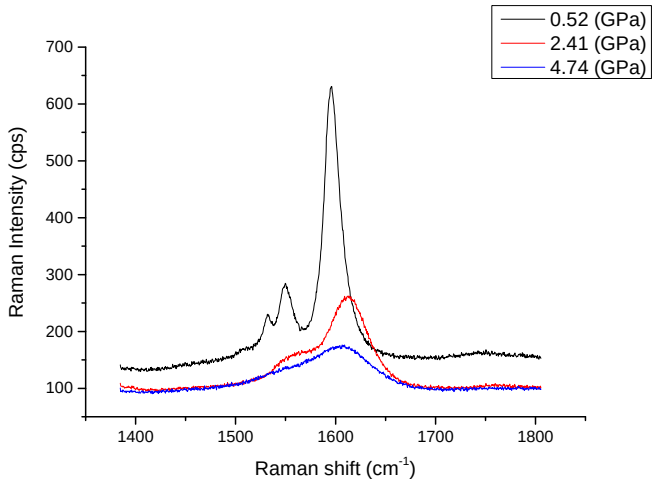

a)

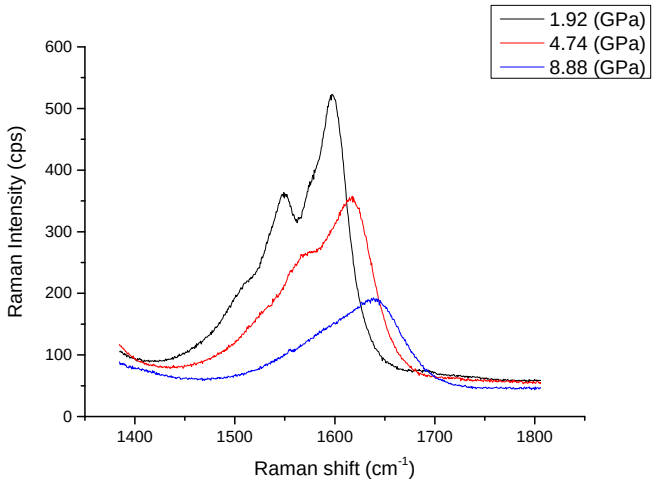

b)

Figure 4.1: "The raw Raman spectra of the GM obtained a) in water with 568 nm laser excitation and b) in hexane with 488 nm laser excitation, under different pressures (labeled) are presented." Adapted from Sun et al. [2014].

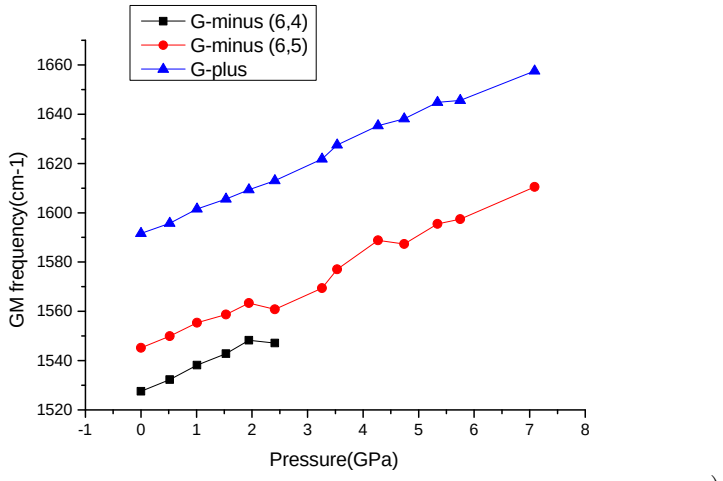

a)

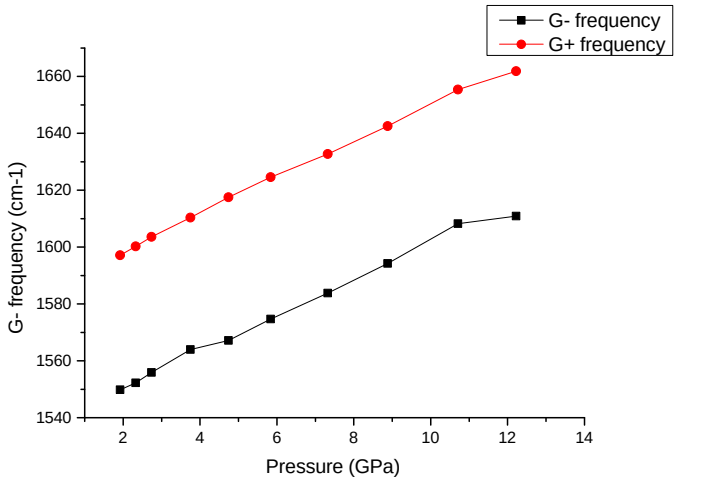

b)

Figure 4.2: "The GM frequencies from the spectra obtained a) in water with 568 nm laser excitation and b) in hexane with 488 nm laser excitation, are plotted against pressure. In a), the blue, red and black points correspond to the G^+ of the mixture, the G^- of (6, 5) tubes and the G^- of (6, 4) tubes. In b), the red and black points correspond to the G^+ and G^- of (6, 5) tubes only." Adapted from Sun et al. [2014].

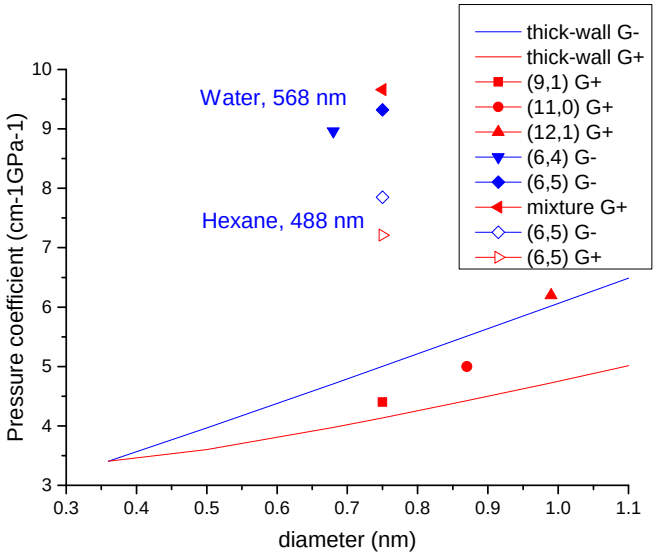

Figure 4.3: The pressure coefficients of carbon nanotubes are plotted against their diameters. The solid lines are for the values predicted by the thick-wall-tube model. The colour red is for the G^+ and the blue is for the G^-. The experimental data is presented as labelled. The data of (9, 1), (11, 0) and (12, 1) tubes are from Ghandour et al. [2013] and the others are from Sun et al. [2014], with the corresponding laser excitation wavelength labelled. Solid symbols are for the data obtained in water and open symbols are for in hexane. The 'mixture G^+' refers to the mixture of (6, 5) and (6, 4) tubes. After Figure 3 of Sun et al. [2014].

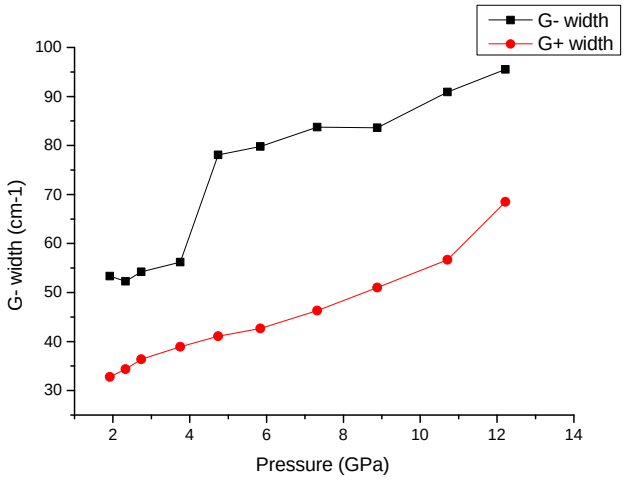

Figure 4.4: "The FWHM of the (6, 5) GM from the spectra obtained in hexane with 488 nm laser excitation is plotted against pressure." Reproduced from Sun et al. [2014].

rates remains unknown at the moment.

With the presence of the G^- peak of tubes of a single diameter in a high pressure experiment, we are able to monitor the change of the tube shape induced by high pressure, by plotting the G^- width against pressure in Figure 4.4. As the G^- is very sensitive to the curvature of the tube wall, it is reasonable to predict a broadened G^- peak in a circular phase (continuous curvature) and a split peak in a collapsed phase (discrete curvature) [Aguiar et al., 2011]. Under the current resolution, the abrupt increase of the G^- width might be interpreted as the splitting and thus implies the collapsing of a tube. The width of G^- peak is now available, as a direct probe of the shape status. However, firm conclusions can only be based on results with a higher resolution and with consideration of bundling effects. In particular, Christofilos et al. [2007] suggested that intertube interaction enhanced the deformation processes, which, as mentioned before, would broaden or split the G^- peak.

In this chapter, we probe the pressure response of (6, 5) and (6, 4) tubes, by using laser of proper energies, which meet the resonance condition of these tubes in a sample of a narrow diameter distribution, to follow their G^+ and G^- under pressure. The striking GM pressure coefficients of (6, 5) and (6, 4) tubes strongly suggest that the shift is not only affected by the diameter and rise a question here — if chirality matters, how it would affect the shift rate. An unexpected clear solvent effect on the GM pressure dependence is also reported, which is contradict to the current understanding. Finally, the broadening of the

G^- might be interpreted as the change of the tube shape, but firm conclusions require better-resolved Raman peaks.

Chapter 5

The Effect of Bundling on the GM Pressure Coefficients of Carbon Nanotubes

This chapter focuses on one of the very important exogenous effects on the GM pressure coefficients — the bundling effect, via Octadecylamine (ODA) functionalized tubes. One key point here is that for the first time we exclude the bundling effect without introducing a new one (from surfactant or functional group).

The study of the GM pressure coefficients is hindered by the availability of carbon nanotubes samples only as bundles or isolated with surfactants. ODA functionalized carbon nanotubes are mostly of a single diameter and can be stably dispersed in 1, 2-dichloroethane (DCE) and chloroform without surfactants. Here we perform high pressure Raman spectroscopy on these tubes and obtain their experimental GM pressure coefficients for individual tubes and bundles. The G^+ pressure coefficient for bundles is only about half of that for individual tubes in DCE and is about two-thirds in chloroform. The G^- pressure coefficient for bundles is about one-third of G^+ in DCE and about the same in chloroform. These results for the first time provide unambiguous experimental evidence of the significant effect of bundling on carbon nanotubes' GM pressure coefficients, identifying it as one of the major reasons for the lack of consensus on what the values are in the literature.

As well as intrinsic effects such as diameter (Chapter 3) and chirality (Chap-

ter 4), the pressure dependence of the GM can be affected by exogenous effects, such as bundling, due to the vdW interaction between the tubes within a bundle. CNTs tend to form bundles [Bandow et al., 1998]. Moreover, bundling effects on the GM pressure coefficient of the tube picked out by RRS may vary with parameters such as the diameters of the surrounding tubes, the bundling configuration (tangled, etc) and the degree of bundling, which is affected by the sample concentration but cannot be precisely controlled.

On the other hand, surfactants stably disperse CNTs, which allows to exclude the bundling effects and their uncertainties, but possibly introduces surfactant effects (vdW interaction between the ambipolar surfactant molecules and CNTs). Researchers compared the GM shift rates of individual tubes to the ones of bundles Christofilos et al. [2007], Lebedkin et al. [2006]. Again, in literature most research on tubes individualised by surfactants were done on samples of mixed diameters and reported varied values of GM pressure coefficients (see Figure 1.7).

Functionalized CNTs provide an alternative approach to study the GM pressure dependence, excluding both the diameter effects and the relatively strong vdW interaction between tubes or between tube and surfactants, and that is the approach we use here, with ODA functionalized tubes. The functional groups are expected to keep the tubes apart in solution and deter bundling, by steric hindrance (see Figure 5.1), while having themselves much less effect on the tubes than surfactant molecules since they are bonded to only one carbon in the order of a hundred. Venkateswaran et al. [2001] first studied the pressure response of ODA functionalized tubes. However, they used ODA tubes in solid (powder) form, which are still bundles (albeit small bundles). No further pressure experiments have been reported on ODA tubes since then. Here we carry out a complete and systematic study, clearly exposing the advantages and disadvantages of using such tubes.

The typical bundle diameter of the solid form of ODA functionalized tubes is 2–8 nm while the length is 0.5–1 μm, which Donovan and Scott [2012] considered to be a very low degree of bundling. They can be stably dispersed in certain organic solvents, such as DCE and chloroform, without the aid of surfactants. In fact, DCE disperses well even non-functionalized SWCNTs after sonication (this can be imaged by STM techniques [Venema et al., 2000]), but the dispersion does not persist long enough for a series of Raman measurements under pressure [Venema et al., 2000]. The steric hindrance caused by the functional group coverage of SWCNTs between 1.8 and 3.2 ODA chains per nanometre stabilizes the suspension [Donovan and Scott, 2013]. It must be noted that as a result of acid treatment during the ODA functionalization, the caps at the end of tubes are removed [Niyogi et al., 2002] and this raises the issue, whether the PTM can

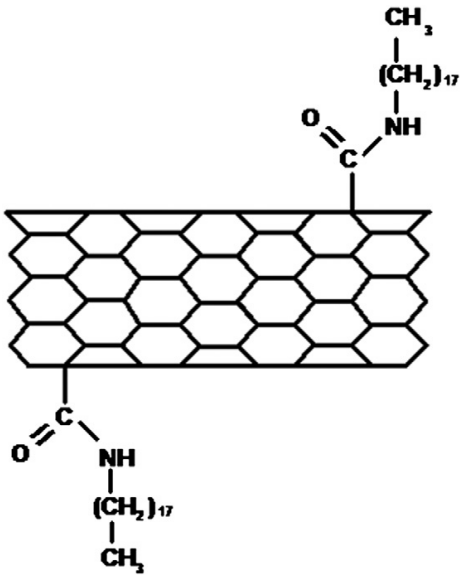

Figure 5.1: A scheme of an ODA functionalized CNT.

enter freely into the tubes. The density of states is largely disrupted [Chen et al., 1998] and therefore no resonance condition applies. This has the advantage that the contribution of CNTs in a given sample to the Raman spectrum is independent of the laser excitation wavelength.

It would be outside the scope of the work reported here to provide a clear answer to what the GM pressure coefficients should be, out of the various values reported in the literature. However, these experiments do present unambiguous experimental evidence, for the significant contribution that bundling alone makes to the pressure coefficients, by comparisons between tubes individualized without surfactants and bundles in DCE and chloroform.

The ODA functionalized tubes were used as purchased from Carbon Solutions, who synthesized them by the arc discharge method, and functionalized them with ODA following a nitric acid treatment [Chen et al., 1998]. The manufacturer specifies that the carbonaceous purity is over 90%, in which SWCNTs loading is 65%±15%, determined by solution-phase near-IR spectroscopy [Itkis et al., 2003]. When first synthesising ODA tubes by this route, Chen et al. [1998] reported a single radial breathing mode (RBM) Raman peak at 170 cm^{-1} in CS_2, at 1064 nm excitation wavelength, indicating that they are of single diameters 1.41 nm, according to the commonly used relation Maultzsch et al. [2005].

$$d = \frac{215}{\omega_{RBM} - 18} \tag{5.1}$$

We prepared four samples of ODA functionalized CNTs — bundled SWCNTs (b-SWCNTs) and individual SWCNTs (i-SWCNTs) in DCE, b-SWCNTs and i-SWCNTs in chloroform, following the recipe (sonication time, power, etc.), which Donovan and Scott [2012, 2013] used in their study. The dispersion was tested by the dichroism [Donovan and Scott, 2012] and viscosity of the solution [Donovan and Scott, 2013], determined by polarizability, thus sensitive to the bundled or individualized status. The concentrations of the samples were 1×10^{-4} wt% for b-SWCNTs in DCE, 1×10^{-6} wt% for i-SWCNTs in DCE, 1.5×10^{-4} wt% for b-SWCNTs in chloroform and 1×10^{-6} wt% for i-SWCNTs in chloroform.

Room temperature non-polarized Raman spectra of the samples were obtained in the backscattering geometry with a Horiba T64000 Raman system with a confocal microscope that had a resolution of 0.6 cm^{-1}, a single 1800 grooves/mm grating and a 100-μm slit, and was equipped with a liquid N_2-cooled CCD detector (Jobin-Yvon Symphony). Suitable edge filters for the 488 nm, 514 nm and 647 nm lines of a Coherent Innova Spectrum 70C Ar^+-Kr^+ laser could be used with the system. We kept the laser power on the sample below 5 mW to avoid significant laser-heating effects on the probed material and the concomitant softening of the Raman peaks.

For the high pressure experiments, we used a MDAC with anvils of 500 μm culet size and very low fluorescence (Type IIa). The ruby luminescence R1 line was used for pressure calibration [Mao et al., 1986]. For the Raman spectroscopy, we used a 20× objective on the b-SWCNTs, i-SWCNTs in DCE and i-SWCNTs in chloroform in the pressure cell and a 40× objective on b-SWCNTs in chloroform. We set the pinhole size in confocal configuration at 200 μm. These settings were found to give the best quality spectra. The four samples were separately loaded into the cells in four separate experiments. After loading the samples into cells with a small pressure applied to prevent the solvent from evaporating, initial RBM and GM spectra of all the samples under 488, 514 and 647 nm excitation were obtained. Then the Raman was measured at higher pressures under 488 nm excitation for b-SWCNTs in DCE and b-SWCNTs in chloroform, and under 514 nm excitation for i-SWCNTs in DCE and i-SWCNTs in chloroform. In all cases, the signal-to-noise ratio of the GM spectra decreased with pressure and therefore this study is in a low pressure range, well below 10 GPa, which is the reported experimental collapse pressure of CNTs of diameters similar to those used here [Caillier et al., 2008].

DCE solidifies at 0.6 GPa [Sabharwal et al., 2007] and chloroform between 0.60–0.79 GPa [Dziubek and Katrusiak, 2008]. To check for non-hydrostatic conditions, we observed the R1 wavelength from two different ruby chips in the cell. Typical values were 694.66 and 694.67 nm at 1.20/1.24 GPa, 694.86

and 694.87 at 1.74/1.76 GPa for b-SWCNTs in chloroform, after observing the solvent solidification. The corresponding errors in pressure are 3.3% and 1.1%, showing acceptable hydrostaticity in this high-pressure study.

Figure 5.2 shows the raw RBM spectra of the dry sample on a glass slide and four prepared samples in cells. The spectra are vertically shifted for clarity to compare the spectra of i-SWCNTs to b-SWCNTs.

Following the literature, we assign the peaks at 268, 302 and 414 cm^{-1} to DCE [Sabharwal et al., 2007] and the peaks at 251 and 368 cm^{-1} to chloroform [Hubel et al., 2006]. For the CNTs, the fitted RBM frequencies (Lorentzian fit) of the dry sample are at 164.9 and 179.5 cm^{-1}, and correspond to tubes of diameters 1.46 and 1.33 nm, according to Eq. 5.1. The ratio of the peaks' integrated area is 9.85:1, former to latter. The small RBM peak cannot be detected for samples loaded into diamond-anvil cells as the absorption by diamonds weakens the signal. For i-SWCNTs which are at an order of magnitude lower concentration than b-SWCNTs, even the main peak is no longer detectable.

Figure 5.3 shows the raw D, G and 2D-band spectra of the dry sample on a glass slide. A clear single G^- peak at 1565.9 cm^{-1} can be observed. The defectiveness of the tubes can be judged by the peak intensity ratio of the G to D-band features I_G/I_D=46.33. This may be compared with the values given by Brown *et al.* for non-functionalized SWCNTs of a diameter distribution vary from about 2 to 30 [Brown et al., 2001]. The low implied defectiveness is not unexpected given that the coverage of the functional groups is between 1.8 and 3.2 ODA chains per nanometre (approximately per 150 carbon atoms). Thus we suppose that the GM and RBM of these tubes are representative of the unperturbed (non-functionalised) tubes.

Before presenting the data, it may be noted that the signal to noise ratio of the Raman spectra presented here is low, for two reasons. Firstly, the Raman experiments are performed under non-resonance conditions as the density of states of these tubes is largely disrupted and thus the peak intensities are up to 6 orders of magnitude lower than those under resonance conditions. Secondly, extremely low samples concentration are used, which is necessary for the stability of the dispersions.

We need to consider the effect of concentration on CNTs GM pressure coefficients, as i-SWCNTs and b-SWCNTs, which we are going to compare, are of different concentration. Figure 5.4 presents the GM spectra obtained in high pressure measurements on b-SWCNTs in chloroform, from two different spots — one in a dark area, which is richer in bundles, making it observable under microscope, and the other in a transparent area, which is less concentrated. We label the GM spectra as concentrated bundles and diluted bundles. The baselines are subtracted, and then the spectra are vertically shifted, proportional

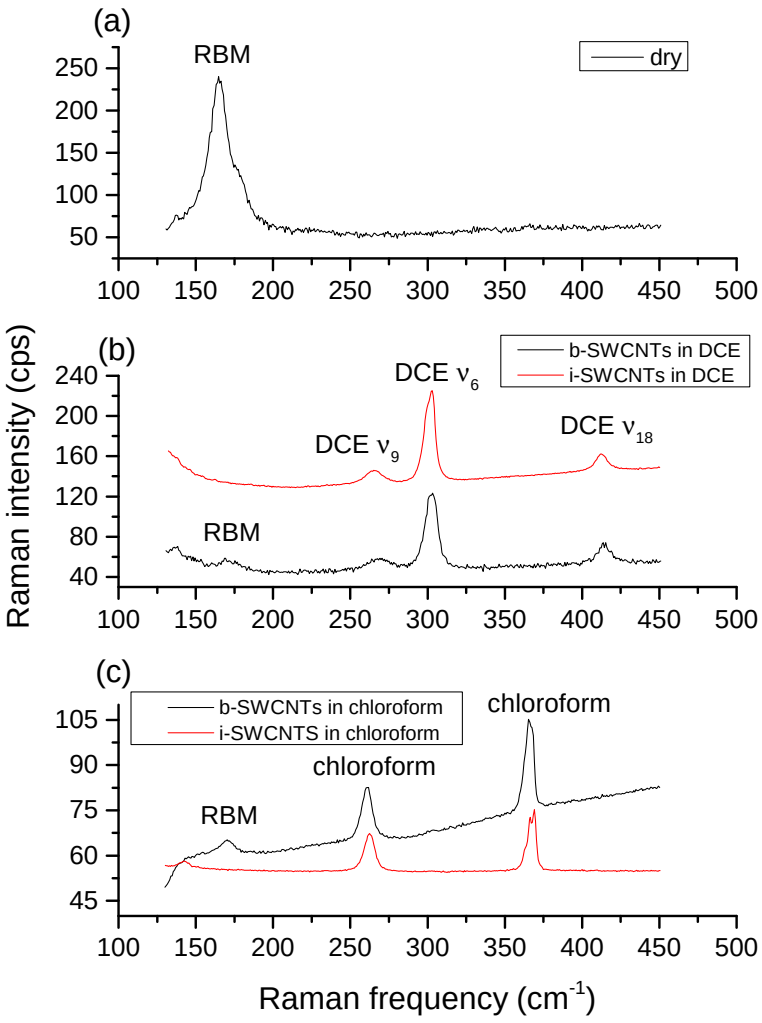

Figure 5.2: The RBM spectra of ODA functionalized tubes are shown for (a) dry samples on a glass slide, (b) b-SWCNTs (black) and i-SWCNTs (red) in DCE and (c) b-SWCNTs (black) and i-SWCNTs (red) in chloroform. In (b) and (c) the spectra are vertically shifted for clarity. The Raman peaks from the solvent are labelled. Laser excitation wavelengths are 488 nm for b-SWCNTs in DCE and b-SWCNTs in chloroform, and 514 nm for i-SWCNTs in DCE and i-SWCNTs in chloroform. Raman shifts do not vary with the excitation wavelength.

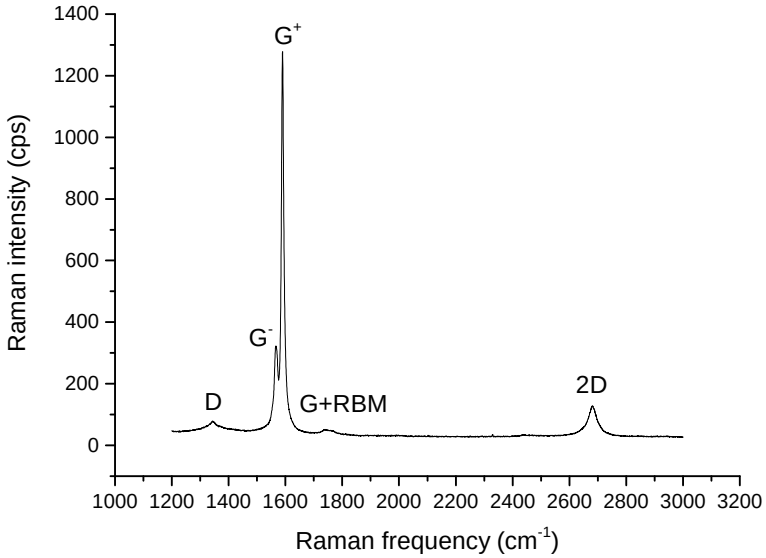

Figure 5.3: The D, G and 2D spectrum of ODA functionalized tubes are shown for dry samples on a glass slide. The laser excitation wavelength is 514 nm.

to pressure. Importantly, figure 5.4 shows that the GM frequencies are nearly unaffected by the sample concentration and therefore it is reasonable to consider that the GM pressure coefficients are independent of the sample concentration in the low pressure range in this study.

Figure 5.5 exhibits the GM spectra of b-SWCNTs and i-SWCNTs at similar pressure points in both DCE and chloroform. For b-SWCNTs in chloroform, the spectra are those of concentrated bundles in Figure 5.4. For i-SWCNTs in DCE and chloroform, the Raman intensities are multiplied by a factor 200, in order to get clear comparisons to the b-SWCNTs. As a result, the i-SWCNTs spectra show an increased level of noise compared to b-SWCNTs spectra. The baselines are subtracted, and then the spectra are shifted vertically, proportional to pressure. The narrow peak at 1554.4 cm^{-1} in the GM spectrum of i-SWCNTs in DCE is assigned to an oxygen vibrational Raman peak from the air between the microscope and the cell Fletcher and Rayside [1974]. It is on top of a wide peak, which might be from carbonaceous impurities in the samples. The GM peak is right next to the wide peak and the signal to noise ratio is low. The ratio looks rather lower in the presented spectra than it is due to the wide range of the y-axes in Figure 5.5 (a) and (b). The y-axis zoomed-in spectra of b-SWCNTs in DCE at 2.44 GPa, i-SWCNTs in DCE at 2.12 GPa, b-SWCNTs in chloroform at 2.28 GPa and i-SWCNTs in chloroform at 1.20 GPa are shown

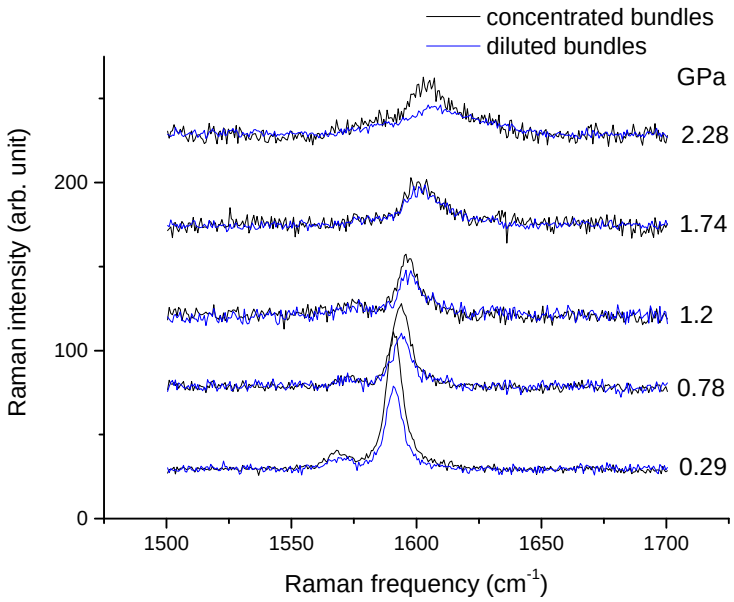

Figure 5.4: GM spectra of b-SWCNTs in chloroform are collected from the dark area (black) and the transparent area (blue). The spectra are vertically shifted, proportional to pressure. The pressures, under which the spectra are obtained, are labelled. The laser excitation wavelength is 488 nm.

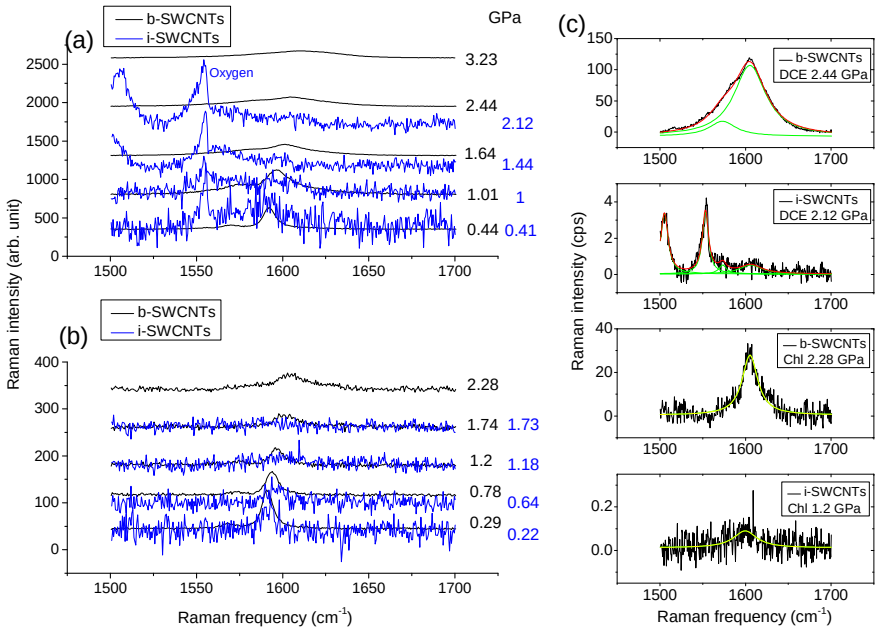

Figure 5.5: The GM spectra of i-SWCNTs (blue) and concentrated b-SWCNTs (black) are shown in (a) DCE and (b) chloroform. For i-SWCNTs the Raman intensities are multiplied by 200. The spectra are vertically shifted, proportional to pressure. The pressures, under which the spectra are obtained, are labelled in the colours corresponding b-SWCNTs (black) or i-SWCNTs (blue). The oxygen vibrational Raman peaks are labelled. The laser excitation wavelength is 488 nm for b-SWCNTs in DCE and b-SWCNTs in chloroform, and 514 nm for i-SWCNTs in DCE and i-SWCNTs in chloroform. Raman shifts do not vary with the excitation wavelength. In (c), four labelled spectra and the Lorentzian fits are shown as examples as they are of the lowest signal to noise ratio among the spectra which will be used to extract the GM pressure coefficients for each samples.

in Figure 5.5 (c). These four spectra are selected as examples because they are of the lowest signal to noise ratio among the spectra which we will use to obtain the GM pressure coefficients for each samples. Remarkably, the GM intensities of i-SWCNTs are extremely low – about 0.5 cps in DCE (400 s to collect and accumulated twice) and 0.1 cps in chloroform (900 s to collect and accumulated twice). The Lorentzian fits for the four spectra are shown in yellow lines and the details of the fitting will be discussed in the following part.

We fit the GM spectra of i-SWCNTs in DCE and chloroform in Figure 5.5 each with a single Lorentzian and the GM spectra of b-SWCNTs in DCE and chloroform in Figure 5.5 each with two Lorentzians (except b-SWCNTs in chloroform at 2.28 GPa). In the latter case these correspond to the G^+ and G^- peaks, which are initially well separated but cannot be told apart with increased

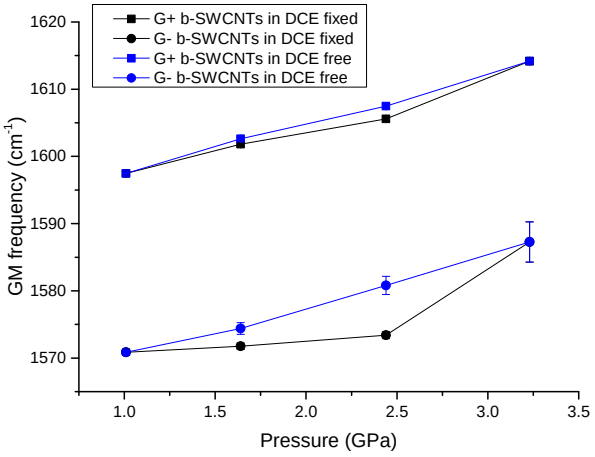

Figure 5.6: The GM frequencies of b-SWCNTs in DCE are plotted against pressure. The frequencies are obtained by fixing the integrated area ratio of G^+ to G^- at the free fitting value at 0.44 GPa (black), and by releasing all the fitting parameters of the two Lorentzians (blue). The squares are for G^+ and the circles are for G^-. Where they exceed the size of the data-points, error bars are shown.

pressure. We fix the integrated area ratio of G^+ to G^- at the value obtained by free fitting at the first pressure point (0.44 GPa) during the whole fitting, to avoid unphysical fitting results such as a larger G^- than G^+ peak, that may be obtained when releasing all the fitting parameters of the two Lorentzians. Figure 5.6 shows how these two fitting procedures lead to different GM frequencies of b-SWCNTs in DCE. The difference is mainly at the uncertain frequencies of the weak G^- peak. We plot GM frequencies, obtained by fixing the integrated area ratio, of all the samples against pressure with error bars in Figure 5.7. Linear least square fits are shown, excluding the points of b-SWCNTs in DCE at 3.23 GPa, for the similar pressure range to that of i-SWCNTs in the same solvent and the point of i-SWCNTs in DCE at 0.63 GPa as an abnormal point, which is exactly at the DCE solidification point. The excluded data points are labelled green.

The reliability of the obtained GM frequencies can be seen from Figure 5.5 (c). It can be further validated by Figure 5.8, where we plot the GM width of all the samples against pressure. We expect the GM width to evolve systematically with pressure and therefore an absurd value of the GM width might indicate that the corresponding GM frequency is questionable. The points in Figure 5.8 are all of reasonable values while the second point of i-SWCNTs in DCE is excluded in the extraction of the GM pressure coefficient as being exactly at

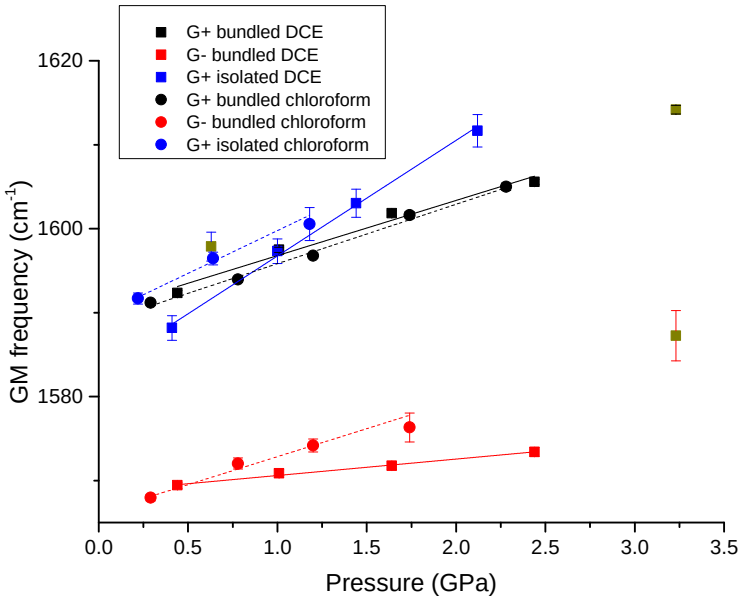

Figure 5.7: The GM frequencies of all the samples are plotted against pressure. The colour black is for G^+ frequencies of b-SWCNTs, red is for G^- of b-SWCNTs and blue is for G^+ of i-SWCNTs. The squares are for samples in DCE and the circles are for chloroform. Error bars are shown, where they exceed the size of the points. The linear fits are presented as solid lines for DCE and dashed lines for chloroform. The fits exclude the points for b-SWCNTs in DCE at 3.23 GPa and i-SWCNTs in DCE at 0.63 GPa, which are shown as open symbols.

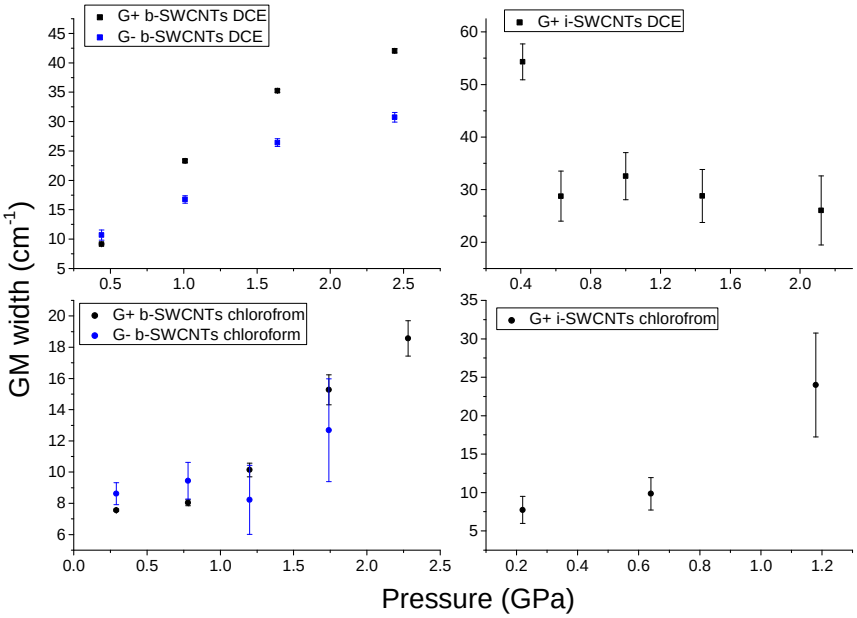

Figure 5.8: The GM width of all the samples are plotted against pressure. The colour black is for G^+ and blue is for G^-. The squares are for samples in DCE and the circles are for chloroform. Error bars are shown, where they exceed the size of the points.

Table 5.1: The GM pressure coefficients for all measured samples

GM pressure coefficients ($cm^{-1}GPa^{-1}$)	G^+	G^-
b-SWCNTs in DCE	6.6±0.7	2.0±0.1
i-SWCNTs in DCE	13.8±0.6	
b-SWCNTs in chloroform	7.1±0.3	6.7±0.7
i-SWCNTs in chloroform	10.2±1.3	

the DCE solidification point.

We present the GM pressure coefficients in Table 5.1 from the linear fit in Figure 5.7. The errors are from the linear fit, the Lorentzian fit for the peak position and the system resolution.

Figure 5.7 and Table 5.1 present the key results that the G^+ pressure coefficient for bundles is only about half of that for individual CNTs in DCE and is about two-thirds in chloroform. For bundles, the G^- pressure coefficient is about one-third of G^+ in DCE and about the same in chloroform.

At the moment we do not fully understand these results. There are four key issues. First, the pressure dependence of the GM is commonly considered as determined by the shortening of sp^2 bond, which should have little to do with the environment, in contrast with the apparent bundling and solvent effects

reported here. This is quite unlike the pressure dependence of the RBM, which is due to the decrease of the distance between tube shell and the absorbed fluid layer and therefore unsurprisingly sensitive to the environment [Longhurst and Quirke, 2007]. Second, according to the *thick-wall tube model* [Ghandour et al., 2013], the G^+ and G^- pressure coefficients of 1.46 nm tubes should be 6.0 and 8.0 $cm^{-1}GPa^{-1}$ respectively. The model is based on individual tubes but the G^+ values of i-SWCNTs are much higher than the predicted ones. The G^+ values of b-SWCNTs agree well, as the previous work on bundles [Ghandour et al., 2013]. Third, the tangential stress is always larger than the axial stress for a tube under hydrostatic pressure. The pressure coefficient of the vibrational mode along tube circumference (G^-) should therefore be always larger than the one along tube axis (G^+). This is again against our observations in DCE. And fourth, considering that the end of the tubes has been removed, the solvents might be expected to enter inside the tubes. If the internal pressure (pressure of the solvent inside the tube) is at a value between 0 and the external pressure, the pressure coefficients for both G^+ and G^- should lie between the graphene value and the *thick-wall-tube* model predictions. Results of i-SWCNTs in Table 5.1 are out of this range. The normal way to judge whether tubes are solvent-filled by the shift of RBM frequency [Cambré et al., 2010] is not possible in this case, because no close-ended ODA functionalized CNTs are available for comparison (the caps are removed during the ODA functionalisation).

ODA functionalized CNTs, as samples to study the CNTs GM pressure coefficients, have the following advantages. First, given that they are mostly of a single diameter and their density of states is largely disrupted, the contributions to the RBM and GM signals from tubes of different diameters may be taken proportional to their contents in samples, regardless of the laser excitation. In Figure 5.2, we obtained the RBM integrated area ratio of 1.46 nm to 1.33 nm tubes at 9.85 to 1. The G^+ signal is contributed by 1.46 and 1.33 nm tubes, and in the absence of resonance, also with a ratio of 9.85 to 1. It is reasonable to attribute the GM pressure coefficients in Table 5.1 to 1.46 nm tubes only. Second, the ODA side chains offer the steric hindrance and therefore provide us with SWCNTs samples stably dispersed without the aid of surfactants. This is the main reason we use ODA CNTs in this study.

There are related disadvantages, namely the limited choices of PTM consistence with dispersion and the potential side chain effect on GM pressure coefficients. DCE and chloroform are effective in dispersing CNTs samples but are not considered as good PTMs because of their low solidification pressures.

In order to exclude the inter-tube or tube-surfactant van der Waals interaction, we introduce the side chains. The ODA coverage between 1.8 and 3.2 chains per 150 carbon atoms may be high from the point of view of chemistry,

but it is too low to have an effect on the in-plane vibrational frequencies at ambient pressure, and there is no reason to suppose it should have any more effect at high pressure. The upshift of GM frequency with pressure is induced by the increasing overlap of electrons of carbon atoms. In the case of bundles or surfactants, each carbon atom is under the influence and the behaviour of its electrons are affected, as shown in this work, while in the case of ODA tubes, electrons of most carbon atoms are not affected by the sp^3 defects (1.8–3.2 sp^3s in 150 sp^2s). Thus its effect on the pressure coefficient should be small, certainly not comparable to the effects of bundles or surfactants. Therefore, the experimental data of ODA functionalized tubes presented here can be meaningfully compared to the theories of the in-plane bond response to pressure in pristine SWCNTs.

In conclusion, we present the experimental demonstration of the significant and unexpected bundling effects on the CNTs GM pressure coefficients of a specific chirality. The G^+ pressure coefficient for bundles is only about half of that for individual CNTs in DCE and is about two-thirds in chloroform. For bundles, the G^- pressure coefficient is about one-third of the G^+ in DCE and about the same in chloroform. Such comparison for the first time excludes the effect of surfactants, achieved by using ODA functionalized tubes. The origin of the bundling and solvent effects on GM pressure coefficients is unclear at the moment and the values of the pressure coefficients in this work are beyond the framework of the current understanding, especially the *thick-wall tube model*. Despite posing unresolved questions, this work clarifies that the bundling effect, is one of the major reasons for the current lack of consensus on the value of the GM pressure coefficients.

Chapter 6

The Collapse of Carbon Nanotubes

In this chapter, we consider the collapse of closed tubes at high pressure. The collapse under external pressure of a long tube is a classic problem, for which with R_0 the outer radius, E Young modulus, ν Poisson ratio and h wall thickness, there are analytic solutions for both thin-walled (after the second equal sign) and thick-walled tubes (after the first equal sign),

$$P_C = 2\frac{E}{1-\nu^2}\frac{h^3}{R_0(R_0-h)^2} = 2\frac{Mh^3}{R^3} \tag{6.1}$$

where M is the plane strain modulus and the expression in M is for a thin wall, $h \ll R$ [Corradi et al., 2011]. It is appropriate to use the thin-walled approximation for nanotubes, with R being the radius at the nuclear positions, although the wall thickness of 0.34 nm is not small compared with the diameter.

Figure 6.1 illustrates the argument. The circle is discretised to a regular polygon with hinges at the corners and with rigid sides which are impermeable to the pressure-transmitting medium (PTM). This is progressively modified in Figure 6.1 (a) to (e) without changing the appropriate value of R. The diagram Figure 6.1 (e) is thus a model for the nanotubes, with the weak material which defines a wall thickness representing the π-orbitals. So the conclusion is that any of these models in Figure 6.1 are to be compared with the thin-wall analytic equation rather than the thick-walled.

We recognise the term Mh^3 in Eq. 6.1 as twelve times the bending stiffness of the wall of the thin-wall tube. We use an atomic model with discretised bending stiffness k_0 (angular springs) at each atom, and for a spacing of a_0 the stiffness of a chain of such atoms is $k = a_0 k_0$. Then the collapse pressure of a

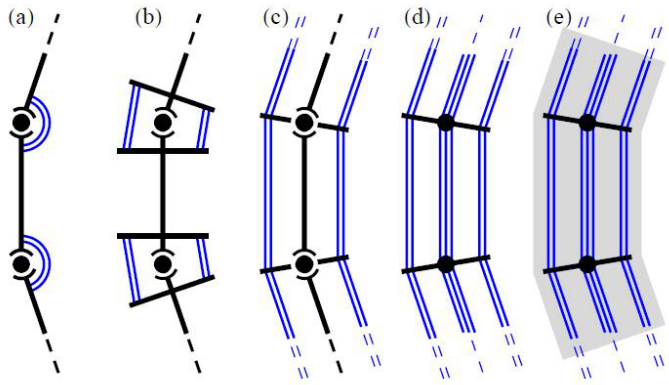

Figure 6.1: "In (a), a thin-wall tube is discretised with hinges and angular springs. In (b) the angular springs are replaced by levers and linear springs permeable to the PTM, and in (c) the linear springs extend the full length of the sides. In (d) the rigid sides are themselves made into springs (impermeable to the PTM) and in (e) a weak material is added to give a real wall-thickness." Reproduced from Sun et al. [2013].

ring of N such atoms is

$$P_C = \frac{24k}{d^3} = \frac{24\pi^3 k_0}{N^3 a_0^2} \tag{6.2}$$

where d is the diameter of the ring.

Numerical data for the collapse pressure of such rings is shown in Figure 6.2 (a). Results of DFT - Monte Carlo calculations are shown in Figure 6.2 (b) for nanotubes where the interaction between carbon atoms was described with the potentials introduced in Holec et al. [2010]. Periodic boundary conditions were used along the axis of the tube and the length of the tube was held constant. When the pressure is increased, first, the nanotube only changes its radius, but preserves its shape. After a critical pressure is exceeded, at 3.2 GPa in Figure 6.2 (b), the nanotube shows a transition from a circular to elliptic cross section. This is accompanied by a much faster change in radius with pressure. In the final stage the structure bulges inwards. Both models, Hooke's law atomic model as well as the Monte Carlo simulation, predict a well defined collapse pressure. Furthermore, the larger the nanotubes the closer they follow the predictions from continuum tube models.

Finally, it should be pointed out that the collapse pressure is hard to relate to experiment; the collapse is clearly a continuous process but completes over a narrow pressure range perhaps difficult to resolve in experiment.

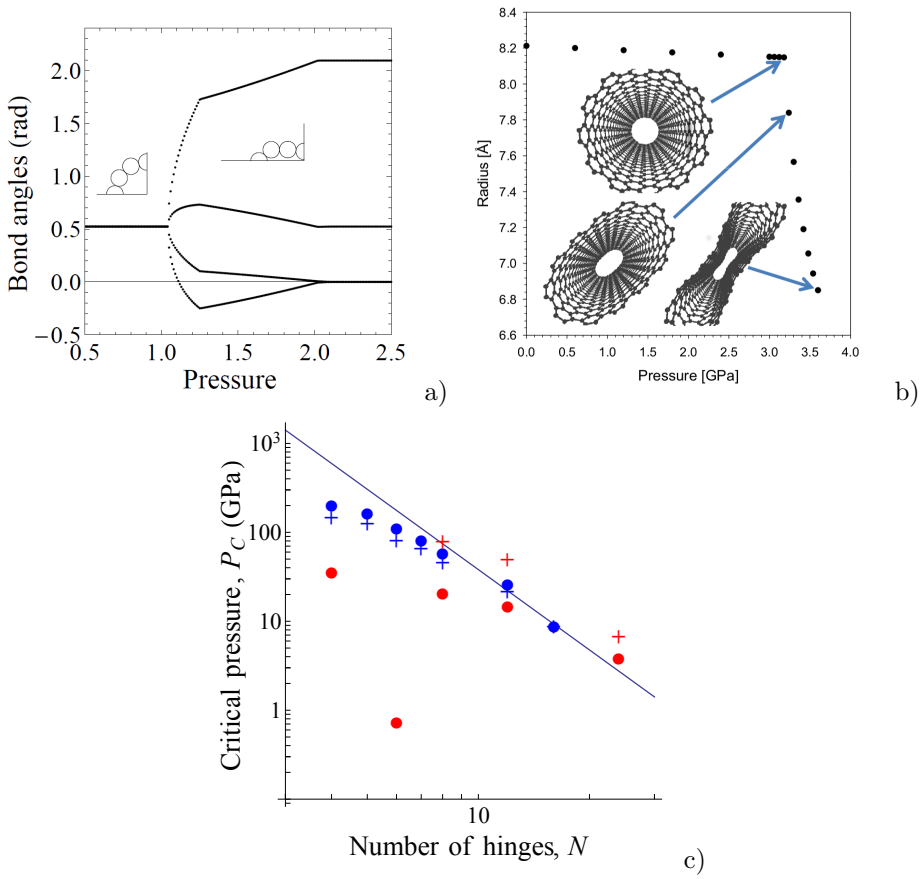

Figure 6.2: "Models of nanotubes under pressure are shown in (a), the Hookes Law atomic model, and (b) Monte Carlo simulations of the change of radius of the shown nanotube as a function of the applied pressure. In (c) the initial () and final (+) collapse pressures from Hooke's Law atomic model (blue) and Monte Carlo simulations (red) are plotted in against the size of the tubes. The theoretical line for the thin-wall continuum tube is shown for comparison." Adapted from Sun et al. [2013].

Chapter 7

Conclusions and further work

7.1 Summary

This thesis reviews the research on carbon nanotubes under pressure as my PhD project.

Researchers recorded the Raman spectra of carbon nanotubes under pressures and obtained the GM pressure coefficients. The discrepancy of the results, obviously, is because some of the many variables which matter in a high pressure experiment on carbon nanotubes change in different measurements. The questions to answer, naturally, are which of the variables matter and how they affect the GM pressure coefficients.

The diameter of tubes should matter. Via Raman spectroscopy equipped with a wavelength-tunable laser we obtain the GM pressure coefficients of tubes of specific diameters and explain the experimental diameter effect well with a thick-wall tube model and revised Grüneisen parameter and shear deformation potential.

The chirality of tubes should not matter. Unexpectedly, we report a significant chirality effect by a comparison between the GM pressure efficients of (6, 5) and (9, 1) tubes, which have very similar diameters.

Apart from intrinsic effects, bundling might also matter. In most literature, unbundling is accompanied by surfactant. If bundling affects the GM pressure coefficients, very likely for the vdW between tubes, so does the surfactant, for a similar reason — interactions between tubes and large surfactant molecules. Using ODA tubes, we compare the bundled and individual tubes excluding the surfactant and report a very strong bundling effect.

We do not understand the chirality and bundling effects, but we have suspicions, that it is related to the π-electrons behaviour. Opposite to experiments, a theoretical work introduce the variables one by one. A natural start point is graphene and graphite, without the complexity of the wall curvature. We introduce a new parameter relating the out-of-plane strain to in-plane phonon frequency, which very likely reflects the effect of π-electron behaviour.

Finally, we find that a thin-wall model and atomistic-refined elastic ring model are fairly good approximation in predicting the critical pressure for carbon nanotubes, through comparison with the results from MD.

7.2 Further work

For the theoretical work, frequencies of graphite in-plane modes have already been calculated under uniaxial strain (in-plane geometry fixed) and stress (released) along c-axis (see Chapter 2). I will then do the calculation for bi-layer graphene changing interlayer distance, to quantify the amount of -electrons squeezed through sp2 network and its contribution to G-mode frequency. Following this I will displace the upper layer in tri-layer graphene along c-axis, to apply pressure to the lower two, which are fixed still, to calculate the amount of -electrons squeezed through the middle layer and pressure transmitted to the lower layer. This quantifies the capability of -electrons acting as pressure transmitting media (PTM) and its contribution to the G-mode shift of the lower layer. The next part concerns interactions of fundamental importance to the applications of graphene to batteries, electronics, etc. I plan to insert solvent molecules (e.g. water) in between the graphene layers, to quantify solvent effects on G-mode frequencies and their response to pressure. This will lead to a better understanding of the role PTM (and any substrate) play in the -electron behaviour. Finally I plan to calculate G-mode frequency under strain for carbon nanotubes of specific chiralities, which is related to the following part.

From the experimental side, my approach is to establish sufficient experimental data for tubes of specific chiralities — most existing data are from tubes of mixed chiralities, then attempt to empirically quantify the chirality effect by chiral angles or pyramidaliztion or -orbital misalignment angle, and finally interpret the effect with -electron behaviour, combing the results obtained for graphene. To achieve the goal, I will firstly run a laser excitation wavelength scan to obtain Kataura plot under ambient and high pressure. Then I will focus on tubes of a specific chirality and obtain a 3D plot of pressure vs. excitation wavelength vs. Raman GM intensity. The above will be repeated in DWCNTs, the results of which will be compared to tri-layer graphene, which originally mimics DWCNTs under pressure. I will use various PTM to quantify

the solvent effect, and compare with the results for graphene.

Chapter 8

Appendices

8.1 Raman Spectroscopy Under High Pressure

Raman scattering is inelastic. Stokes scattering refers to the process that incident photon excites atom or molecule from its ground state to a virtual energy level and as it drops to an excited vibrational state, the emitted photon has lower energy than the incident photon. Anti-Stokes refers to the process that has a vibrational state as start and a ground state as end. We detect scattered photon, the energy difference between which and the incident photon is the energy of the corresponding vibrational mode. We typically use wavelength to describe the energy of the photons and naturally the energy of a vibrational state is in wavenumbers, as

$$\Delta\omega = (\frac{1}{\lambda_0} - \frac{1}{\lambda_1}) \tag{8.1}$$

where λ_0 is for the incident photon and λ_1 is for the scattered.

Raman signals are very weak. One in 10^{12} excitation photon is Raman-shifted and one in 10^3 passes optical filters. A further signal loss of 99 % is expected if a triple spectrometer is used. Some vibrational modes are Raman-inactive, if there is no change in the polarisability. However, RRS is able to increase the intensity by up to 10^5 if the virtual energy level happens to match a real state. The momentum of a phonon is usually three orders of magnitude smaller than the π/a of a Brillouin zone, so Raman spectroscopy gives information only at the Γ-point.

High pressure is generated in a DAC. The Raman signal is further reduce to 1/1000 because of the absorption of the diamond. Diamond is stiff and the culet size is small to generate high pressure, up to 100 GPa. A thin gasket makes the cell more stable than a thick one, so the pre-indentation of the gasket is

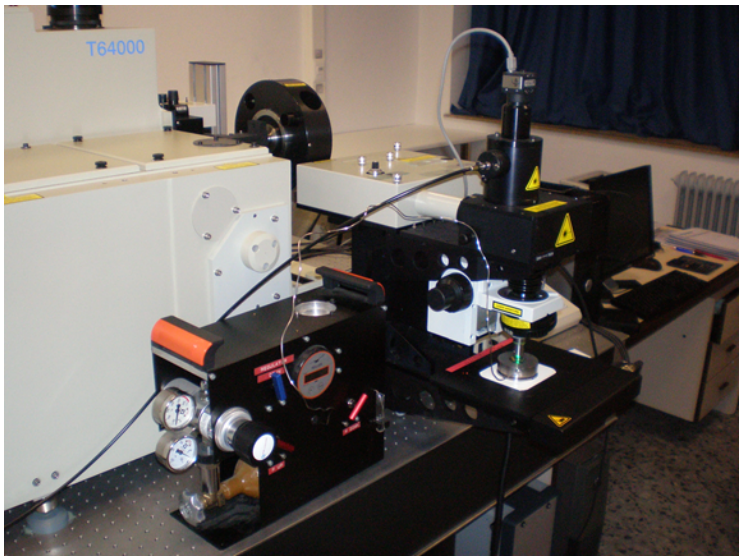

Figure 8.1: A photo of all apparatus, including the spectrometer and the DAC (Taken by Prof J. Gonzalez).

desirable. When decreasing pressure, we expect the sample hole to be enlarged to reduce the pressure in the cell. However, the pressure in the fluid is not sufficient to extrude the gasket outwards and the pressure will be reduced by leaking, as no seal is provided between the anvil and gasket. The data collected during decreasing is not so reliable as that during increasing.

A photo of all apparatus is shown in Figure 8.1 (The author thanks Prof J. Gonzalez for providing this photo.). More details can be found below.

HiPco: The details of the HiPco SWCNTs are available at `http://www.nanointegris.com/en/hipco`. Overall, they contain tubes of a wide diameter distribution and are commonly used in research.

Debundling: CNTs tend to form bundles and sonication can break bundles. Sonication with a probe is more efficient in debundling than sonication bath as the power is directly applied to the bundles. In general, the sonication power and time should be set high and long enough to break the bundles but not too high and long to destroy the tubes. The concentration of the samples should be low to prevent rapid re-bundling after the sonication. Two methods to significantly extend the duration of the debundled status are to add surfactant in solvents or use ODA functionalised tubes.

Triple spectrometer: Three monochromators are connected in series. The diagram of a Czerny-Turner monochromator is shown in Figure 8.2 (source: `www.gnu.org/copyleft/fdl.html`). B and F are slits, C and E are curved mirrors to collimate/refocus the light, and D is either a grating or a prism, to

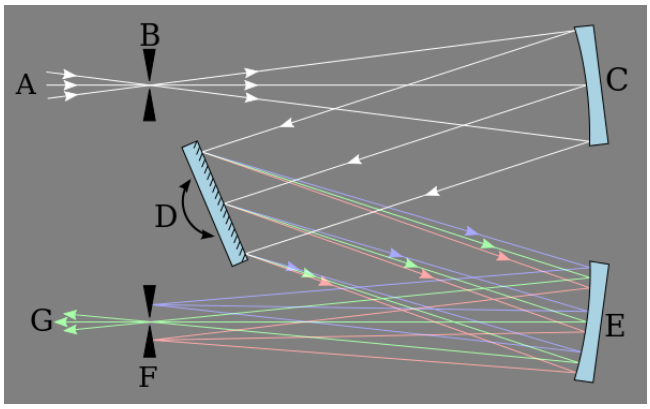

Figure 8.2: A diagram of a Czerny-Turner monochromator (source: `www.gnu.org/copyleft/fdl.html`)

disperse the light on the slit F. The angle of D can be tuned to make the lights of a specific wavelength pass through. A triple spectrometer is suitable with a multi-wavelength laser or a wavelength tuneable laser, while the disadvantage is the huge loss of the signal during the reflections/diffractions.

Edge/colour filter: An Edge/colour filter allows near 100% transmission above a certain wavelength and near zero transmission below a certain wavelength. The edge steepness (the difference between the above two wavelengths) is usually below 10 nm for an edge filter and can be more than 50 nm for a colour filter. Both filters are suitable with laser of a specific wavelength. The advantage of them is the low signal loss compared to the use of a triple spectrometer. Colour filters are very cheap, which provides a way to avoid huge signal loss in the experiments with multi/tuneable-wavelength laser, by having many colour filters for different wavelengths, and using the one corresponding to a specific laser wavelength, if we do not study low wavenumber modes.

Horiba T64000 Raman System: The details are available at `http://www.horiba.com/fileadmin/uploads/Scientific/Documents/Raman/T64000.pdf`. The advantage is the flexibility that it can switch between the triple and single (employing the edge/colour filter) configuration to suit the specific study. A schematic of subtractive foremonochromator and spectrograph configuration is shown in Figure 8.3 (The author thanks Prof J. Gonzalez for providing this schematic.).

DAC: A diagram of the standard DAC and the Zen configuration are shown in Figure 8.4 [Dunstan, 1989]. The Zen configuration provides a good control of pressure due to the large contact area between the single diamond and the gasket. The pressure can be applied by screws or a hydraulic ram to these cells. The pressure is applied by inflating the membrane to a MDAC, which

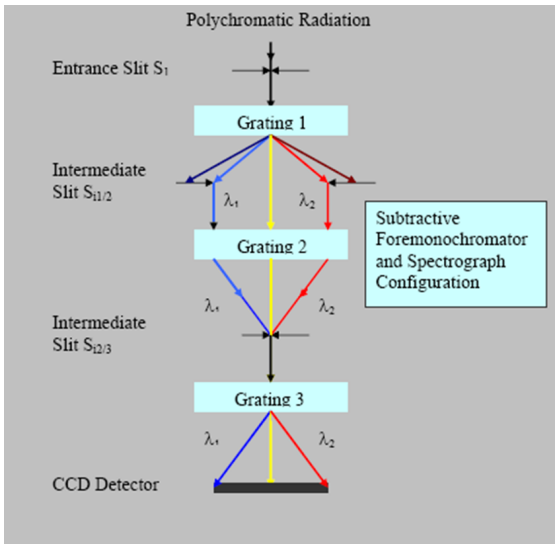

Figure 8.3: A schematic of subtractive foremonochromator and spectrograph configuration (provided by Prof J. Gonzalez).

provides a good control of pressure and a much wider pressure range than the Zen configuration.

The experimental procedures: 1) We need to align the diamonds in the diamond anvil cells to avoid diamond breakage. We first do the tilt alignment by looking at the number of coloured fringes – two fringes indicate a good tilt alignment. We then perform the axial alignment, simply making the culets of the two diamonds overlap. 2) We pre-indent the gasket to the thickness of 70 μm. For the standard DAC, we need to pre-indent the gasket gently and gradually, by applying a bit pressure, taking the gasket out of the cell, checking the thickness, loading it back to the cell and repeating all the above until the thickness reaches 70 μm . For MDAC, because the pressure of the inflated gas can be precisely controlled (i.e. the force on the gasket is precisely controlled), we can directly pre-indent the gasket to 70 μm. 3) We drill a hole at the centre of the indent (we use a driller but the spark drilling is desired if the pressure measurement goes above 10 GPa.) and then clean the gasket in sonication bath. 4) We load samples into the hole of the gasket after fixing the gasket on the bottom diamond. For bundled CNTs in solvent, we use a needle to tip some tubes powders into the hole, load a drop of solvent into the hole and close the cell by the top diamond with ruby pieces stick to its culet – I personally like this way, as often the ruby flows out after loading the liquid drop if we load the ruby first. For ODA tubes, we load a drop of samples into the hole and need to close the cell very fast and apply an initial pressure at several kbar to prevent the evaporating of DCE and chlorofrom. 5) We use a silicon piece to calibrate the

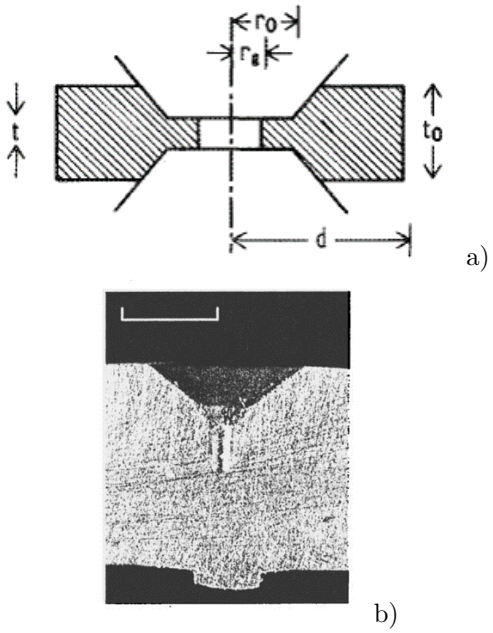

Figure 8.4: Diagrams of a standard diamond anvil cell and the Zen configuration [Dunstan, 1989].

Raman system and then we record the spectrum of a ruby piece on a glass slide as a pressure reference. 6) We put the cell under the microscope subjected to the Raman spectrometer and focus on the ruby piece and record its spectrum. 7) We focus on the samples and record their spectra. A test Raman spectrum of bundled CNTs in cell usually takes less than three minutes to record. We focus on different areas and at different depth in the cell to get the best signal of the sample – a trick I use here is that after I focus on the surface of the sample, I tune the focus a bit into the bulk (make full use of the cone) to get a better signal. After selecting a certain point, we increase the collecting time to 15 – 20 minutes to improve the quality of the spectrum and accumulate it twice to further reduce the noise. 8) We circulate the collection of the ruby spectrum as a monitor when we increase pressure. We stop slightly before the aimed pressure and wait 10 minutes till the ruby lines (i.e. the pressure inside the cell) get stable. We repeat 6) and 7), to continue the measurements under pressure. Above are the general procedures of an experiment.

8.2 Density Functional Theory

To solve the Schrödinger equation is extremely difficult in most cases. We apply the Born-Oppenheimer Approximation and the Kohn-Sham scheme to make the

Hamiltonian $H = -\frac{\hbar^2}{2m}\nabla^2 + V_{e-e}^{non-int.}[\rho] + V_{e-n}[\rho] + V_{xc}[\rho]$, where e is electron, $non-int.$ is non-interacting, n is nuclei and xc is exchange. We do not know what $V_{xc}[\rho]$ is. LDA assumes that electrons are evenly spread in space and therefore contribution to E_{xc} only relies on $\rho(r)$. GGA additionally uses the gradient of ρ.

In crystals, we have periodic potential and therefore density. Bloch's theorem gives the wavefunction $\psi(\mathbf{r}+\mathbf{L}) = e^{i\mathbf{k}(\mathbf{r}+\mathbf{L})}u(\mathbf{r}+\mathbf{L}) = e^{i\mathbf{k}\mathbf{L}}\psi(\mathbf{r})$, where L is a lattice vector. Instead of integrating all $\mathbf{k}$, we sum up enough $\mathbf{k}$-points to get accurate results. $u(\mathbf{r})$ is periodic and therefore can be expanded in plane-waves and we set a cut-off energy to include all the plane-waves with less energies and get enough accurate results. Also, we replace the near-nuclei Coulomb potential with a weaker pseudopotential.

Perturbation of ionic positions gives phonons. To solve the dispersion relation is difficult if the system is complex — two atoms per unit cell beyond 1D is complex. We use the finite-displacement method — we displace an ion by small distance and calculate the force and its derivative to the displacement on every ion and repeat for each ion, to obtain the dynamical matrix, the eigenvalues of which are the frequencies.

I acknowledge the CASTEP 2014 training workshop in University of Oxford for clear, detailed and systematic demonstrations.

Bibliography

D. Abbasi-Perez, J. M. Menendez, J. M. Recio, A. Otero de-la Roza, E. del Corro, M. Taravillo, V. G. Baonza, and M. Marques. Modeling graphite under stress: Equations of state, vibrational modes, and interlayer friction. *Phys. Rev. B*, 90:054105, 2014.

A. L. Aguiar, E. B. Barros, R. B. Capaz, A. G. Souza Filho, P. T. C. Freire, J. Mendes Filho, D. Machon, Ch. Caillier, Y. A. Kim, H. Muramatsu, M. Endo, and A. San-Miguel. Pressure-induced collapse in double-walled carbon nanotubes: Chemical and mechanical screening effects. *J. Phys. Chem. C*, 115:53785384, 2011.

A. L. Aguiar, R. B. Capaz, A. G. Souza Filho, and A. San-Miguel. Structural and phonon properties of bundled single- and double-wall carbon nanotubes under pressure. *J. Phys. Chem. C*, 116:22637–22645, 2012.

P. T. Araujo, A. Jorio, M. S. Dresselhaus, K. Sato, and R. Saito. Diameter dependence of the dielectric constant for the excitonic transition energy of single-wall carbon nanotubes. *Phys. Rev. Lett.*, 103:146802, 2009.

P. T. Araujo, P. B. C. Pesce, M. S. Dresselhaus, K. Sato, R. Saito, and A. Jorio. Resonance Raman spectroscopy of the radial breathing modes in carbon nanotubes. *Physica E*, 42:12511261, 2010.

S. Bandow, S. Asaka, Y. Saito, A. M. Rao, L. Grigorian, E. Richter, and P. C. Eklund. Effect of the growth temperature on the diameter distribution and chirality of single-wall carbon nanotubes. *Phys. Rev. Lett.*, 80:3779, 1998.

A. Bosak and M. Krisch. Elasticity of single-crystalline graphite: Inelastic x-ray scattering study. *Phys. Rev. B*, 75:153408, 2007.

S. D. M. Brown, A. Jorio, M. S. Dresselhaus, and G. Dresselhaus. Observations of the d-band feature in the raman spectra of carbon nanotubes. *Phys. Rev. B*, 64:073403, 2001.

Ch. Caillier, D. Machon, A. San-Miguel, R. Arenal, G. Montagnac, H. Cardon, M. Kalbac, M. Zukalova, and L. Kavan. Probing high-pressure properties of single-wall carbon nanotubes through fullerene encapsulation. *Phys. Rev. B*, 77:125418, 2008.

S. Cambré, B. Schoeters, S. Luyckx, E. Goovaerts, and W. Wenseleers. Experimental observation of single-file water filling of thin single-wall carbon nanotubes down to chiral index (5,3). *Phys. Rev. Lett.*, 104:207401, 2010.

J. Chen, M. A. Hamon, H. Hu, Y. Chen, A. M. Rao, P. C. Eklund, and R. C. Haddon. Solution properties of single-walled carbon nanotubes. *Science*, 282: 95–98, 1998.

D. Christofilos, J. Arvanitidis, C. Tzampazis, K. Papagelis, T. Takenobu, Y. Iwasa, H. Kataura, C. Lioutas, S. Ves, and G.A. Kourouklis. Raman study of metallic carbon nanotubes at elevated pressure. *Diamond Relat. Mater*, 15:1075–1079, 2005.

D. Christofilos, J. Arvanitidis, C. Tzampazis, K. Papagelis, T. Takenobu, Y. Iwasa, H. Kataura, C. Lioutas, S. Ves, and G.A. Kourouklis. Raman study of metallic carbon nanotubes at elevated pressure. *Diam. Relat. Mater.*, 15: 10751079, 2006.

D. Christofilos, J. Arvanitidis, K. S. Andrikopoulos, G. A. Kourouklis, S. Ves, T. Takenobu, and Y. Iwasa. Comparative high pressure raman study of individual and bundled single-wall carbon nanotubes. *phys. stat. sol. (b)*, 244: 100–104, 2007.

L. Corradi, A. Cammi, and L. Luzzi. *Collapse Behavior of Moderately Thick Tubes Pressurized from Outside*. InTech, USA, 2011.

C. S. G. Cousins and M. I. Heggie. Elasticity of carbon allotropes. iii. hexagonal graphite: Review of data, previous calculations, and a fit to a modified anharmonic keating model. *Phys. Rev. B*, 67:024109, 2003.

R. S. Deacon, K. C. Chuang, J. Doig, I. B. Mortimer, and R. J. Nicholas. Photoluminescence study of aqueous-surfactant-wrapped single-walled carbon nanotubes under hydrostatic pressure. *Phys. Rev. B*, 74:201402(R), 2006.

F. Ding, H. Ji, Y. Chen, A. Herklotz, K. Dorr, Y. Mei, A. Rastelli, and O. G. Schmidt. Stretchable graphene: A close look at fundamental parameters through biaxial straining. *Nano Lett.*, 10:34533458, 2010.

K.J. Donovan and K. Scott. Anomalous effective hydrodynamic radius of octadecylamine functionalised single walled carbon nanotubes. *Carbon*, 50: 3807–3815, 2012.

K.J. Donovan and K. Scott. Anomalous intrinsic viscosity of octadecylamine-functionalised carbon nanotubes in suspension. *J. Chem. Phys.*, 138:244902, 2013.

O. Dubay, G. Kresse, and H. Kuzmany. Phonon softening in metallic nanotubes by a peierls-like mechanism. *Phys. Rev. Lett.*, 88:235506, 2002.

D. J. Dunstan. Theory of the gasket in diamond anvil high-pressure cells. *Rev. Sci. Instrum.*, 60:3789, 1989.

D. J. Dunstan and A. J. Ghandour. High-pressure studies of carbon nanotubes. *High Pressure Res.*, 29:548–553, 2009.

K. F. Dziubek and A. Katrusiak. Polar symmetry in new high-pressure phases of chloroform and bromoform. *J. Phys. Chem. B*, 112:1200112009, 2008.

J. A. Elliott, J. K. W. Sandler, A. H. Windle, R. J. Young, and M. S. P. Shaffer. Collapse of single-wall carbon nanotubes is diameter dependent. *Phys. Rev. Lett.*, 92:095501, 2004.

C. Fantini, A. Jorio, M. Souza, M. S. Strano, M. S. Dresselhaus, and M. A. Pimenta. Optical transition energies for carbon nanotubes from resonant raman spectroscopy: Environment and temperature effects. *Phys. Rev. Lett*, 93:147406, 2004.

H. Farhat, H. Son, Ge. G Samsonidze, S. Reich, M. S. Dresselhaus, and J. Kong. Phonon softening in individual metallic carbon nanotubes due to the kohn anomaly. *Phys. Rev. Lett.*, 99:145506, 2007.

W. H. Fletcher and J. S. Rayside. High resolution vibrational raman spectrum of oxygen. *J. Raman Spectrosc.*, 2:3–14, 1974.

I. C. Gerber, P. Puech, A. Gannouni, and W. Bacsa. Influence of nitrogen doping on the radial breathing mode in carbon nanotubes. *Phys. Rev. B*, 79: 075423, 2009.

A. J. Ghandour, D. J. Dunstan, and A. Sapelkin. Raman g-mode of single-wall carbon nanotube bundles under pressure. *J. Raman Spectrosc.*, 42:1611–1613, 2011.

A. J. Ghandour, A. Sapelkin, I. Hernandez, D. J. Dunstan, I. F. Crowe, and M. P. Halsall. Raman excitation spectroscopy of carbon nanotubes: effects of pressure medium and pressure. *High Pressure Res.*, 32:67–71, 2012.

A. J. Ghandour, I. F. Crowe, J. E. Proctor, Y. W. Sun, M. P. Halsall, I. Hernandez, A. Sapelkin, and D. J. Dunstan. Pressure coefficients of raman modes of carbon nanotubes resolved by chirality: Environmental effect on graphene sheet. *Phys. Rev. B*, 87:085416, 2013.

J. F. Green, P. Bolsaitis, and I. L. Spain. Pressure dependence of c-axis elastic parameters of oriented graphite. *J. Phys. Chem. Solids*, 34:1927–1937, 1972.

S. Grimme. Semiempirical GGA-type density functional constructed with a long-range dispersion correction. *J. Comput. Chem.*, 27:1787, 2006.

M. Hanfland, H. Beister, and K. Syassen. Graphite under pressure: Equation of state and first-order raman modes. *Phys. Rev. B*, 39:12598, 1989.

P. Hohenberg and W. Kohn. Inhomogeneous electron gas. *Phys. Rev.*, 136: B864, 1964.

D. Holec, M. A. Hartmann, F. D. Fischer, F. G. Rammerstorfer, P. H. Mayrhofer, and Oskar Paris. Curvature-induced excess surface energy of fullerenes: Density functional theory and monte carlo simulations. *Phys. Rev. B*, 81:235403, 2010.

M. Huang, H. Yan, C. Chen, D. Song, T. F. Heinz, and J. Hone. Phonon softening and crystallographic orientation of strained graphene studied by raman spectroscopy. *PNAS*, 106:7304–7308, 2009.

H. Hubel, D. A. Faux, R. B. Jones, and D. J. Dunstan. Solvation pressure in chloroform. *J. Chem. Phys.*, 124:204506, 2006.

M. E. Itkis, D. E. Perea, S. Niyogi, S. M. Rickard, M. A. Hamon, H. Hu, B. Zhao, and R. C. Haddon. Purity evaluation of as-prepared single-walled carbon nanotube soot by use of solution-phase near-ir spectroscopy. *Nano Lett.*, 3:309–314, 2003.

A. Jorio, A. G. Souza Filho, G. Dresselhaus, M. S. Dresselhaus, A. K. Swan, M. S. Unlu, B. B. Goldberg, M. A. Pimenta, J. H. Hafner, C. M. Lieber, and R. Saito. G-band resonant raman study of 62 isolated single-wall carbon nanotubes. *Phys. Rev. B*, 65:155412, 2002.

H. Kataura, Y. Kumazawa, Y. Maniwa, I. Umezu, S. Suzuki, Y. Ohtsuka, and Y. Achiba. Optical properties of single-wall carbon nanotubes. *Synt. Met.*, 103:2555–2558, 1999.

G. Kavitha and C. Narayana. Raman spectroscopic investigations of pressure-induced phase transitions in n-hexane. *J. Phys. Chem. B*, 111:1413014135, 2007.

W. Kohn and L. J. Sham. Self-consistent equations including exchange and correlation effects. *Phys. Rev.*, 140:A1133, 1965.

G. Kresse and J. Furthmuller. Efficient iterative schemes for ab initio total-energy calculations using a plane-wave basis set. *Phys. Rev. B*, 54:11169, 1996.

G. Kresse and D. Joubert. From ultrasoft pseudopotentials to the projector augmented-wave method. *Phys. Rev. B*, 59:1758, 1999.

S. Lebedkin, K. Arnold, O. Kiowski, F. Hennrich, and M. M. Kappes. Raman study of individually dispersed single-walled carbon nanotubes under pressure. *Phys. Rev. B*, 73:094109, 2006.

H. Liu, D. Nishide, T. Tanaka, and H. Kataura. Large-scale single-chirality separation of single-wall carbon nanotubes by simple gel chromatography. *Nat. Commun.*, 2:309, 2011.

W. L. Liu, Z. R. Zheng, Z. F. Dai, Z. G. Liu, R. B. Zhu, W. Z. Wu, A. H. Li, Y. Q. Yang, and W. H. Su. Effect of solvent on absorption spectra of all-trans-β-carotene under high pressure. *J. Chem. Phys.*, 128:124501, 2006.

Z. Liu, L. Wang, Y. Zhao, Q. Cui, and G. Zou. High-pressure raman studies of graphite and ferric chloride-graphite. *J. Phys.: Condens. Matter*, 2:8083–8088, 1990.

M. J. Longhurst and N. Quirke. Pressure dependence of the radial breathing mode of carbon nanotubes: The effect of fluid adsorption. *Phys. Rev. Lett*, 98:145503, 2007.

H. K. Mao, J. Xu, and P. M. Bell. Calibration of the ruby pressure gauge to 800 kbar under quasi-hydrostatic conditions. *J. Geophys. Res. Sol. Ea.*, 91: 4673–4676, 1986.

R. M. Martin and L. M. Falicov. Light scattering in solids. In Manuel Cardona, editor, *Topics in Applied Physics*. Springer, 1975.

J. Maultzsch, H. Telg, S. Reich, and C. Thomsen. Radial breathing mode of single-walled carbon nanotubes: Optical transition energies and chiral-index assignment. *Phys. Rev. B*, 72:205438, 2005.

A. Merlen, N. Bendiab, P. Toulemonde, A. Aouizerat, A. San Miguel, J. L. Sauvajol, G. Montagnac, H. Cardon, and P. Petit. Resonant raman spectroscopy of single-wall carbon nanotubes under pressure. *Phys. Rev. B*, 72: 035409, 2005.

A. Merlen, P. Toulemonde, N. Bendiab, A. Aouizerat, J. L. Sauvajol, G. Montagnac, H. Cardon, P. Petit, and A. San Miguel. Raman spectroscopy of open-ended single wall carbon nanotubes under pressure: effect of the pressure transmitting medium. *phys. stat. sol. (b)*, 243:690–699, 2006.

T. M. G. Mohiuddin, A. Lombardo, R. R. Nair, A. Bonetti, G. Savini, R. Jalil, N. Bonini, D. M. Basko, C. Galiotis, N. Marzari, K. S. Novoselov, A. K. Geim, and A. C. Ferrari. Uniaxial strain in graphene by raman spectroscopy: G peak splitting, grneisen parameters, and sample orientation. *Phys. Rev. B*, 79:205433, 2009.

M. Mohr, J. Maultzsch, E. Dobardzic, S. Reich, I. Milosevic, M. Damnjanovic, A. Bosak, M. Krisch, and C. Thomsen. Phonon dispersion of graphite by inelastic x-ray scattering. *Phys. Rev. B*, 76:035439, 2007.

M. Mohr, K. Papagelis, J. Maultzsch, and C. Thomsen. Two-dimensional electronic and vibrational band structure of uniaxially strained graphene from ab initio calculations. *Phys. Rev. B*, 80:205410, 2009.

R. J. Nemanich, G. Lucovsky, and S. A. Solin. Infrared active optical vibrations of graphite. *Solid State Comm.*, 23:117, 1977.

Z. H. Ni, T. Yu, Y. H. Lu, Y. Y. Wang, Y. P. Feng, and Z. X. Shen. Uniaxial strain on graphene: Raman spectroscopy study and band-gap opening. *ACSNANO*, 2:2301–2305, 2008.

J. Nicolle, D. Machon, P. Poncharal, O. Pierre-Louis, and A. San-Miguel. Pressure-mediated doping in graphene. *Nano Lett.*, 11:3564–3568, 2011.

S. Niyogi, M. A. Hamon, H. Hu, B. Zhao, P. Bhowmik, R. Sen, M. E. Itkis, and R. C. Haddon. Chemistry of single-walled carbon nanotubes. *Acc. Chem. Res.*, 35:1105–1113, 2002.

M. J. O'Connell, S. M. Bachilo, C. B. Huffman, V. C. Moore, M. S. Strano, E. H. Haroz, K. L. Rialon, P. J. Boul, W. H. Noon, C. Kittrell, J. Ma, R. H. Hauge, R. B. Weisman, and R. E. Smalley. Band gap fluorescence from individual single-walled carbon nanotubes. *Science*, 297:593, 2002.

T. W. Odom, J. Huang, P. Kim, and C. M. Lieber. Atomic structure and electronic properties of single-walled carbon nanotubes. *Nature*, 391:62–64, 1998.

M. Pena-Alvarez, E. del Corro, V. G. Baonza, and M. Taravillo. Probing the stress effect on the electronic structure of graphite by resonant Raman spectroscopy. *J. Phys. Chem. C*, 118:25132–25140, 2014.

J.P. Perdew, K. Burke, and M. Ernzerhof. Generalized Gradient Approximation made simple. *Phys. Rev. Lett.*, 77:3865, 1996.

J. E. Proctor, M. P. Halsall, A. Ghandour, and D. J. Dunstan. High pressure raman spectroscopy of single-walled carbon nanotubes:effect of chemical environment on individual nanotubes and the nanotube bundle. *J. Phys. Chem. Solids*, 67:2468–2472, 2006.

J. E. Proctor, E. Gregoryanz, K. S. Novoselov, M. Lotya, J. N. Coleman, and M. P. Halsall. High-pressure raman spectroscopy of graphene. *Phys. Rev. B*, 80:073408, 2009.

P. Puech, E. Flahaut, A. Sapelkin, H. Hubel, D. J. Dunstan, G. Landa, and W. S. Bacsa. Nanoscale pressure effects in individual double-wall carbon nanotubes. *Phys. Rev. B*, 73:233408, 2006.

A. M. Rao, E. Richter, S. Bandow, B. Chase, P. C. Eklund, K. A. Williams, S. Fang, K. R. Subbaswamy, M. Menon, A. Thess, R. E. Smalley, G. Dresselhaus, and M. S. Dresselhaus. Diameter-selective raman scattering from vibrational modes in carbon nanotubes. *Science*, 275:187–191, 1997.

S. Reich and C. Thomsen. Raman spectroscopy of graphite. *Phil. Trans. R. Soc. Lond. A*, 362:2271–2288, 2004.

S. Reich, H. Jantoljak, and C. Thomsen. Shear strain in carbon nanotubes under hydrostatic pressure. *Phys. Rev. B*, 61:R13 389, 2000.

S. Reich, C. Thomsen, and J. Maultzsch. *Carbon Nanotubes: Basic Concepts and Physical Properties*. Wiley-VCH, 2004.

R. J. Sabharwal, Y. Huang, and Y. Song. High-pressure induced conformational and phase transformations of 1,2-dichloroethane probed by raman spectroscopy. *J. Phys. Chem. B*, 111:72677273, 2007.

J. R. Sanchez-Valencia, T. Dienel, O. Groning, I. Shorubalko, A. Mueller, M. Yansen, K. Amsharov, P. Ruffieux, and R. Fasel. Controlled synthesis of single-chirality carbon nanotubes. *Nature*, 512:6164, 2014.

J. Sandler, M. S. P. Shaffer, A. H. Windle, M. P. Halsall, M. A. Montes-Moran, C. A. Cooper, and R. J. Young. Variations in the Raman peak shift as a function of hydrostatic pressure for various carbon nanostructures: A simple geometric effect. *Phys. Rev. B*, 67:035417, 2003.

V. Skakalova, A. B. Kaiser, U. Dettlaff-Weglikowska, K. Hrncarikova, and S. Roth. Effect of chemical treatment on electrical conductivity, infrared

absorption, and raman spectra of single-walled carbon nanotubes. *J. Phys. Chem. B*, 109:7174–7181, 2005.

A. V. Soldatov, S. You, M. Mases, and K. S. Novoselov. Free standing graphene monolayer at high hydrostatic pressure. In *Graphene 2012, Abstract Book of the Conference*, page 172, 2012.

A. K. Sood, P. V. Teresdesai, D. V. S. Muthu, R. Sen, A. Govindara, and C. N. R. Rao. Pressure behaviour of single wall carbon nanotube bundles and fullerenes: A raman study. *phys. stat. sol. (b)*, 215:393, 1999.

Y. W. Sun, D. J. Dunstan, M. A. Hartmann, and D. Holec. Nanomechanics of carbon nanotubes. *Proc. Appl. Math. Mech.*, 13:7–10, 2013.

Y. W. Sun, I. Hernandez, A.J. Ghandour, C. Rice, I.F. Crowe, M.P. Halsall, A. Sapelkin, J. Gonzalez, F. Rodriguez, and D.J. Dunstan. Resonance raman spectroscopy of carbon nanotubes: pressure effects on g-mode. *High Pressure Res.*, 34:191–197, 2014.

H. Telg, J. Maultzsch, S. Reich, and C. Thomsen. First and second optical transitions in single-walled carbon nanotubes: a resonant raman study. *phys. stat. sol. (b)*, 244:4006–4010, 2007.

C. Thomsen, S. Reich, H. Jantoljak, I. Loa, K. Syassen, M. Burghard, G.S. Duesberg, and S. Roth. Raman spectroscopy on single- and multi-walled nanotubes under high pressure. *Appl. Phys. A*, 69:309, 1999.

C. Thomsen, S. Reich, and P. Ordejon. Ab initio determination of the phonon deformation potentials of graphene. *Phys. Rev. B*, 65:073403, 2002.

S.P. Timoshenko and J.N. Goodier. *Theory of Elasticity, 3rd ed.* McGraw-Hill, New York, 1970.

A. Togo, F. Oba, and I. Tanaka. First-principles calculations of the ferroelastic transition between rutile-type and $CaCl_2$-type SiO_2 at high pressures. *Phys. Rev. B*, 78:134106, 2008.

M. M. J. Treacy, T. W. Ebbesen, and J. M. Gibson. Exceptionally high young's modulus observed for individual carbon nanotubes. *Nature*, 381:678–680, 1996.

F. Tuinstra and J. L. Koenig. Raman spectrum of graphite. *J. Chem. Phys.*, 53:1126, 1970.

N. W. A. van Uden and D. J. Dunstan. Zen diamond-anvil low-pressure cell. *Rev. Sci. Instrum.*, 71:4174, 2000.

L. C. Venema, V. Meunier, Ph. Lambin, and C. Dekker. Atomic structure of carbon nanotubes from scanning tunneling microscopy. *Phys. Rev. B*, 61: 2991, 2000.

U. D. Venkateswaran, A. M. Rao, E. Richter, M. Menon, A. Rinzler, R. E. Smalley, and P. C. Eklund. Probing the single-wall carbon nanotube bundle: Raman scattering under high pressure. *Phys. Rev. B*, 59:10928, 1999.

U. D. Venkateswaran, E. A. Brandsen, U. Schlecht, A. M. Rao, E. Richter, I. Loa, K. Syassen, and P. C. Eklund. High pressure studies of the raman-active phonons in carbon nanotubes. *phys. stat. sol. (b)*, 223:225–236, 2001.

U. D. Venkateswaran, D. L. Masica, G. U. Sumanasekera, C. A. Furtado, U. J. Kim, and P. C. Eklund. Diameter dependent wall deformations during the compression of a carbon nanotube bundle. *Phys. Rev. B*, 68:241406, 2003.

J. H. Walther, R. Jaffe, T. Halicioglu, and P. Koumoutsakos. Carbon nanotubes in water: structural characteristics and energetics. *J. Phys. Chem. B*, 105: 99809987, 2001.

L. Yang and J. Han. Electronic structure of deformed carbon nanotubes. *Phys. Rev. Lett.*, 85:154–157, 2000.

M. Yao, Z. Wang, B. Liu, Y. Zou, S. Yu, W. Lin, Y. Hou, S. Pan, M. Jin, B. Zou, T. Cui, G. Zou, and B. Sundqvist. Raman signature to identify the structural transition of single-wall carbon nanotubes under high pressure. *Phys. Rev. B*, 78:205411, 2008.

R. Yu, J. Zhu, and H.Q. Ye. Calculations of single-crystal elastic constants made simple. *Comput Phys Commun*, 181:671, 2010.